UNIVERSITY OF PADOVA

Department of Management and Engineering
PhD School of Mechatronics and Product Innovation Engineering
PhD cycle: XXVII

Novel measurement techniques for motion analysis and human recognition by using ultrasound and radiofrequency signals

---

PhD school director: Ch.mo prof. Alessandro Persona
PhD supervisor: Ch.mo prof. Alessandro Sona

Phd candidate: **Roberto Ricci**

This research has been partially supported by Fondazione Studi Universitari di Vicenza.

ABSTRACT

Human detection and identification has been constituting a fundamental application in everyday life, and it is assuming an increasing importance both within the commercial world and the scientific community. The applications cover a variety of different areas, such as security and surveillance, rescue/recovery of troubled people, medicine and gait analysis.

Among the plenty of employed technologies, over the last few years, radar and ultrasound systems are gaining an increasing interest in human detection/identification scenario. They can effectively work in particular environments and situations where other systems may fail, like in the darkness, in smoky or foggy areas, or through not transparent obstacles. Many radar and ultrasound systems for human detection exploit Doppler and micro-Doppler effects to analyse the target motion. The micro-Doppler effect is a variant of the Doppler phenomenon which accounts also for micro-motions of the target superimposed to the bulk motion. Hence, it can be deployed to record the micro-Doppler characteristics of different moving targets, commonly referred as micro-Doppler signature. Human moving targets exhibit very distinctive and unique micro-Doppler signatures, which, if properly analysed, may be used to carry out human target recognition and classification tasks.

Aim of this dissertation is to provide a general and technology independent measurement approach suitable for human identification purposes. The approach is a list of elementary blocks covering the measurement device definition and setup, the micro-Doppler signature acquisition and the algorithm for signatures analysis. In order to test the procedure, several experimental trials to collect micro-Doppler signatures have been performed, both in the ultrasonic and radio frequency domain. A novel algorithm has been also designed and developed to extract some particular features from the acquired signatures, to be used for target classification. Recognition performance has been assessed as a function of some key algorithm parameters to investigate the level of robustness of the proposed features. Results show that high level recognition performance can be achieved for different human activities and subjects, both employing ultrasounds and radio-frequency waves.

SOMMARIO

Il rilevamento e l'identificazione di persone rappresenta un'applicazione fondamentale nella vita di ogni giorno, e per questo sta assumendo un'importanza ed un interesse crescente all'interno del mondo commerciale e della comunità scientifica. Tra le innumerevoli applicazioni pratiche, si annoverano la sicurezza e la sorveglianza, il recupero ed il soccorso di persone in situazioni di emergenza, ed in medicina per la diagnosi di patologie posturali e non. Tra la vastità di tecnologie impiegate, negli ultimi anni i sistemi ad ultrasuoni e radar stanno catturando un interesse sempre maggiore nello scenario dell'identificazione ed il rilevamento umano. Tali tecnologie infatti possono operare in particolari situazioni ambientali non adatte ad altre sistemi, come ad esempio, in presenza di fumo e nebbia, o in aree buie, oppure attraverso barriere non trasparenti come muri e vegetazione. Molti sistemi radar sono progettati per sfruttare gli effetti Doppler e micro-Doppler per analizzare il movimento del target da rilevare. In termine micro-Doppler rappresenta una variante dell'effetto Doppler che considera ulteriori micro-movimenti del target, che possono essere sovrapposti al moto principale. Può essere quindi impiegato per rilevare le caratteristiche micro-Doppler, di diversi target in movimento. Tali caratteristiche, dette anche signatures micro-Doppler, si dimostrano essere una peculiarità unica e distintiva per quanto riguarda il movimento umano. Lo scopo della tesi è quello di fornire un approccio di misura che sia generale ed indipendente dalla particolare tecnologia, da usarsi per applicazioni riguardanti l'identificazione di umani. L'approccio prevede una lista di blocchi elementari, riguardanti la scelta del dispositivo e dell'ambiente di misura, l'acquisizione di signatures micro-Doppler e lo sviluppo di un algoritmo per l'analisi e la classificazione delle signatures. La procedura è stata quindi testata sia nel caso si impieghi una tecnologia ad ultrasuoni, che una tecnologia radar. È stato inoltre sviluppato un algoritmo innovativo per estrarre un insieme di parametri dalle signatures acquisite, per poi essere usati con lo scopo di classificare i target umani analizzati. Le prestazioni della procedura di riconoscimento sono state valutate in funzione di alcuni parametri chiave dell'algoritmo sviluppato, al fine di valutarne robustezza ed affidabilità. I risultati ottenuti mostrano un alto livello di riconoscimento positivo, per

diversi target umani ed attività analizzate, e sia nel caso si impieghino onde ultrasonore che a radiofrequenza.

CONTENTS

LIST OF FIGURES

LIST OF TABLES

1 INTRODUCTION

Human detection and identification has been constituting a fundamental application in everyday life, and it is assuming an increasing importance both within the commercial world and the scientific community. The applications cover a variety of different areas, such as security and surveillance, rescue/recovery of troubled people, medicine and gait analysis. For example, some detection systems are used to analyse and monitor people flows and crowds in highly secure areas, such as airports, underground and train stations. Some surveillance systems comprise human recognition techniques for limited access control. Other applications involve the detection of troubled people for rescue operations, e.g. persons under the debris or snow heaps. In medicine, human recognition techniques can be deployed for diseases diagnosis, e.g. gait analysis for posture and articulation problems detection.

Many techniques and technologies can be deployed for human detection/identification purposes, depending also on the specific application. Camera-based systems constitute the most used and diffused technology for security and surveillance applications [3, 4, 5]. Such techniques exploit face detection or shape recognition algorithms for a single human identification, or computation geometry concepts for crowds behaviour monitoring. Infrared technology can be used for human detection as well [6, 7], deploying the distinctive human thermal pattern. Other techniques analyse the seismic pattern generated by the human gait to recognise the presence of people in the scenario [8, 9, 10]. They are often implemented in the audio or ultrasonic domain to detect both the step repetition frequency and the footstep signature generated by the ground-foot friction.

1.1 DOPPLER RADAR AND ULTRASOUND SYSTEMS FOR HUMAN IDENTIFICATION

Radar (Radio Detection and Ranging) is an object detection system which exploits radio waves to determine the range, altitude, direction or speed of potential targets. Basically, a radio wave is emitted and a part of the the transmitted energy returns to the device providing information about

the monitored environment. The term ultrasound radar is used to denote devices which deploys the same principle but in the ultrasonic domain.

Over the last few years, radar and ultrasound systems are gaining an increasing interest in human detection/identification scenario. They can effectively work in particular environments and situations where the previously mentioned systems fail. For example, they can be deployed in daytime as well as in the darkness, or in smoky or foggy areas. Radar systems can be effective even in presence of not transparent obstacles, like walls, debris or vegetation. Furthermore, thermal or acoustical noise typical of urban areas do not affect the radar system performance.

In literature, some works deploy Ultra Wide Band (UWB) radar as a ranging system to track people position or detect human breath [11, 12, 13, 14]. Although most of the work and this dissertation focus on Doppler radar and ultrasound systems to analyse the human movement characteristics.

The Doppler effect or Doppler shift is the perception of frequency variations of a wave for an observer in relative motion with respect to the wave emitter. The nomenclature is due to the Austrian physicist Christian Doppler who proposed the phenomenon explanation. A common example of Doppler effect takes place when a moving vehicle sounding a siren approaches or and recedes from an external observer. Compared to the emitted frequency, the observer perceives an higher frequency during the approach, while a lower frequency is heard during the recession. The Doppler effect is an apparent phenomenon. Suppose to have a general wave emitter (radio-frequency or acoustic) approaching a static observer. Each successive wave crest is emitted from a position closer to the observer than the previous wave. Therefore, each wave takes slightly less time to reach the observer than the previous one, which causes the perception of an higher frequency.

The micro-Doppler (μ-D) effect is a variant of the Doppler phenomenon which accounts also for micro-motions of the target superimposed to the bulk motion. Hence, it can be deployed to record the micro-Doppler characteristics of different moving targets, commonly referred as μ-D signature. Human moving targets exhibit very distinctive and unique micro-Doppler signatures, which, if properly analysed, may be used to carry out human target recognition and classification tasks.

1.2 LITERATURE OVERVIEW

Radar target classification by micro-Doppler signatures has attracted considerable research interest in recent years. An excellent overview of the topic and its latest advances and applications can be found in [15] and [16] and a review of some of the latest research on micro-Doppler applied to emerging radar techniques is presented in [17]. In the literature the micro-Doppler signatures of different targets have been measured and analysed and these include rigid bodies [1, 18], aircraft [19], helicopters [20], space based rigid targets [21], and tracked and wheeled vehicles [22].

Much work on micro-Doppler has been carried out to classify human targets using radar systems, Synthetic Aperture Radar (SAR) [23, 24] and Inverse Synthetic Aperture Radar (ISAR) [25, 26, 27]. In [28], the authors developed a 10.525 GHz coherent CW radar to measure human micro-Doppler signatures and extract a robust set of features of the human gait using the Short Time Fourier Transforms (STFT) and the Chirplet. They found that the STFT can provide a better and unambiguous description of the human bio-mechanical motion with respect to the Chirplet. The experimental results were compared with a set of human micro-Doppler signatures obtained from the trajectories of some target components which were measured with an infrared motion capture system [29]. The results overall showed that the micro-Doppler signature of the human gait contains bio-mechanical features which are associated to the movement of the legs and the body. A feature-based human motion parameter estimation was performed on a set of human micro-Doppler signatures measured with a 9.68 GHz frequency-modulated CW radar from various target aspect angles ranging from 0° to 180° [30]. A set of features based on the spectrogram of echoes from humans was proposed in [31] and used as the input of a Boulic and Thalmann walking model to reconstruct the human motion. A commercial low-cost CW radar operating at 10.525 GHz was used in [32] to perform human detection and classification by micro-Doppler signatures. A set of features consisting of (i) the mean walking speed, (ii) the step repetition frequency, (iii) the stride length, (iv) and the radar cross sections (RCS) of some moving body components was extracted from the signatures and used in a binary classifier to detect the presence or non-presence of people in front of the device. The authors showed that 88% successful classification performance could be achieved with the proposed method. A pulsed Doppler

radar operating at 9 GHz was used to distinguish between one human, two humans and a vehicle by their micro-Doppler signatures in [33]. A vector consisting of Cepstrum features was extracted from the signatures and used to classify using both a voting and a maximum likelihood classification scheme. The classifiers were trained with both statistical and physical features of the human locomotion model and results showed that correct classification performance up to 99% could be achieved with this combined approach. In [34], the micro-Doppler signatures of 12 human targets performing different activities including walking, running, crawling, boxing and sitting were collected with a 2.4 GHz CW radar. These were used in a Support Vector Machine (SVM) classifier to distinguish between activities. Results showed a success classification rate of nearly 90% could be achieved.
In recent years there has also been an increasing interest in detecting and classifying humans by their micro-Doppler signature using ultrasound. A CW ultrasound radar operating at 40 kHz was developed in [35] to demonstrate the suitability of acoustics for human target classification by micro-Doppler in short range applications. In [36] an active ultrasound radar at 40 kHz was deployed together with a passive ultrasound receiver to investigate the synchronisation properties of the signature of the human gate between passive and active measurements. The micro-Doppler signatures of isolated body segments of a walking human were collected in [37] using ultrasound at a 40 kHz. An assessment of classification performance using ultrasound human micro-Doppler signatures collected at 80 kHz was carried out in [38] to distinguish between running and walking humans. The authors also presented a preliminary study of recognition performance in [39] and showed that high level recognition performance was very challenging to achieve with the proposed features even when only two classes were used.

1.3 DISSERTATION OBJECTIVES AND STRUCTURE

Although the literature presents a lot of work on the analysis of human micro-Doppler signatures, there is very little work attempting to use human micro-Doppler signatures for identification and recognition. Most of the existing contributions have focused on the classification between humans and other types of targets or between human performing different activities. The use of micro-Doppler signatures for target identification, i.e. when the target is of the same type, remains a very challenging task

that requires the extraction of key and robust features that guarantee suitable separability between different targets.

Aim of this dissertation is to provide a general and technology-independent measurement approach suitable for human identification purposes. The approach is a list of elementary blocks covering the measurement device definition and setup, the μ-D signature acquisition and the algorithm for signatures analysis. In order to test the procedure, several experimental trials to collect micro-Doppler signatures have been performed, both in the ultrasonic and radio frequency domain. A novel algorithm has been also designed and developed to extract some particular features from the acquired signatures, to be used for target classification. Recognition performance has been assessed as a function of some key algorithm parameters to investigate the level of robustness of the proposed features. Results show that high level recognition performance can be achieved for different human activities and subjects, both employing ultrasounds and radio waves.

The dissertation is organised according to the following sections:

- in Chapter 2, some basics are provided regarding radar and ultrasound systems, as long as some theoretical concepts about Doppler and micro Doppler effects. The use of kinematic model for human gait simulation is also treated, along with an algorithm to detect particular features within images. All the concepts introduced are then merged into the development of a novel measurement approach for human motion analysis, detection and identification. A simulation of the measurement procedure is reported at the end of the chapter.

- In Chapter 3, an ultrasound Doppler system is designed, to prove the effectiveness of the measurement approach. The ultrasound system is then characterised by using a proper measurement setup, which employs a rotating sphere as reference target.

- In Chapter 4, the developed ultrasound system is characterised, by comparing the ultrasound micro-Doppler signatures with the results of a very accurate motion capture system, based on cameras. To this aim, a test human target is properly arranged to wear a set of reflecting markers that can be detected by the cameras-based system. The target is asked to perform some basic movements and walk normally, then the trajectories measured by the motion cap-

ture system are compared to the micro-Doppler signatures collected by the ultrasound system.

- In Chapter 5, a measurement campaign is reported, with the aim to prove the effectiveness of the measurement approach in a real case study. In particular, the micro-Doppler signatures of several human targets gait are collected by the developed ultrasound system, then analysed and finally classified in order to detect the person identity.

- In Chapter 6, the measurement approach has been tested in the case of radio-frequency waves. Four human targets are analysed while performing a walking and running activity. The associated micro-Doppler signatures are gathered through a 10 GHz continuous wave radar. The signatures are then analysed and classified to detect the person identity, according to different setup of the processing algorithm to check its robustness and find an optimal parametric setup. Finally, a comparison is reported, between the classification of ultrasound and radar micro-Doppler signatures.

- In Chapter 7, some conclusive observations are reported, regarding the achieved results and possible advancements.

2

BASICS AND DESIGN OF A MEASUREMENT APPROACH

In this chapter a measurement approach is proposed for human motion analysis and detection, by using radar/ultrasound systems and exploiting the micro-Doppler signature generated by the human motion. The aim of the approach is to provide a framework through which better organise, compare and merge further researches, ideas and results. The approach does not specifically refer to a given application. Furthermore, the design is technology independent, which means that the measurement operations may be achieved employing different devices and/or technologies. It can be thus considered of interest for a wide range of possible applications, with particular regard to medicine, security and disaster recovery.

The definition of the approach requires a prior knowledge regarding some of the underling basic concepts. Indeed, the first part of the chapter provides some basic information about radar and ultrasound systems, introducing the terminology and the principles of operation. Then, an overview about the Doppler and micro-Doppler theory is provided along with the common mathematical relations. Some concepts about human gait modelling are hence provided, with particular emphasis to the Boulic-Thalmann walking model. Furthermore, some image processing algorithms are explained, especially the Hough algorithm to detect sinusoidal waves within image. The latter one can be very suitable for the classification of the micro-Doppler signatures generated by the human gait. At the end of the chapter and example of approach application is then provided.

2.1 RADAR AND ULTRASOUND DEVICES

A radar is an electromagnetic sensor for the detection and location of reflecting objects [40]. Summarising, it performs the following operation:

1. the radar radiates electromagnetic energy from an antenna to propagate in space.

2. some of the radiated energy is intercepted by a reflecting object, usually called a target, located at a distance from the radar.

3. The energy intercepted by the target is re-radiated in many directions.

4. Some of the re-radiated energy (echo) is returned to and received by the radar antenna.

5. After amplification and some signal processing techniques performed by the receiver, a decision is made as to whether or not a target echo signal is present. Other information about the target may be achieved at this stage.

This list of operation are valid even for and ultrasonic radar, as far as pressure wave (or ultrasonic energy) replaces electromagnetic wave. In general, the following information is valid for an ultrasound device as well.

The basic parts of a simple radar are the *transmitter*, which constitutes of a power amplifier generating a suitable waveform for the particular task of the radar. In the case a radar shares a single antenna for transmitting and receiving, a *duplexer* is needed to protect the sensitive receiver while the transmitter is on and to direct the received echo to the receiver. The *antenna* is the part allowing the transmitted energy to be propagated into space and then gathers the echo energy coming from targets. The *receiver* acts as low-noise amplifier to augment the weak received signal to a level where its presence can be detected. The *signal processor* is usually embedded into the receiver and separates the desired signal from the undesired signals which can degrade the detection process. Aim of the processor is also to take the detection decision and draw out some additional information about the target.
Regarding the radar terminology, often the following association are made:

- **Target.** Reflecting object to detect. It causes a backscatter of the radiated energy.

- **Echo.** Part of the backscattered energy that returns to the receiver.

- **Clutter.** Object located in the monitored environment, which generates unwanted return echoes that may cause incorrect detection of the target.

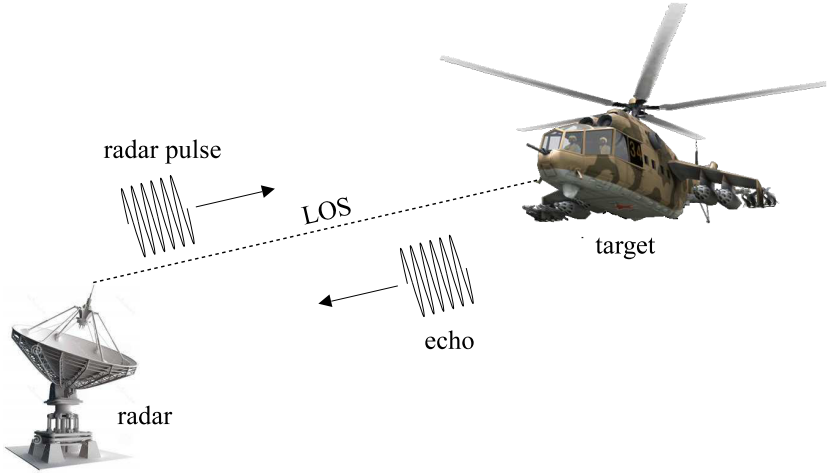

Figure 1: Illustration of some basic concepts related to a radar systems.

- **RCS.** Radar Cross Section, is the measure of how a target is detectable. The larger the RCS the more detectable the target. The RCS affects the amount of energy that backscatters from the target, with respect to the incident energy.
- **LOS.** Line of sight, is the line from the radar set directly to the target.

In Figure 1, the concepts of radar echo, LOS and target are shown.

Depending on the radar structure, two different types of radar can be identified. A **mono-static radar** is a device in which a single a antenna is deployed to radiate the radio signal and collect target echo signals. In a **bi-static radar** two different antennas are used for the transmission and reception operations.

Another classification of radar systems can be achieve according to the different type of transmitting wave:

- *Continuous Wave (CW) radar.* This radar employs a continuous sine wave. It almost always uses the Doppler frequency shift for detecting moving targets or for measuring their relative velocity.
- *Frequency Modulated (FM) CW radar.* This CW radar uses frequency modulation of the waveform to allow a range measurement.
- *Pulse radar.* This is a radar that radiates a repetitive series of rectangular pulses.
- *Pulse compression radar.* This device uses a long pulse with internal modulation to obtain the energy of a long pulse with the resolution of a short pulse.

The term "Doppler" beside the enlisted types of radar indicates that the system exploits a Doppler processing technique enhancing the radar performance to obtain additional information about the target. For example, the Doppler processing can be applied to overcome the problem of static clutters, or to obtain a direct measurement of the target speed. Interpreting the Doppler signature induced by the target motion can allow to carry out recognition and classification tasks of different types of target.

2.2 MICRO-DOPPLER PRINCIPLES

When a radar or an ultrasound device transmits a wave (electromagnetic or acoustic) to a target, such a wave interacts with the target, and an amount of the transmitted energy returns back to the device. Changes in the properties of the returned signal reflect the characteristics of interest for the target [1]. Whenever a target moves with a constant velocity, the carrier frequency of the returned signal will be shifted, according to the well known Doppler effect phenomenon [41]. For a mono-static radio-frequency or ultrasound radar, where the transmitter and the receiver are at the same location, the total distance covered by the wave is twice the distance between the transmitter and the target. The Doppler frequency shift f_d is computed as:

$$f_d = -2\,\frac{f_c}{c}\,v_r, \tag{1}$$

in which f_c is the carrier frequency of the transmitter, c is the propagation speed in the medium, and v_r is the radar-target relative velocity. Eq. (1) can be also expressed in term of wavelength λ_c, as $f_d = -2v_r/\lambda_c$, considering that $\lambda_c = c/f_c$. If the radar is stationary, v_r constitutes the velocity of the target along the line of sight of the radar, known as the radial velocity. When the target is moving away from the radar, the velocity is defined to be positive, and hence the Doppler shift is negative.

Common targets are often complex, and can be made of several parts, each moving with respect to the main target velocity. Even a simple target can be characterised by additional movements superimposed to the main motion law. A mechanical vibration or rotation in addition to the bulk motion might induce a frequency modulation on the returned signal that generates sidebands around the target main Doppler frequency shift. This is called the **micro-Doppler effect**. Radar or ultrasound signals backscattered from a target characterised by vibrating or rotating parts, such as propellers of a fixed-wing aircraft or rotors of a helicopter

contain micro-Doppler features related to these structures. In the case of humans, the moving parts are represented by the appendages, which oscillate with respect to the main gait velocity.

Potentially, the micro-Doppler effect allows to detect the motion characteristics of targets, and it offers a different approach for the analysis, detection and recognition of targets in term of μ-D signature. Such a signature can provide additional information and features which are complementary to those obtained with existing methods. The micro-Doppler effect can be employed to recognise specific type of vehicles as well as their engine speed. Signatures generated by helicopters blades can be used to distinguish the particular type and/or model. From micro-Doppler return generated by the engine vibration signal of a ground vehicle, one can distinguish whether it is a gas turbine engine of a tank or the diesel engine of a bus. Regarding human detection applications, the micro-Doppler signature (human signature) can be deployed to classify/detect different class of people or even the person identity.

The study of micro-Doppler effect can be performed through analytic, finite elements simulations or experimental techniques. For simple targets, such as point scatters, spherical or cylindrical rigid bodies an analytic expression can be derived.

2.2.1 *Vibrating targets and induced micro-Doppler*

A target translation or vibration modulates the phase function of the scattered electromagnetic or ultrasonic waves. When the target oscillates linearly and periodically, the modulation generates sideband frequencies about the carrier frequency of the incident wave.

In order to understand the μ-D phenomenon, consider the setup described in Figure 2. The sketch is suitable to analyse the μ-D signature induced by a scatterer point P, considered a perfect reflector, i.e. all the intercepted energy is reflected. A mono-static radar is located at the origin of the (U, V, W) reference system. P oscillates around a center point O, according to the law $D_t = D_v \, sin(2\pi f_v \cdot t)$, in which D_v and f_v are respectively the vibration amplitude and frequency. The center point O is assumed to be stationary with respect to the radar and at distance equal to R_0. O is also the origin of the (X, Y, Z) reference system, while α and β respectively indicate the azimuth and elevation angle of O with respect

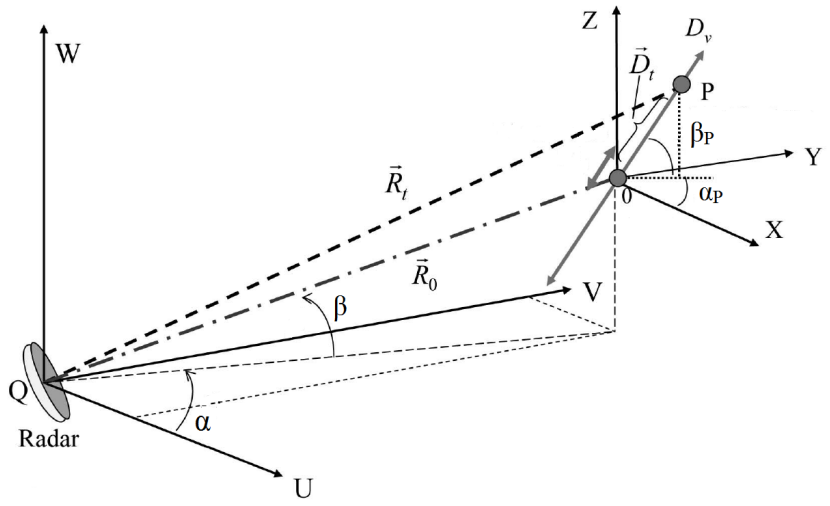

Figure 2: Geometry for radar and a vibrating scatter point P [1].

to the radar. The coordinates of O in the radar reference system can be expressed as:

$$\vec{R}_0 = [R_0 \cos\alpha \cos\beta,\ R_0 \sin\alpha \cos\beta,\ R_0 \sin\beta]^T. \tag{2}$$

Considering that α_P and β_P are the azimuth and elevation angle of the vibration direction with respect to reference system (X, Y, Z), the vector $\vec{D}_t = \vec{OP}$ can be expressed as:

$$\vec{D}_t = [D_t \cos\alpha_P \cos\beta_P,\ D_t \sin\alpha_P \cos\beta_P,\ D_t \sin\beta_P]^T. \tag{3}$$

Hence, as shown in Figure 2, the vector from the radar to the scatterer P becomes $\vec{R}_t = \vec{R}_0 + \vec{D}_t$ and the range can be computed as:

$$\begin{aligned} R_t = |\vec{R}_t| = [&(R_0 \cos\alpha \cos\beta + D_t \cos\alpha_P \cos\beta_P)^2 \\ &+ (R_0 \sin\alpha \cos\beta + D_t \sin\alpha_P \cos\beta_P)^2 \\ &+ (R_0 \sin\beta + D_t \sin\beta_P)^2]^{1/2}. \end{aligned} \tag{4}$$

Range R_t is a time varying function, due to the presence of term D_t, and hence to the scatterer movement. Even if R_t can now be deployed to compute the radar return signal, further hypotheses are now assumed to achieve a simpler expression.
When $R_0 \gg D_t$, and α and β_P are both zero, the range becomes approximately:

$$\begin{aligned} R_t &= (R_0^2 + D_t^2 + 2R_0 D_t \cos\alpha_P \cos\beta)^{1/2} \\ &\cong R_0 + D_t \cos\alpha_P \cos\beta. \end{aligned} \tag{5}$$

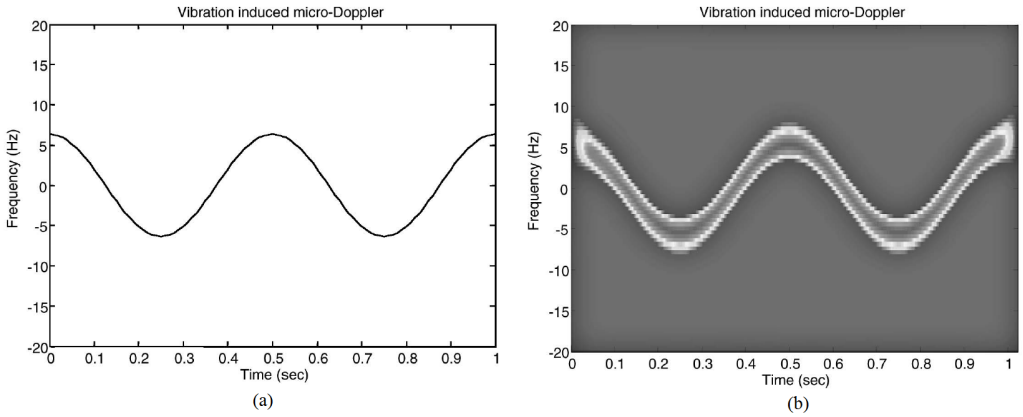

Figure 3: Micro-Doppler modulation induced by vibration [1].

The range function can be finally formulated considering the P vibration expression:

$$R(t) = R_t = R_0 + D_v \sin(2\pi f_v \cdot t) \cos\alpha_P \cos\beta. \tag{6}$$

If the radar transmits a sinusoidal waveform with a carrier frequency f_c, then the received signal $s_r(t)$ can be computed as:

$$\begin{aligned} s_r(t) &= \rho \exp\{j(2\pi f_c t + 4\pi \frac{R(t)}{\lambda_c})\} \\ &= \rho \exp\{j(2\pi f_c t + \Phi(t))\}, \end{aligned} \tag{7}$$

where ρ is the reflectivity of the point scatterer, and $\Phi(t)$ is the phase modulation function. Finally, the time derivative of $\Phi(t)$ provides the micro-Doppler shift function, $f_{\mu-D}(t)$ induced by the vibration, and considering Eq. (6), it becomes:

$$f_{\mu-D}(t) = \frac{1}{2\pi} \frac{d\,\Phi(t)}{dt} = \frac{4\pi f_v D_v}{\lambda_c} \cos\alpha_P \cos\beta \cos(2\pi f_v \cdot t). \tag{8}$$

Figure 3 shows a simulation of the μ-D signature induced by a vibrating point scatterer, in the case of a 10 GHz pulse Doppler radar with a Pulse Repetition Frequency (PRF) of 2000 Hz. The other input data is: $D_v = 0.01m$, $f_v = 2Hz$, $\alpha_P = 30°$, $\beta_P = 30°$, and the center of the vibration at $(U, V, W) = (1000, 5000, 5000)\,m$. It can be noticed that the theoretical result in Figure 3a is identical to the simulated signature of Figure 3b.

From this analysis, it is evident how the ability to extract such an information from the returned signal can play an important role in modern automatic target recognition systems, which can be deployed in human detection/recognition system as well.

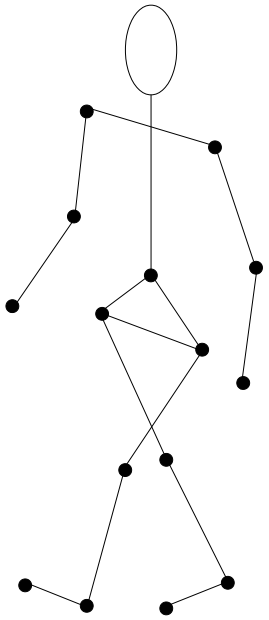

Figure 4: Representation of the sticky man and the relative junction points.

2.3 HUMAN GAIT MODEL

The study of the human gait is a non-trivial task. The human motion pattern is composed of several body parts moving according to different trajectories and at different velocities. In the past, the human gait model has been largely studied [42, 43, 31]. In particular, L. Ren et al.[43] compare different models and techniques synthesising human walking, F. Faure et al. [42] give some computation and analysis tools for estimating the human internal actuator forces. In another paper [31], the well-known Boulic and Thalmann walking model (BT-model) is presented. It is based on experimental biomechanical data collected from a large set of test persons. As represented in Figure 4, the human body is represented as a stick figure, with lines linking the main joints of the human body. In this dissertation, the BT-model has been adopted to emulate the radar μ-D response of a walking human, for its simplicity and because it has already been shown to be applicable in radar simulations [44, 30].
The implementation of BT-model consists on the following stages:

1. **Global parameters definition.** The model provides a set of basic trajectories consisting of the translation of the base spine, and the rotations of thorax, shoulder, elbow, hip, knee, and ankle. Such trajectories are function of just two global parameters (inputs), the

height at the thigh, h_t, and the medium walking velocity, v. Three additional parameters are then derived as follows:

$$\begin{aligned} RV &= \frac{v}{h_t}, \\ RLc &= 1.346\sqrt{RV}, \\ Tc &= \frac{RLc}{RV}, \end{aligned} \tag{9}$$

where RV is defined as relative velocity, RLc is the relative length of cycle and Tc is the cycle time.

2. **Basic/Joints trajectories.** Trajectories of the angles between various links as well as the translation of the origin (located at the base of the spine) are provided over the duration of one cycle, i.e. two steps. Thereafter, the walking motion is assumed to repeat identically. Details on the derivation of the basic trajectories are omitted here and reported in the bibliography-reported article [31].

3. **Junction points 3-d trajectories.** The forward cinematic modelling is the procedure that maps the basic trajectories of a human model into 3-d coordinates of the junction points shown in Figure 4. The knowledge of the the links length is also needed at this stage. Indeed, this permits to define the position of sternum, shoulder, elbow, hand, head, hip, knee, ankle, and toe, relative to a standing position.

Once the 3-d trajectories of the junction points are known, they can be deployed to emulate radio-frequency or ultrasound backscatters, according to different setup of the input parameters, physical dimensions, and micro-Doppler models. In Figure 5, a sequence of 8 frames is shown regarding the simulation of one walking cycle, and considering: $h_t = 1\,\mathrm{m}$, $v = 1\,\mathrm{m/s}$. The simulation also provides the frontal velocities of a 12 parts body model, as plotted in Figure 6. It shows a set of sinusoidal-like trajectories, which are typical of the human walking gait. Such curves are computed as a combination of the joint speed trajectories, e.g. the foot speed is computed as the mean speed between the ankle and the toe velocities.

2.4 HOUGH TRANSFORM

Hough transform is a diffused algorithm used in computer vision, digital image processing and image analysis. It provides a very helpful method

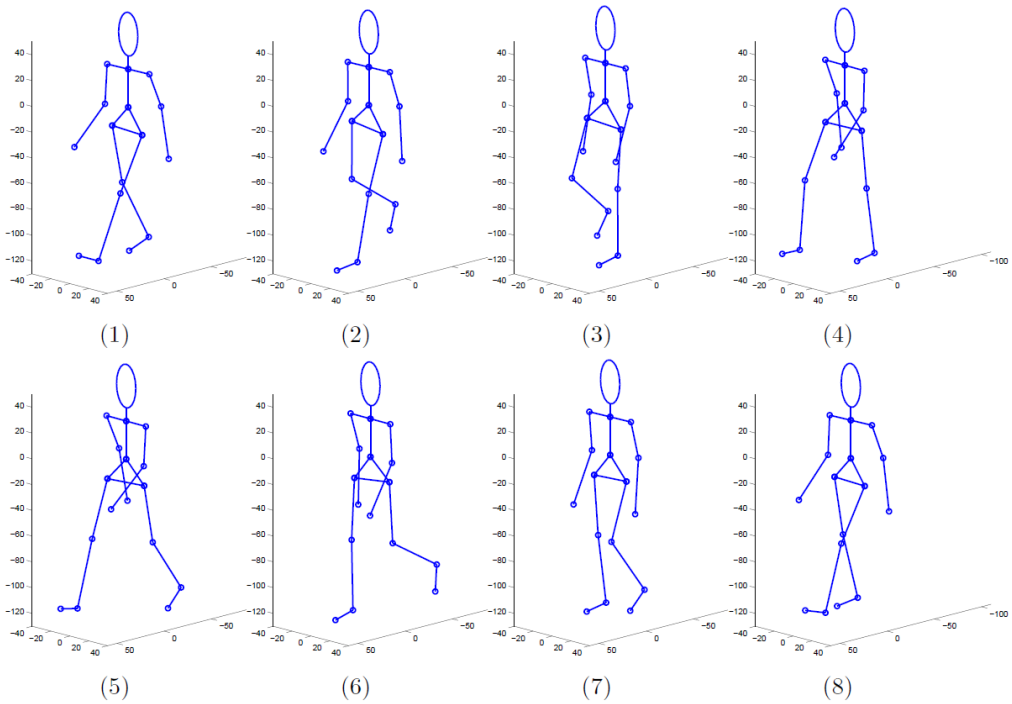

Figure 5: Succession of 8 frames relative to a walking cycle emulated using the BT-model, with $h_t = 1\,\mathrm{m}$, $v = 1\,\mathrm{m/s}$.

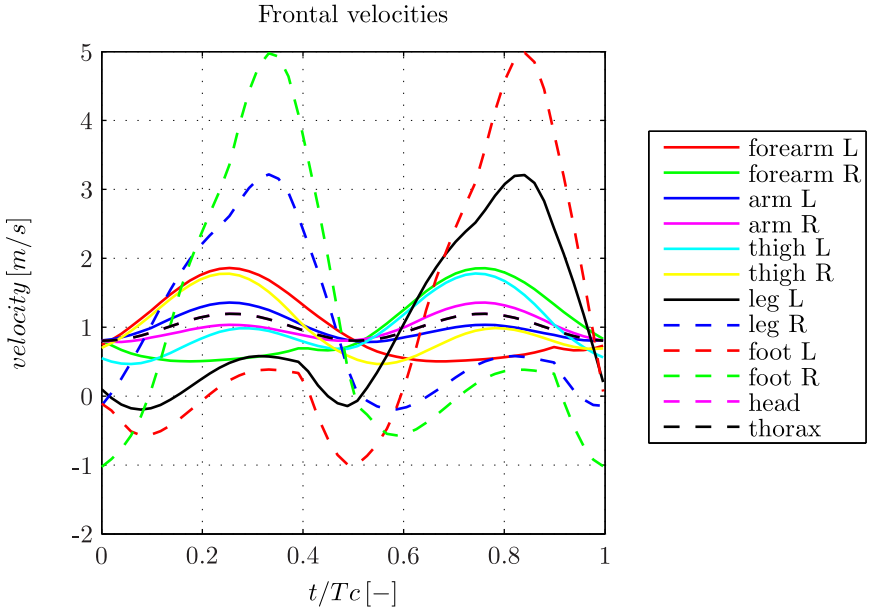

Figure 6: Speed trajectories of a 12 parts body model over a walking cycle of two steps, and using the BT-model with $h_t = 1\,\mathrm{m}$, $v = 1\,\mathrm{m/s}$.

to recognise features of particular shape or pattern within an image. As a pattern recognition tool, it can provide the ability to detect and classify different targets. Information about the target shape is obtained by a voting procedure carried out in a parameter space. Object entities are

detected as a local maxima in the accumulator space, that is directly constructed by Hough algorithm. In a image, most information about an object is contained in the shape of its boundary [45]. For this reason Hough transform is almost always applied on edge images.

2.4.1 *Hough transform procedure*

First step requires the image to be transformed into an edge image. A generic RGB color image will be transformed into a gray-scale image and subsequently the magnitude gradient is computed in order to obtain an edge image. Operators that transform the image in such a way are known as edge operators, among which, Prewitt, Hueckel and Sobel methods are three of the most used. Edge detection performance is affected by the noise level present in the image.

Second step requires a convenient parametric representation of the shape to detect within the analysed image. The choice of the parameters will affect the result of the Hough transform. Indeed, the parameter space dimension is equal to the number of parameters n_p, and computational complexity grows exponentially with n_p. It is important to have a number of parameters as small as possible, and bounded parameters are preferable even though not essential.

Once the equation representing the object to detect has been defined, the n_p-dimensional parameter space must be built. This is accomplished by choosing the variation range and quantisation of each parameter. The range of parameters set some constraints in the voting stage, which can avoid multiple results, obtaining unique solutions. The quantisation level in the parameter space affects the resolution of the recognition task. When in not necessary to determine the shape exactly and a small error is allowed, the computational burden can be reduced [46].

To evaluate the best candidates for pattern (shape) recognition the voting procedure is then performed. The procedure is based explicitly on the parametric equation which describes the shape. Each point of the edge image is mapped into the corresponding curve in the parameter space, according to the object boundary equation. The voting procedure takes place by increasing the count in each cell (bin) along the mapped curve in the parameter space. After all edge points of the figure have been evaluated, the accumulator space is inspected to find local maxima (peaks). A threshold is needed in order to avoid false peaks detection.

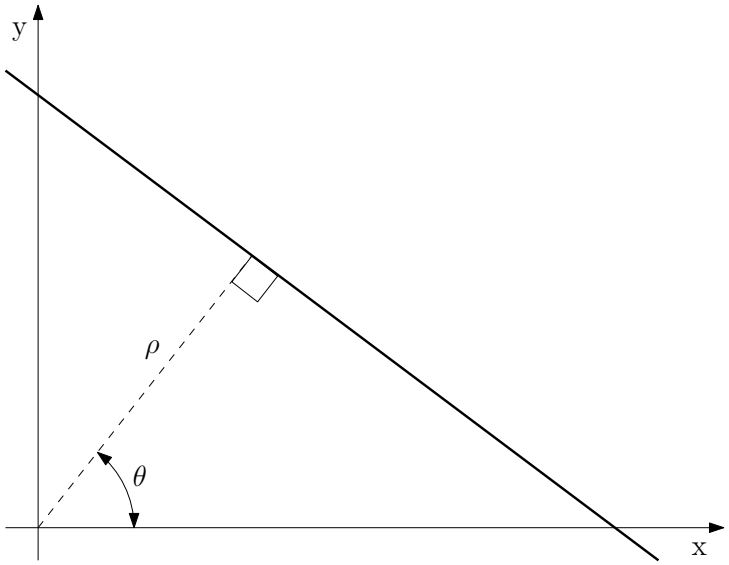

Figure 7: Parametric representation of a straight line used in standard Hough transform.

The results are sensitive to the quantisation of the parameters. A finer quantisation results in a better resolution of the reconstructed shape but increases the computational complexity. Moreover, it can increase the problem of false peak detection. On the other hand, low quantisation can resolve false-matching issues.

2.4.2 *Standard Hough transform*

In digital image processing a common problem is the detection and extraction of straight lines. The issue is to find the presence of groups of co-linear points in the image. Standard Hough transform is an ingenious method for replacing detection problem of co-linear points by an equivalent problem of finding concurrent curves [46]. For this purpose, a mapping is needed from image space to the parametric space. A parametric representation of a straight line must be pondered in order to avoid unbounded parameters and to obtain a parameter space as small as possible. A convenient law to represent a straight line is described by Eq. (10) and plotted in Figure 7; where θ is defined as the angle of the straight line normal, and ρ is the algebraic distance from the origin.

$$\rho = x\cos\theta + y\sin\theta. \tag{10}$$

Usually a straight line in the Cartesian plane is described with two parameters, slope, m, and intercept, q, according to the explicit equation

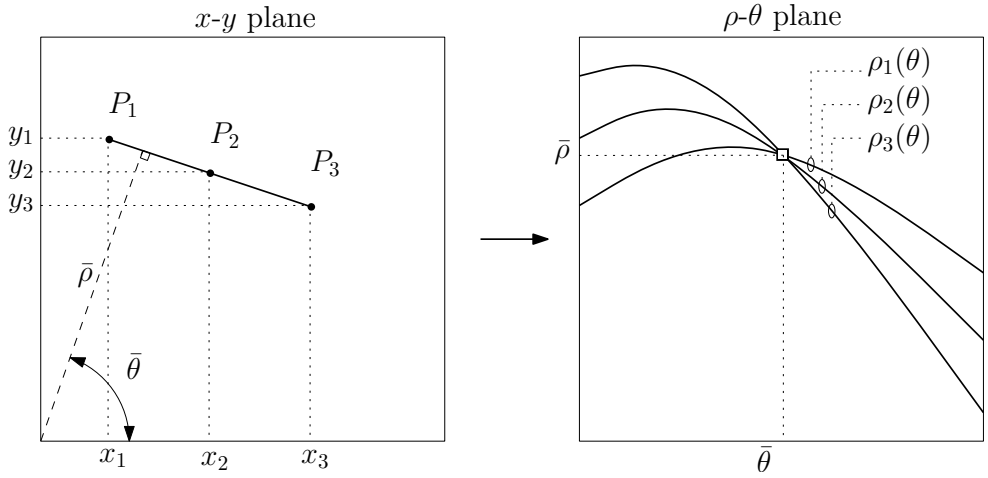

Figure 8: Mapping three co-linear points, P_1, P_2 and P_3 in the parameter space θ-ρ.

$y = m\,x + q$. This mathematical description is lacking from a Hough transform point of view. Both m and q can indeed be unbounded (e.g. in the case of a vertical line), and for this reason this representation is not advisable. According to the parametric equation (10), called *normal parametrisation*, both θ and ρ are bounded. Furthermore, introducing the restriction $\theta \in [0, \pi]$ then for any straight line, normal parameters are unique. In other words, when Hough transform is applied to a picture containing straight lines, each i-th line is mapped into a single point (θ_i, ρ_i) of the parameter space.

Figure 8 represents three co-linear points lined up on the corresponding straight line of parameters $\bar{\theta}$ e $\bar{\rho}$. Each point at coordinates (x_1, y_1), (x_2, y_2) and (x_3, y_3) is mapped into a sine wave within the parameter plane θ-ρ, according to Eq. (10). Resulting sine waves are denoted in Figure 8 as $\rho_1(\theta)$, $\rho_2(\theta)$ and $\rho_3(\theta)$, and they are concurrent at the point ($\bar{\theta}$, $\bar{\rho}$).
As general properties:

1. A point in the image plane is transformed into a sine wave within the parameter plane.

2. A point in the parameter plane corresponds to a straight line in the original image.

3. More points lined up on a straight line are mapped into the parameter space as concurrent sine waves. The intersection point indicates the straight line parameters.

Hence, the problem of finding co-linear points in the picture plan can be transformed into the problem of finding concurrent sine waves in the parameter plan.

A voting procedure is needed to detect potentially straight lines in the picture. The parameters θ and ρ must be quantised according to the desired recognition resolution, as to be $\Delta\theta$ and $\Delta\rho$ respectively. The parameter space is hence discretised in several bins. Each edge pixel of the image has to be mapped into the corresponding set of bins within the parameter space, which is then inspected to find local maxima, representing potential instance of a straight line. A threshold is often employed in order to select the most voted bin and provide robustness to the algorithm. Some a priori information (if available) about straight line parameters are useful in order to tune $\Delta\theta$ and $\Delta\rho$ and to choose a proper threshold level.

2.4.3 *Sine waves classification by Hough transform*

Hough algorithm can be useful even for the classification of sine waves within images. As described in Section 2.3, the human motion trajectories are in the form of sinusoidal-like curves, and hence Hough transform can be suitably applied to classify them.

When a two parameter pattern must be detected, Hough transform is a suitable method from the computation and noise immunity points of view. Although, when the pattern has more than two parameters, like a circle (center coordinates and radius) or ellipses, application of the traditional direct Hough transform algorithm requires too much memory storage and computation. A general sine wave is represented by Eq. (11) and totally described by four parameters: period T, mean value y_0, amplitude A, and initial phase φ. A novel method for breaking down the original problem into two simpler sub-problems is presented in [47]. It requires the knowledge of the sine wave period T which can be estimated through preliminary measurements.

$$y = A\sin(\frac{2\pi}{T}x + \varphi) + y_0. \tag{11}$$

The first step requires the application of 1-dimensional Hough transform to locate mean values of sine waves, y_0. Subsequently, amplitudes and initial phases are estimated in the second step of the algorithm. This is achieved by the application of 2-dimensional Hough transform, for each

mean values found in the first stage. In details, the algorithm implements the following sequence of operations:

1. *Image pre-processing*. The gray-scale image to be analysed is transformed into a BW image. This requires the set-up of a proper threshold level so that to preserve the sinusoidal waveforms to be measured and cut-off the typical background noise surrounding the traces.

2. *First voting procedure (a)*. The BW image resulting from the image pre-processing stage is forwarded to a voting procedure algorithm, which purpose is to map the pixels of the input image into a suitable output vector $v(y)$.

   The voting procedure is applied to each BW image black pixel, $P_{x,y}$, with $x \in \{1, ..., N_x\}$ and $y \in \{1, ..., N_y\}$ and where N_x and N_y are respectively the horizontal and vertical sizes, in pixel unit, of the image. For each $P_{x,y}$, the procedure analyses the column C_x of coordinates $(x + T/2, y)$, and $y = \{1, ..., N_y\}$. From C_x it then extracts the coordinates y_i of black pixels only, if present. For each i, the average coordinate $y_{m,i} = (y + y_i)/2$ is then evaluated and used to provide one vote to $v(y)$. The vote is assigned to the element of $v(y)$ that includes $y_{m,i}$. $v(y)$ is in fact subdivided into a number of N_y/d_y cells, where d_y is the step used to quantise the interval $\{1, ..., N_y\}$. In Figure 9, an example is given regarding this step of the procedure. $P_{x,y}$ is the analysed point, supposed to belong to the sine wave to detect. Then, $P'_{x+T/2,y'}$ is selected at a $T/2$ distance along the x-axis. Supposing that P' also belongs to the sine wave, then the mean y-axis coordinate $(y + y')/2$ provides an estimation of y_0.

3. *Estimation of y_0*. $v(y)$ is then inspected in order to find out its most voted element. The index j of this element, with $j \in \{1, ..., N_y/d_y\}$, is finally used to provide an estimate $\hat{y}_0$ of the mean value y_0 of the analysed sinusoidal curve, according to the following expression: $\hat{y}_0 = j \cdot d_y$.

4. *Second voting procedure (b)*. The BW image is processed again to provide a second output, consisting in a matrix $m(A, \varphi)$, where A and φ are the amplitude and phase of the analysed sine wave. $m(A, \varphi)$ represents a quantised version of A-φ plane, with a $dA \times d\varphi$ step

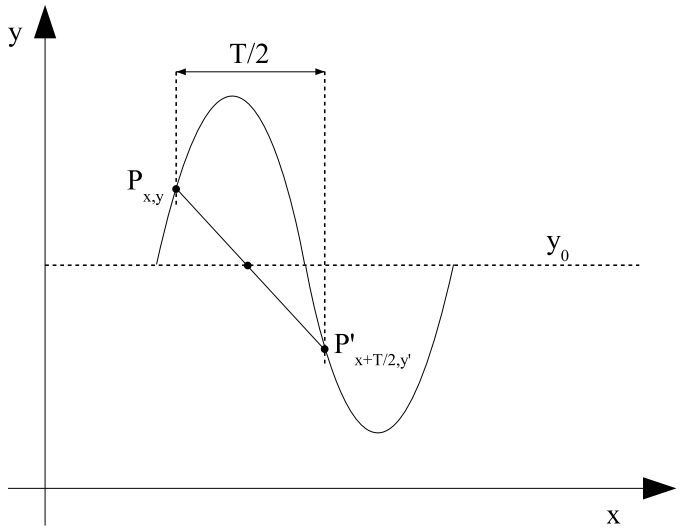

Figure 9: Concept underling the estimation of the mean sine wave value y_0.

size between each matrix element. The mapping of $P_{x,y}$ pixels into $m(A, \varphi)$ is accomplished through the rewritten Eq. (11) as follows:

$$A = \frac{y - \hat{y}_0}{\sin(\frac{2\pi}{T}x + \varphi)}, \tag{12}$$

where $\hat{y}_0$ is the value before estimated. The procedure performs the following operations: for every $P_{x,y}$ and for each φ, a value $\tilde{A}$ of A is computed by using Eq. (12), for $\varphi \in [0, 2\pi]$. The algorithm verifies the presence of $\tilde{A}$ into the range of accepted values, defined as $[A_{min}, A_{max}]$, to be chosen according to some prior information. If $\tilde{A} \in [A_{min}, A_{max}]$, a vote is provided to the corresponding $m(A, \varphi)$ element containing $(\tilde{A}, \varphi)$.

5. *Estimation of A and φ.* The matrix $m(A, \varphi)$ is inspected in order to find out the cell characterised by a maximum score. The most voted bin indexes (i, j) are finally used to estimate A and φ according the following expressions: $\hat{A} = i \cdot dA$, $\hat{\varphi} = j \cdot d\varphi$.

When the algorithm is applied to images containing multiple sine waves, some threshold levels can be used in steps 3 and 5 to distinguish one trace from another or from the noise. In particular, when $v(y)$ is inspected, a threshold level th_{y_0} is set in order to select only the $\hat{y}_0$ estimates characterised by a voting score higher than th_{y_0}. Similarly, in step 5, a threshold level $th_{A,\varphi}$ is adopted to select only the estimations $(\hat{A}, \hat{\varphi})$ characterised by a score higher than $th_{A,\varphi}$.

2.5 MEASUREMENT APPROACH

In this section a measurement approach is proposed for human motion analysis. The aim of the approach is to provide a framework through which better organise, compare and merge further researches, ideas and results. Indeed, following the designed approach, several different measurement campaigns, processing techniques, features extraction algorithms, and classifier will be implemented and performed. For more generality, the approach schematically represented in Figure 10 does not specifically refer to a given application. Nevertheless, the design is technology independent, which means that the measurement operations may be achieved employing different devices and/or technologies. It can be thus considered of interest for a wide range of possible applications, with particular regard to medicine, security and disaster recovery.

2.5.1 *Proposed Approach*

The approach is made of a sequence of operations involving: measurements, micro-Doppler detection, signal conditioning and processing, image processing, human modelling, cinematic modelling. Due to the generality of the approach, the details of the processing techniques and algorithms will be provided within the chapters dealing with measurement campaigns.

In Figure 10, a human under test (HUT) is supposed to walk, run (along the x-axis) or perform a predefined activity in a controlled and predetermined environment, which however may include several unwanted targets, mainly not-moving targets, i.e. stationary clutters. The environment can vary depending on the activity performed by the HUT and on the desired analysis. For example, whenever the walking or running activity is analysed, the setup can be a narrow corridor or a treadmill. As indicated by the circled numbers, six operations are performed:

1. Micro-Doppler scanning. The environment is monitored by a couple of transmitter (Tx) and receiver (Rx) apparatuses. Tx illuminates the HUT with a test wave W_T of proper characteristics, which can be a radar, an ultrasonic or an optic pulse. Rx is instead used to receive from the target a part W_R of W_T energy, backscattered by the HUT. The performance of the overall approach strongly depend on this stage characteristics and setup. In particular, the following characteristics and parameters are to be carefully considered: Rx sensitivity, dynamic range and aperture an-

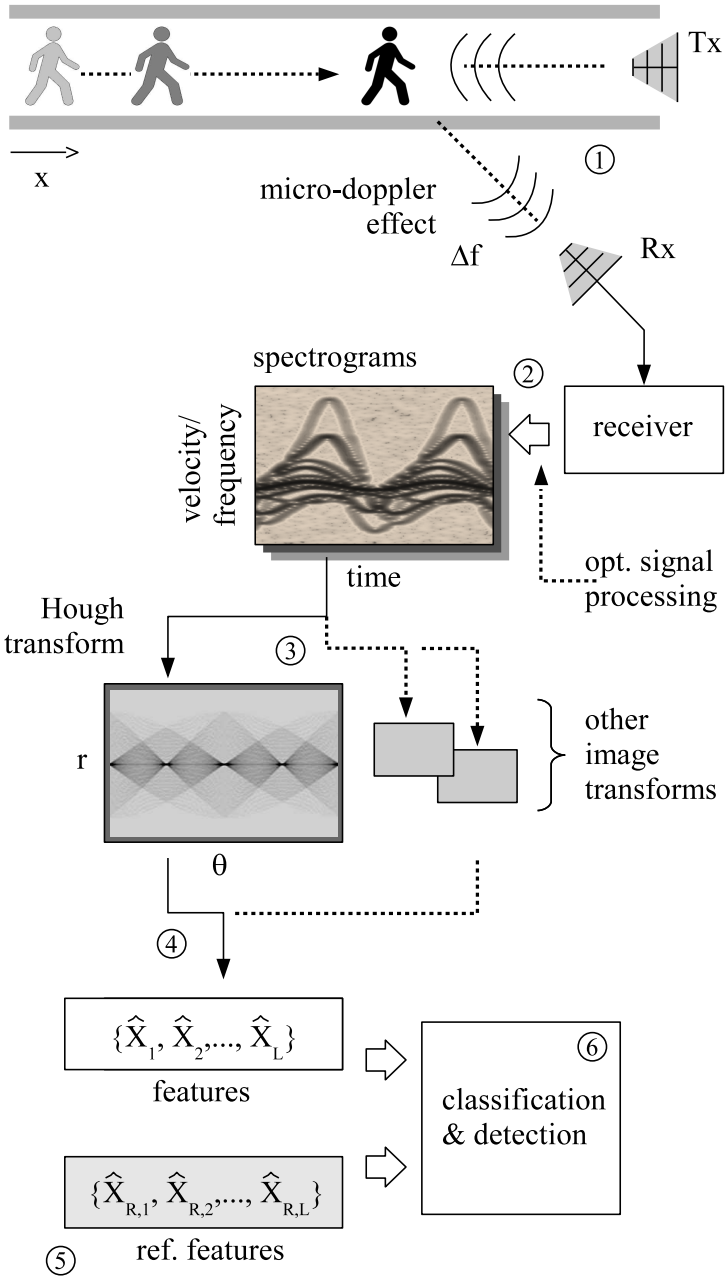

Figure 10: Block diagram of the proposed measurement approach.

gle, Tx output level and aperture angle, background noise and external interference, path setup, angle of aspect between Tx-Rx and HUT, and presence of clutters.

2. Spectrogram The signal acquired at the receiver side is subsequently processed through a Short Time Fourier Transform (STFT) and plotted under the form of a frequency (or velocity) versus time diagram I_0 (spectrogram or micro-Doppler map)[1]. Spectrograms are diagrams that effec-

1 Some pre-processing stages may be needed prior the STFT, e.g. signal filtering, complex demodulation, stationary clutters removal.

tively represent the μ-D signature in a comprehensive way. As can be seen in Figure 10, spectrograms typically appear as a set of sinusoidal-like curves, each associated to a specific body element. The highest amplitude curves are typically those of arms and legs.

Spectrograms are typically complex to analyse and process. The revealed curves are often very close one with another and not so well defined to be easily distinguished and measured (average value, peak value and phase). They are also affected by background noise, which complicates the analysis and degrades accuracy. This requires a careful attention in the setup of STFT parameters such as number of acquired samples, sampling rate, and type of windowing.

3. Image transform In this stage, the incoming spectrogram I_0 is transformed into one or more new diagrams in a image plane, allowing a better isolation and assessment of some target characteristics. The choice of the transformation algorithm strongly depends on the type of target and motion. For example, if the motion is periodical and made of several trajectories, an algorithm to highlight the frequency components of the μ-D signature can be suitably applied. Whenever the μ-D signature is a sinusoidal-like wave, the Hough transform algorithm may be applied to obtain information such as amplitude, mean value and initial phase [47]. The resulting image I_1 is then forwarded to a features extraction algorithm.

4. Features extraction I_1 is then processed to gather a set of features (or parameters) which characterise the micro-Doppler signature, and hence the HUT behaviour. The features have been summarised through L parameters $\{X_1, X_2, ..., X_L\}$. The choice of these parameters is "a key point" for the whole analysis task. It requires an in-depth knowledge of how a given behaviour or characteristic of HUT motion reflects on the displayed images. It also requires to consider impairments and effects typically not simple to analyse, such as distortions, noise and interference (e.g. for the presence of other humans). The expected result from this operation is a set of L estimates $\{\hat{X}_1, \hat{X}_2, ..., \hat{X}_L\}$, which can be seen as another representation of the unknown HUT signature.

5. Reference features estimation Along with the obtained $\{\hat{X}_1, \hat{X}_2, ..., \hat{X}_L\}$, another set of parameters $\{\hat{X}_{R,1}, \hat{X}_{R,2}, ..., \hat{X}_{R,L}\}$ is needed. These $\hat{X}_{R,i}$, with i from 1 to L, are used as reference and comparison for each $\hat{X}_i$. They can be determined in one of the following way: (i) experimentally, through a first scanning of HUT in suitable and well-controlled conditions, that is a sort of calibration or registration stage, (ii) theoretically, through a

simulation analysis; (iii) from a database of pre-determined responses obtained either experimentally or theoretically. The modalities to extract the reference features are described in Sec. 2.5.2, with particular focus on the simulative way.

6. Classification and detection The two sets of values $\hat{X}_i$ and $\hat{X}_{R,i}$ are finally compared and processed to provide a classification and/or a detection of the analysed human motion. Different types of classifiers can be deployed, depending on the features nature (scalars, vectors or mixed) distribution and separability. The success of this task depends on how well all the previous operations have been carried out, as well as on the number of HUT classes to recognise.

2.5.2 *Reference features value estimation*

In Figure 11, a procedure is proposed for the determination of the reference features from the micro-Doppler signature, i.e. $\{\hat{X}_{R,1}, \hat{X}_{R,2}, ..., \hat{X}_{R,L}\}$ to be used as reference for the final comparison and classification. The easiest way to obtain the reference features is through a pre-registration stage. In other words, a part of the gathered μ-D signatures can be processed, the reference features obtained, and hence used to form a database. Whenever a recognition/classification task is needed, the extracted features are compared with the ones picked up from the database.

Alternatively, the reference values can be obtained through a simulation analysis. The procedure can be subdivided into three steps. Firstly, a cinematic model of the human behaviour is simulated in terms of position and velocity, e.g. by adopting the BT-model described in Section 2.3. A walking model of the analysed type of target is applied and some basic trajectories obtained. A starting set of M input parameters describing the target $\{p_1, p_2, ..., p_M\}$ is needed for this task. The obtained basic trajectories are subsequently processed by suitable cinematic model expressions to obtain a set of spatial coordinates of the body elements along the whole path. Velocities are subsequently determined by a time-derivative stage, in the figure denoted as *d/dt*.
In the second step, the micro-Doppler response is simulated and spectrograms are obtained. The behaviour of the micro-Doppler Tx-Rx system of Figure 10 is analysed by using the expressions recalled in Sec. 2.2. The accuracy of this computation depends on the approximation degree through which each single part of the body and the surround-

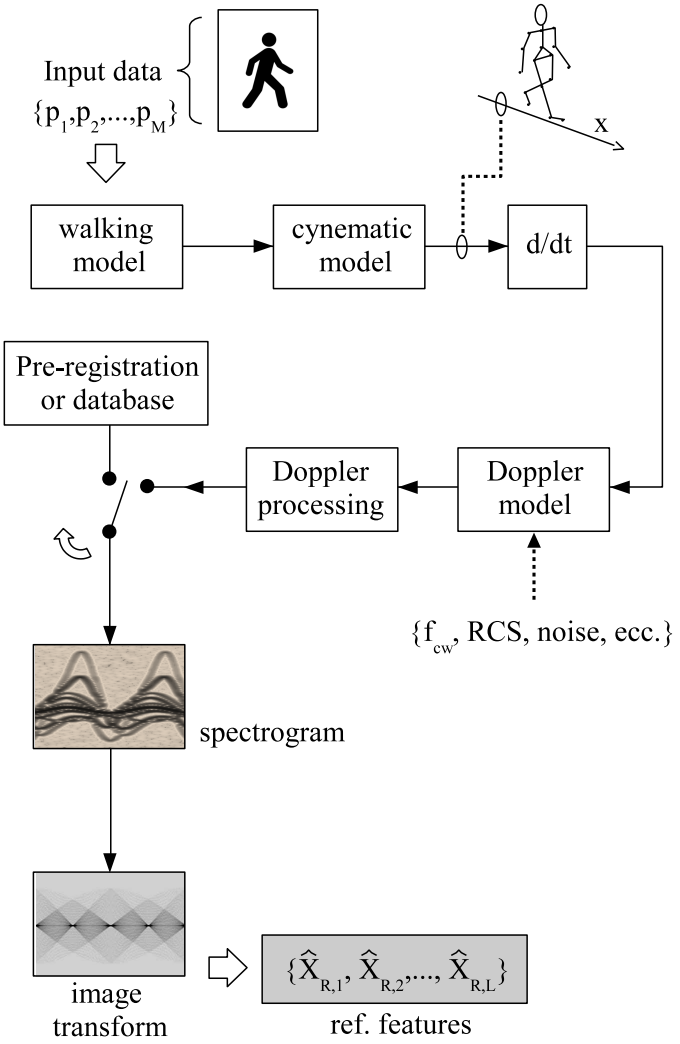

Figure 11: Proposed procedure for the generation of reference responses $\{\hat{X}_{R,1}, \hat{X}_{R,2}, ..., \hat{X}_{R,L}\}$.

ing environment are accounted for. Another important parameter is the frequency band and the waveform used to illuminate the target, which strictly affects system resolution. A background noise is also to be considered emulating the presence of interference or impairments from the surrounding environment. The radar return from the moving HUT is finally achieved and mapped into spectrograms.
In the third step, the final image transform provides a new set of images, from which the L final reference values $\{\hat{X}_{R,1}, \hat{X}_{R,2}, ..., \hat{X}_{R,L}\}$ are achieved.

2.5.3 *Example of reference features generation*

A number of tests have been conducted with the purpose of verifying the potentialities of the proposed approach at the begging stage. In par-

ticular, attention has been focused on the procedure for the generation of reference responses using a human walking model. In this section, the procedure has been applied for two different humans, here denoted as hut_1 and hut_2. Both targets are assumed identical and walking at the same velocity $v = 1.5\,m/s$. The only difference is the height, 1.4 m for hut_1 and 1.9 m for hut_2. The trajectories of the body elements have been simulated by using the BT-model. Hence, the procedure shown in Figure 11 has been employed considering: $M = 2$, $p_1 = v$, and $p_2 = h_t$, where h_t is thigh's height (from ground to the hip). The dimensions of the body parts have been gathered from an on-line available anthropometric database [48]. Proportionally to the HUTs height, h_t is 0.8 and 1.08 m, respectively for hut_1 and hut_2.

The μ-D model has been applied considering a human body model composed of 12 parts, as shown in Figure 12. Thus, the emulated radar received signal has been computed as a superposition of $N = 12$ contributions, where each body part is considered a point scatterer located at the median point. Furthermore, the following radar model setup has been chosen:

1. CW radar emitting at a carrier frequency, $f_c = 20\,\text{GHz}$;
2. negligible background noise and multipath effect;
3. no clutters present in the emulated scene;
4. HUTs approach the radar at a 0° aspect angle, i.e. the LOS overlaps the radar pointing direction;
5. The radar cross section value RCS_n for the n-th body part has been considered equal to $RCS_n = rcs_n \cdot S_{hut}$; where S_{hut} is the total surface of the body, assumed equal to 1 m^2, and rcs_n is the fraction of S_{hut} associated to the n-th body part, computed from the adopted human sizes database;
6. the radar-target distance is supposed to be much greater than the target displacement (in two steps), hence the variability of the signal power has been neglected.

Based on the chosen setup and hypotheses, the emulated baseband signal received by the radar, $s_{rx}(t)$ can be computed considering the μ-D theory described in Section 2.2, as summation of each body part contribution:

$$s_{rx}(t) = \sum_{n=1}^{N=12} RCS_n \exp\left\{ j\frac{4\pi}{\lambda_c} \int_0^t v_{r,n}(t)dt \right\}, \tag{13}$$

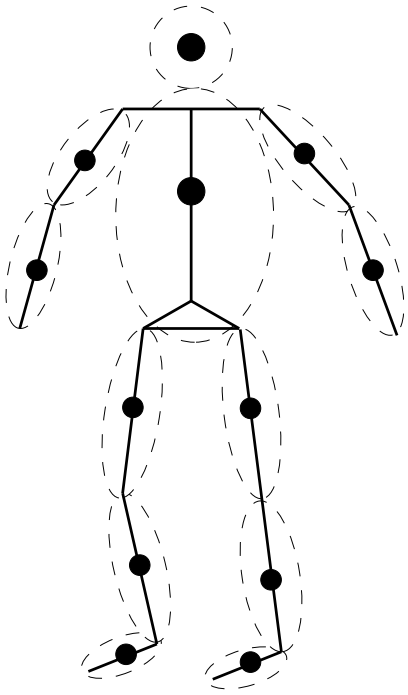

Figure 12: Human model composed of 12 parts for radar return emulation [2].

where $v_{r,n}(t)$ represents the velocity of the n-th body part midpoint. In the equation, the amplitude of each term is considered equal to its RCS, preserving the power ratio among the signals of each contribution. Indeed, the aim is to highlight the difference among each body part and the respective trajectories.

In Figure 13a and 13b, the results obtained from the Micro-Doppler processing are shown under the form of spectrograms, respectively for hut_1 and hut_2. Spectrograms have been obtained using a 0.01 s time window, choosing an overlap equal to 90%, and finally the result has been normalised with respect to its maximum amplitude value. In the figures, frequency and time are replaced by v and t/T_c to improve readability, where t is time and T_c the cycle time needed for a couple of steps. T_c can be assessed by measuring the periodicity of the acquired samples. In the considered case, T_c is 0.985 s for hut_1 and 1.143 s for hut_2. In the figure, only some curves have been labelled to improve clarity.

From the two spectrograms, a number of considerations can be addressed:

1. the response of the system is a bundle of periodic curves, each associated to a specific body element, and varying with a period T_c;

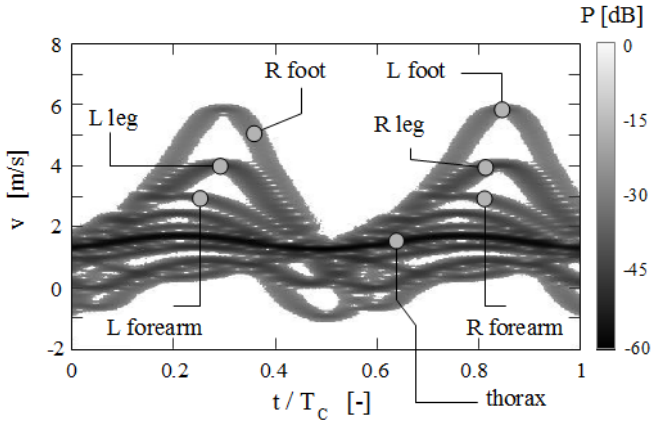

(a)

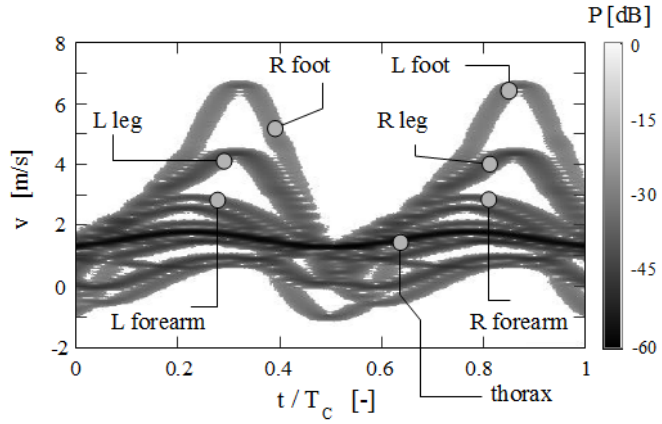

(b)

Figure 13: Spectrogram representation of the emulated radar return, for: (a) hut_1; (b) hut_2.

2. the curves are sinusoidal-like for an half period ($T_c/2$), in agreement with the BT-model (Figure 6);

3. the ones associated to the right (R) and left (L) elements are very similar one with another, and shifted by $T_c/2$;

4. the curves amplitude changes from one body element to another: it is higher for feet, legs and forearms;

5. the distinction of the curves and the measurement of their parameters is not clear and simple, especially for the body parts oscillating slowly;

6. the curves have a different gray scale intensity (0 dB reference level), that means a different received wave intensity (the darker the curve

the higher the intensity). This intensity is higher for the body parts having a larger surface (*e.g.* the chest), and lower for the smaller ones;

7. the average value of the thorax trajectory is nearly 1.5 m/s; this is a measure of the walking velocity;

8. the forearms and legs oscillate slower in hut_1 with respect to hut_2;

9. the bundle of curves resembles the typical "eye patterns" of electronics and telecommunication analyses, used for troubleshooting of digital signals and devices;

10. the "eye pattern" associated to hut_1 is closer than hut_2 one; in particular the difference between forearms and legs maximum velocities is lower for hut_1 with respect to hut_2.

The spectrograms have been subsequently processed through the Hough transform algorithm described in Section 2.4.3. The aim is to reconstruct some sinusoidal-like trajectories of the μ-D signatures, and extract a set of features describing the HUTs. For each n-th detected sinusoidal curve, the algorithm measures: the mean value $y_{0,n}$, the amplitude A_n and the initial phase φ_n. From the estimated values, the sine waves associated to the spectrogram curves can easily be plotted, as shown in Figure 14a and 14b. They represent a typical example of the proposed approach final output. Some considerations can be drawn:

1. spectrogram curves can now be clearly distinguished and measured in terms of amplitude, phase and average value;

2. R and L spectrograms curves appear now merged into a same sine wave;

3. further parameters can be measured, for example: Δv and Δt, where Δv is the difference of the velocity between forearms and feet, and Δt is the phase shift measure between them;

4. Δv is higher for hut_2 with respect to hut_1, while Δt is smaller for hut_2 with respect to hut_1. This shows that the legs of hut_1 are not perfectly synchronised with the forearms (higher Δt), and the velocity of the legs is closer to the one of forearms (lower Δv). These results can be viewed as a sign that hut_1 is struggling more than hut_2 in the attempt to walk at the average velocity of 1.5 m/s;

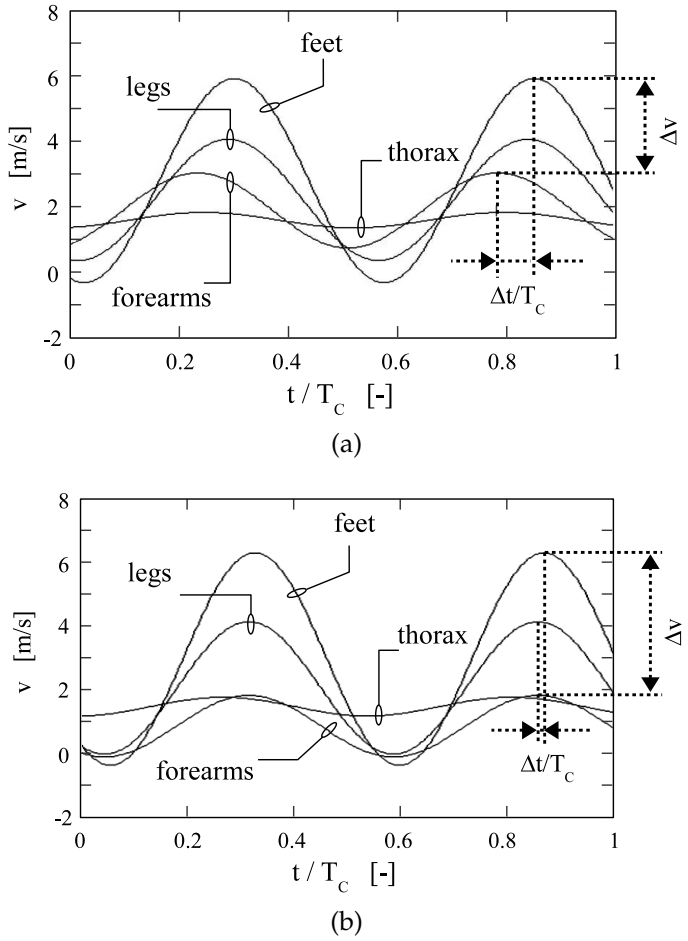

Figure 14: Final sinusoidal waves obtained through the Hough transform application to: (a) spectrogram of Figure 13a (hut_1); (b) spectrogram of Figure 13b (hut_2).

5. Δv and Δt can be thus considered as meaningful indexes for deducing information about the height of a target or about the walking gait (relaxed or troubled, calm or hurried, injured or not injured, etc.).

In Table 1, some of the parameters (features) associated to the sinusoidal traces displayed in Figure 14a and 14b are shown, for the four analysed body parts. In each cell, three values are reported: $y_{0,n}$ [m/s], A_n [m/s] and φ_n [rad]. The obtained ΔV and Δt values are also provided. Results in the table are examples of the features $\{\hat{X}_{R,1}, \hat{X}_{R,2}, ..., \hat{X}_{R,L}\}$ that can be deduced by applying the proposed procedure, and can be used as reference for human motion detection and analysis purposes.

Table 1: Estimated features from the diagrams of Figure 14a and 14b.

	hut_1	hut_2
feet	(2.76, 3.12, 4.32)	(3.22, 3.28, 4.06)
legs	(1.87, 2.17, 4.38)	(2.22, 2.05, 4.76)
forearms	(1.61, 1.89, 4.44)	(1.12, 1.75, 5.58)
thorax	(1.56, 0.23, 5.46)	(1.58, 0.23, 4.88)
$\Delta V\ [m/s]$	1.84	2.23
$\Delta t\ [s]$	$0.064T_c$	$0.03T_c$

3

DESIGN AND CHARACTERISATION OF AN ULTRASOUND DOPPLER SYSTEM

In this chapter, the measurement approach introduced in Chapter 2 is tested in the case of ultrasounds. To this aim, an Ultrasound Doppler System has been designed, checked on a rapid prototyping platform and then manufactured with the aid of an electronic CAD. The system is composed of a receiver-transmitter couple, capable of transmitting different waveforms and collecting the backscattered signals. The ultrasound system has been then characterised by a suitably build measurement setup. A proper reference target has been realised, and the speed estimation error has been quantified in various test cases. In the last part of the chapter, some preliminary measurements are reported, regarding the acquisition of human gait signatures, performed by using the ultrasound system, and according to different measurement conditions.

3.1 DESIGN OF THE ULTRASOUND TRANSCEIVER

With the aim to apply the measurement approach described in Chapter 2, an ultrasound transceiver has been designed and manufactured. It is made up of a transmitter (Tx) and a receiver (Rx) board, and its main purpose is the collection of micro-Doppler signatures induced by the human motion. The couple Tx-Rx constitutes a module, named Ultrasound Doppler System (UDS). Even though at the design stage there were not strict specifications, some requirements have been set. In particular, the UDS should have the enlisted features:

1. Tx transmits at a carrier frequency far enough from the human hearing frequency range (up to 20 kHz) to not disturb and influence the human under test.

2. The transducer and sensor, mounted respectively on the Tx and Rx boards must have a wide beam/aperture angle, i.e. wide radiation patterns. This to ensure a total illumination of the human target and to gather the backscatter coming from the whole body.

3. The UDS should operate up to a distance of 5 m. Usually, the working range of ultrasound systems does not extend beyond few tens of meters [17].

4. Tx maximum carrier frequency is lower than 100 kHz. This is correlated to requirements 2 and 3. Indeed, the attenuation of ultrasounds in air medium increases at higher wave frequencies. Furthermore, generally, the higher the working frequency of the transducer/sensor the narrower the beam/aperture angle.

5. The Tx carrier frequency should be slightly tunable in order to work at the exact resonance frequency of the transducer, maximising the output sound pressure level. This also allows the employment of more UDS modules at the same time. Tuning them at different frequencies can allow to gather multiple μ-D signatures of the target from different points of view.

6. Tx should include two modes of operation: (i) emission of a continuous sinusoidal wave to analyse the target-induced Doppler effect; (ii) emission of a pulsed sine wave to allow range measurements.

7. Rx should embed a low-noise high gain amplifier to augment the received ultrasound wave. The Rx board should also include a filtering stage to eliminate the continuous component of the signal, and attenuate the high frequency noise coming from the environment.

Focusing on the ultrasound transducer and sensor, the choice has been directed toward the piezoelectric technology. Piezoelectric devices are widely diffused and cover a various range of application, e.g. microphones, accelerometers, strain/force measurement systems, mechanical actuators etc. They are based on the piezoelectricity working principle: if a mechanical stress is applied to a piezoelectric material an electric charge accumulation is caused. On the contrary, if a differential voltage is applied across a piezoelectric element, mechanical strains are induced. In other words, a piezoelectric element can convert mechanical energy into electrical energy and vice versa.

Among the plenty of possibilities about the design options, the following set of key components/features has been chosen for the Tx and Rx implementation:

- the oscillator (Tx) is realised by employing the largely used NE555 Timer to produce a square wave signal. A variable RC network is employed for the fine tuning of the square wave frequency.

- A jumper is placed on the Tx board to switch between the *continuous mode* (sine wave) and the *pulsed mode* (pulsed sine wave).
- A MA40S4S and a MA40S4R Murata piezoelectric devices have been employed respectively for the ultrasound transducer and sensor. They are characterised by a narrow frequency response, centred at nearly 40 kHz, and a wide beam/aperture angle equal to 80°. According to the characterisation conditions pointed out on the datasheet (Appendix A), the transducer can deliver a 120 dB sound pressure level (at 30 cm), while a maximum voltage of 20 V_{pk-pk} can be applied to the electrodes. The sensor has a sensitivity of -63 dB.
- Rx employs a MC33178 low noise operational amplifier manufactured by ON Semiconductor®. It is characterised by a 5 MHz gain-bandwidth product and a 2 V/μs slew rate. It supports a dual supply voltage up to $\pm$18 V.
- The Rx board embeds a bandpass filtered analog output.

Further details about the chosen key components can be found in the datasheets reported in Appendix A.

3.1.1 *Bandpass filter design*

Between the MC33178 amplifier and the Rx board output, a bandpass filter has been designed and inserted to remove the Direct Current (DC) component and cut off the high frequency environmental noise. Such a filter must preserve the signal in correspondence of the sensor working frequency, i.e. around 40 kHz. In order to obtain a flat characteristic at the working frequencies, a only-capacitor topology has been chosen for the bandpass filter, as sketched in Figure 15. The elements C_d and R_4 constitute the high-pass part of the filter, while C_f and R_5 work as a low-pass filter. From Figure 15, the $v_{out}(s)/v_{in}(s)$ Laplace transfer function can easily be computed as:

$$\frac{v_{out}(s)}{v_{in}(s)} = \frac{s\, R_5 C_d}{s^2\, R_4 R_5 C_d C_f + s\,[(R_4 + R_5)C_d + R_5 C_f] + 1}. \tag{14}$$

According to the topology, the filter presents a low and an high cut-off frequency, which values are influenced by the passive components R_4, R_5, C_d and C_f. The following commercial available values have been chosen:

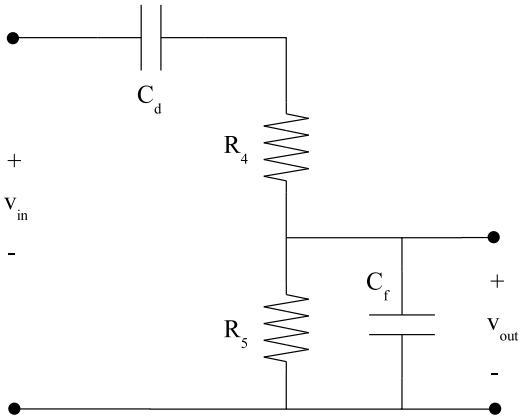

Figure 15: Topology of the designed bandpass filter to embed within the *Rx* board.

$R_4 = 2.2\,\text{k}\Omega$, $R_5 = 82\,\text{k}\Omega$, $C_d = 10\,\text{nF}$ and $C_f = 100 + 47 = 147\,\text{pF}$. In Figure 16, the bode plot of the transfer function described by Eq. (14) is shown, computed with the chosen components value. The low and high cut-off frequencies are nearly equal to 186 Hz and 512 kHz respectively. At a 40 kHz frequency (UDS carrier frequency), the filter gain is nearly -0.37 dB, while the phase shift is equal to -4°. The bandpass region has been chosen to be wide enough in order to: (i) obtain a low attenuation of the received signal; (ii) keep the possibility to slightly vary the working frequency.

The filter transfer function has been experimentally verified as well. The circuit of Figure 15 has been implemented on a breadboard, and its input supplied by a signal generator characterised by a 50 Ω output impedance. The latter one provides a sinusoidal waveform of 5 V_{pk-pk}. The output voltage has been measured while the input signal frequency has been discretely varied within the range [10 Hz, 10 MHz]. The experimental frequency response of the filter is displayed in Figure 17. A good agreement with the theoretical Bode diagram can be noticed. The designed bandpass filter shows a slight attenuation in the working region, the ability to eliminate the continuous component and cut off the high frequency noise.

3.1.2 *Electronic CAD project*

The *Rx* and *Tx* boards have been designed by using Kicad, an open-source electronic CAD. The realised transmitter schematic is plotted in Figure 18. The core component is the oscillator, realised by employing a

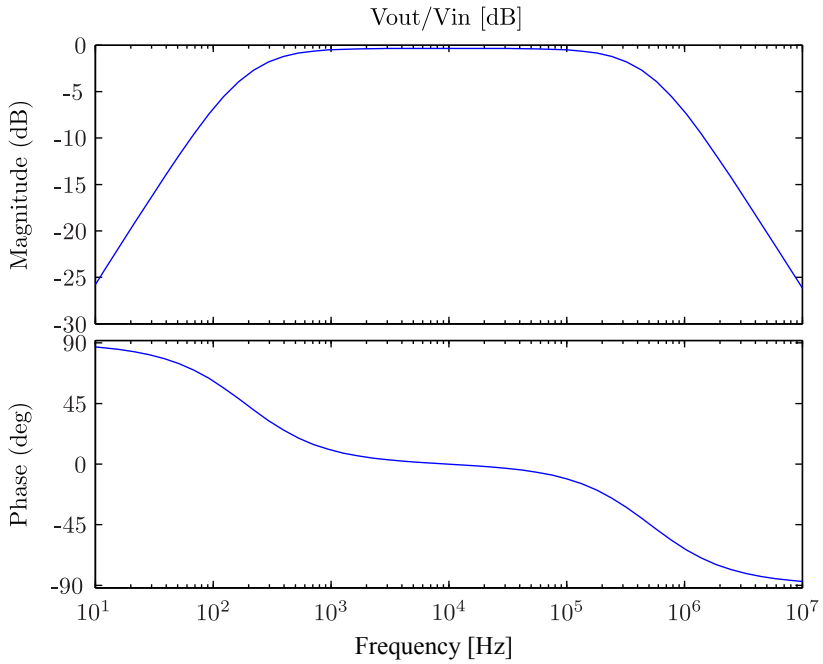

Figure 16: Bode diagram of the designed bandpass filter computed in Matlab.

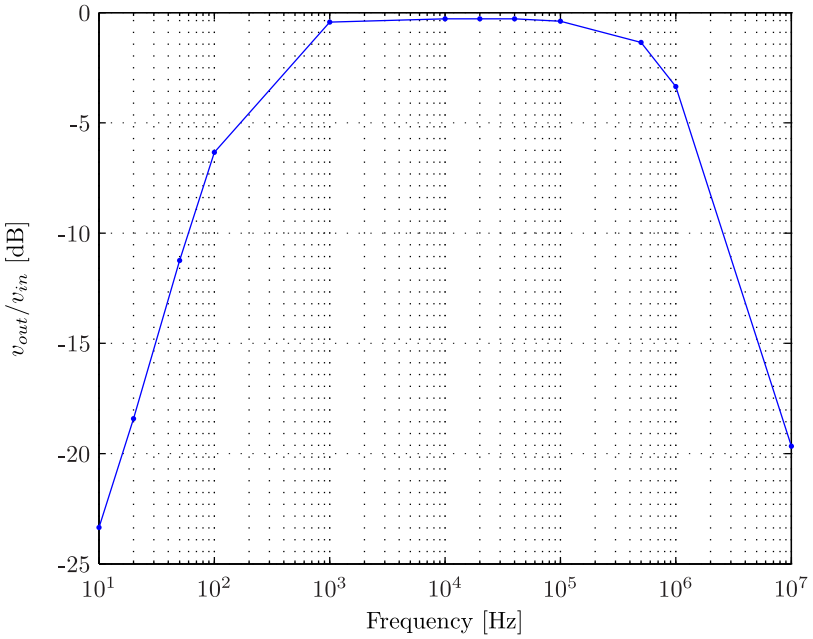

Figure 17: Experimental frequency response of the designed bandpass filter.

NE555 Timer in the astable configuration. In this case, the device acts as multi-vibrator, providing a square wave at the *out* pin. As specified on the datasheet, and referring to the components displayed and labelled on

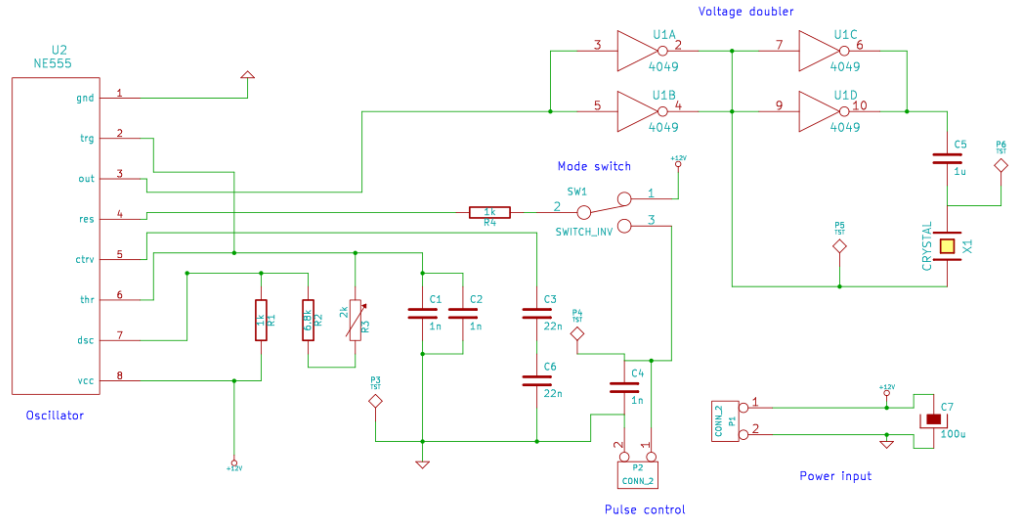

Figure 18: Schematic of the Tx circuit.

the schematic, the generated sine wave frequency f_{sq} can be computed as:

$$f_{sq} = \frac{1.44}{(R_1 + 2\,(R_2 + R_3))\,(C_1 + C_2)}. \tag{15}$$

In the Tx schematic, R_3 is a variable resistor which allows to tune the produced oscillation. With the employed components, the maximum and minimum excursions of f_{sq} are nearly equal to 49.1 kHz ($R_3 \simeq 0\,\Omega$) and 31.8 kHz ($R_3 \simeq 4\,\text{k}\Omega$) respectively. The duty cycle of the square wave is included between 47% and 48%.

The *mode switch* allows to set the operation mode as *continuous wave* or *pulsed wave*. The pulses can be controlled through an external connector by using any TTL-compatible device. The NE555 output is forwarded to a voltage doubler network, consisting of 4 NOT ports connected as displayed in Figure 18, which then supply the piezoelectric transducer.

In Figure 19, the receiver schematic is displayed. The main component is the MC33178 high gain-bandwidth product operational amplifier. The piezoelectric sensor picks up the incident ultrasonic wave and converts it into an electric signal. One end of the sensor is connected to the not-inverting pin of the MC33178, which is configured as a not-inverting amplifier. In this configuration, the achieved signal gain is nearly equal to $1 + R_2/R_1$, and according to the chosen component values it corresponds to a 40 dB gain. The amplifier output is finally forwarded to the previously designed bandpass filter.

After some tests carried out on the breadboard, the Printed Circuit Boards (PCB) have been manufactured at the University's laboratory. In

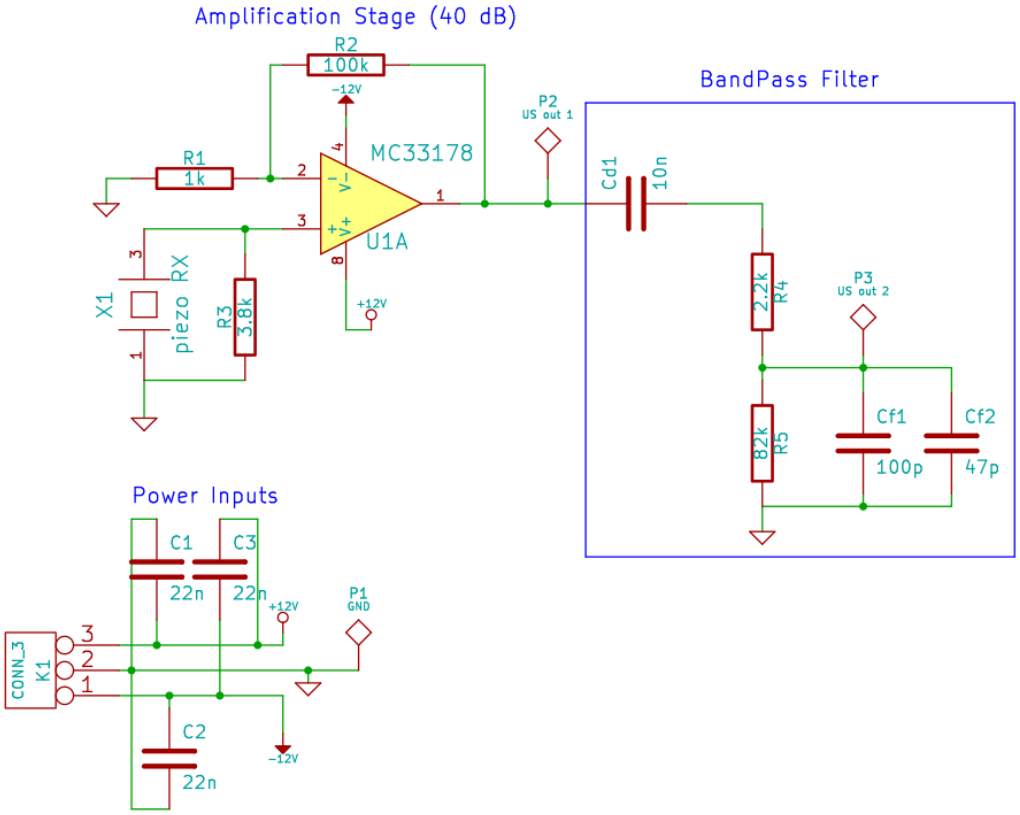

Figure 19: Schematic of the *Rx* circuit.

Figure 20, the 2D and 3D renderings of the *Tx*/*Rx* boards are shown. The dimensions of the realised PCBs are nearly 62x40 mm and 55x30 mm, respectively for the *Tx* and *Rx* board. Finally, in Figure 21, a couple of pictures of the manufactured devices is shown.

3.1.3 *Test of the boards*

A total number of 3 *Tx* and 3 *Rx* boards have been manufactured, to be assembled in 3 UDS modules. Each *Tx*-*Rx* pair has been mounted on a wooden board of dimensions 6x20 cm. In order to reduce the transmission of mechanical vibration, 4 rubber anti-vibration pins have been interposed between *Rx*/*Tx* and the wooden frame. Finally, on the back of the wooden frame, a couple of clamps has been fixed to easily mount the modules on a vertical aluminium pole.

Some preliminary tests have been achieved to check the functionality of the device. To this purpose, two UDS modules have been mounted on two different poles, faced at a distance of 2 m, and at a 1.5 m height from the floor. The following equipments have been also deployed:

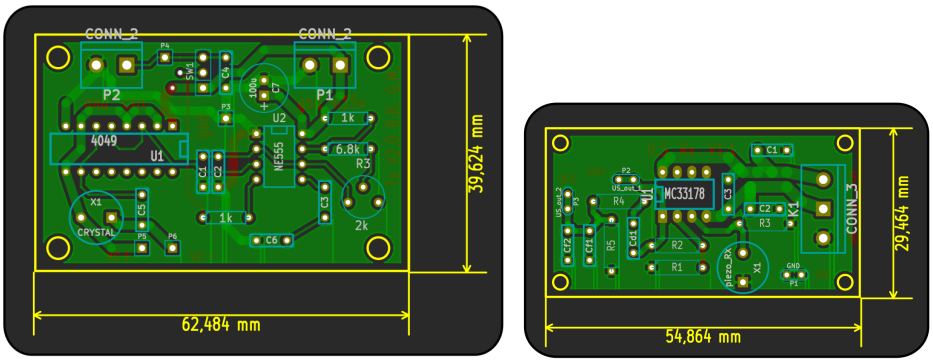

(a) (b)

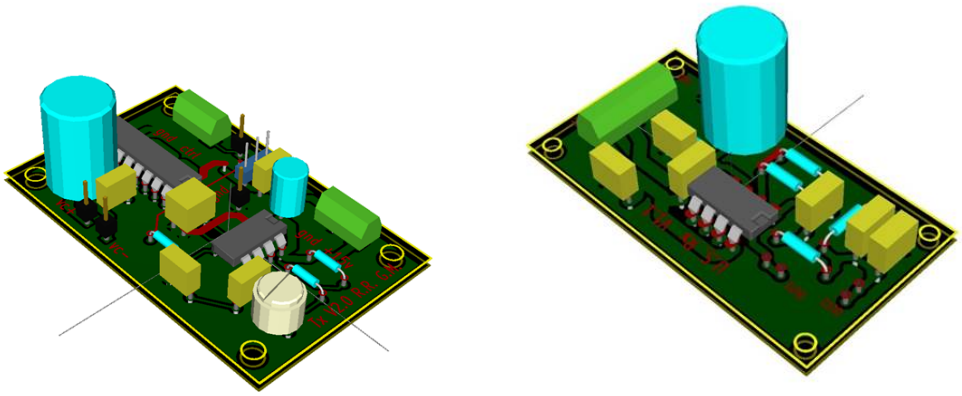

(c) (d)

Figure 20: Rendering of the realised PCBs: (a) 2D plot of the *Tx* board; (b) 2D plot of the *Rx* board; (c) 3D rendering of *Tx* board; (d) 3D rendering of the *Rx* board.

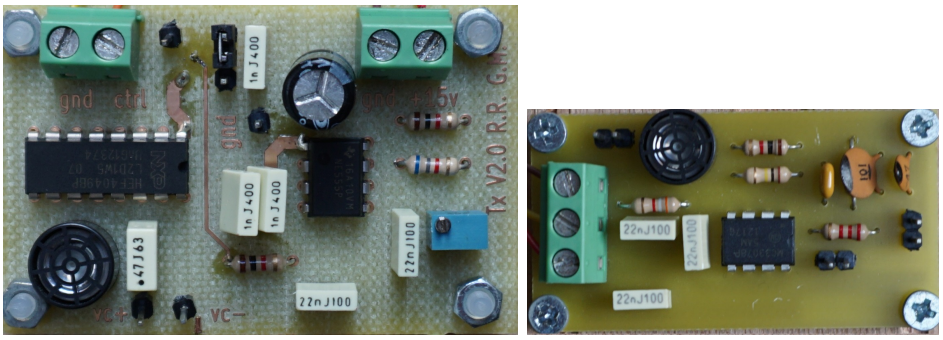

(a) (b)

Figure 21: Pictures of the manufactured PCBs: (a) transmitter; (b) receiver.

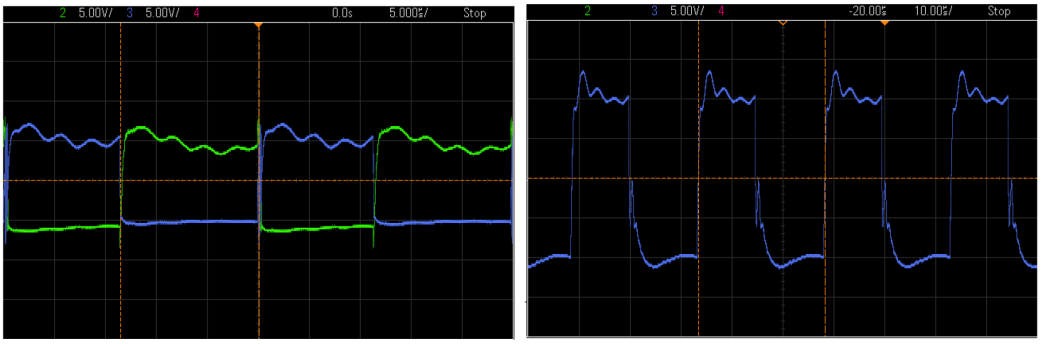

(a) (b)

Figure 22: Oscilloscope screenshots of the Tx board signals (5 V/div): (a) voltage between the positive transducer lead and ground (green trace), and voltage between the negative transducer lead and ground (blue trace); (b) differential voltage applied to the piezoelectric transducer.

1. a stabilised power supply Gwinstek GPS-4303. It provides a 12 V supply voltage to the Tx boards and a dual supply voltage (+12 V and -12 V) to the Rx boards.

2. a Digital Signal Oscilloscope (DSO) LeCroy HRO 64Zi to acquire the test signals. It is characterised by a maximum sampling frequency of 2 GS/s, a 400 MHz bandwidth, and a resolution of 12 bits.

During these tests, only one transmitter and one receiver have been switched on. In particular, said UDS_1 and UDS_2 the two facing modules, only $\text{UDS}_{1,Tx}$ and $\text{UDS}_{2,Rx}$ have been working during the tests, so that $\text{UDS}_{2,Rx}$ directly receives the wave emitted by $\text{UDS}_{1,Tx}$.

In a first experiment, the UDS has been set in *continuous wave* mode. Once plugged to the power supply, the Tx board shows a current absorption of nearly 30 mA, as displayed on the Gwinstek GPS-4303. In Figure 22a, the voltages supplying the transducer (Tx board) are shown (5 V/div). In details, the green trace represents the voltage between the positive transducer lead and common ground, while the blue trace is the voltage between the negative transducer lead and ground. As expected, the two square waves are time shifted of half period, and the peak-to-peak voltage is nearly 12 V. In Figure 22b, the differential voltage applied to the transducer is shown (5 V/div). The voltage doubler circuit works properly as the resulting signal has an amplitude nearly equal to 20 $\text{V}_{\text{pk}-\text{pk}}$.

Table 2: Peak-to-peak voltage measured on the Rx board upon the variation of the transmitting frequency.

f_{sq} [kHz]	$V_{Rx,pk-pk}$ [V]
37.0	0.42
39.0	3.22
40.0	6.53
40.3	7.04
40.5	**7.73**
41.0	6.23
42.5	2.53

A second test has been performed for the tuning of the transmitter carrier frequency, with the aim to maximise the received signal amplitude. To this purpose, the potentiometer R_3 (see schematic of Figure 18) of the Tx board has been adjusted to set different working frequencies, and for each setup, the peak-to-peak voltage of the Rx signal has been measured ($V_{Rx,pk-pk}$). In Table 2, the results of the test are summarised. As specified on the datasheet (Appendix A), the sound pressure/sensitivity curves of the transducer/sensor are centred at a frequency between 40 and 41 kHz. A value of 40.5 kHz has been experimentally measured to be the transmission frequency maximising the received signal amplitude. From Table 2, it can be notices how a +/- 2 kHz variation of f_{sq} causes a 1/3-1/5 decrement of the received voltage. This is due to the narrow frequency characteristic of the employed ultrasound transducer and sensor.

A third test has been performed setting the Tx board in the *pulsed wave* operation mode. Pulses have been generated by an Arduino Uno, a rapid prototyping platform based on a Atmel microcontroller. The Arduino has been programmed to generate a series of 35 ms duration pulses, with a repetition frequency equal to 14.3 Hz. The signal from Arduino is forwarded to the *pulse control* port of the Tx board, controlling the state of the NE555 *reset* pin, and hence the generated square wave. As shown in Figure 23, the received signal (magenta) is delayed with respect to the transmitted one (green). The delay is approximately equal to 6 ms, which is the flight time needed to cover the Tx-Rx distance. Considering a sound propagation speed of 343 m/s (temperature 20° C), it corre-

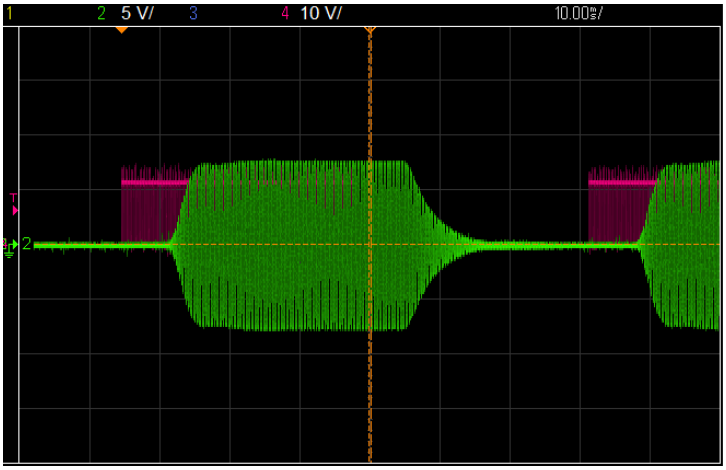

Figure 23: Oscilloscope screenshot relative to the *pulsed wave* operation mode. The magenta trace represents the transmitter signal (10 V/div), while the green trace is the received signal (5 V/div).

sponds to a distance of 2.06 m, very similar to the setup distance (2 m).

3.2 CHARACTERISATION OF THE ULTRASOUND DOPPLER SYSTEM

The developed UDS has been characterised through an experimental setup, as displayed in Figure 24. A metallic frame holds an UDS module, posed at a distance d from a stepper motor, spinning a small sphere (radius 10 mm) through a thin wool wire of length l_w. The motor-sphere sub-system has to be considered as a reference target, emulating the motion of a generic human body part, i.e. swinging of an arm. The reference sphere moves along a circular path of radius r, at a constant adjustable speed ω. l_w and d can flexibly be adjusted to account for different measurement conditions. Rx and Tx signals are then collected and processed in order to reconstruct the μ-D signature induced by the target motion. The stepper motor is driven by a cheap controller, which receives the speed set-up from a ZigBee module. Another ZigBee module connected to a laptop permits the remote speed adjustment, as shown in Fig. 24. Because of the gravity force effect, the radius r is lower than the wire's length. For this reason, r is measured using a ruler and an alignment system. In particular, two pendulums are fixed on the superior beam holding the stepper motor. Each pendulum is realized by a very thin plastic wire hanging a small weight. While the ball is stably rotating, the pendulums are accosted to the circular path until the wires slightly touch

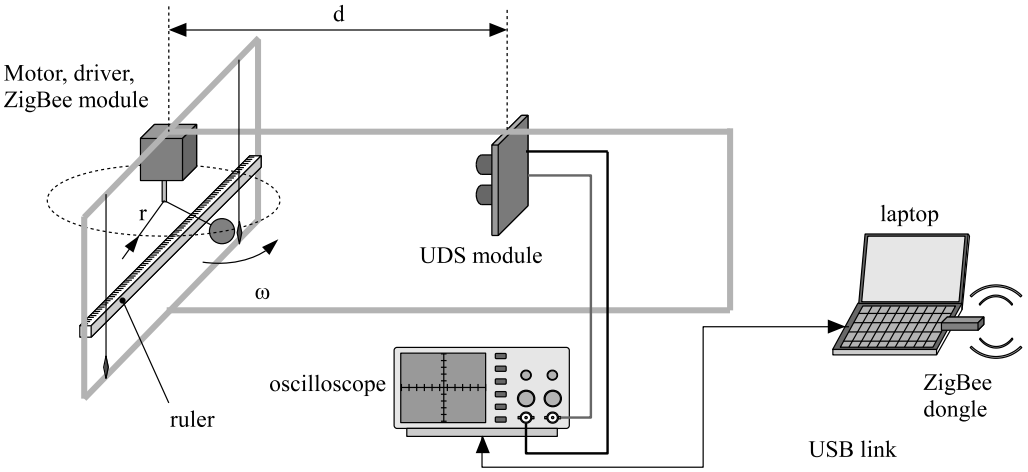

Figure 24: Sketch of the setup deployed for the characterisation of the build ultrasound Doppler system.

the rotating ball. The intersections between the ruler and two pendulums provide the factual diameter of the circular trajectory.

The operation nominal frequency of the ultrasound *Tx-Rx* system is nearly 40 kHz. A LeCroy HRO64Zi DSO has been used to acquire *Tx* and *Rx* signals, at a sampling rate up to 2 GS/s, with a 12 bits resolution. The *Rx* acquired signal is then processed by a Matlab-developed program that tunes some spectrogram parameters starting from the values of frequency and time resolution chosen by the user. Spectrograms are obtained by applying a STFT to the received signal, adopting the following parameters, all expressed in samples unit: (i) number of samples where STFT is applied, called n_f; length of the window to be used in each segment processing, called n_w; overlap length between two consecutive windows, called n_{ol}. The program processes the resulting spectrogram through the Hough algorithm, with the aim to estimate the trajectory of the reference target.

Several experiments have been performed to achieved the following goals: (i) reconstruct the rotating sphere trajectory and compare it with the theoretical μ-D signature; (ii) tune the parameters of the Hough algorithm (described in Section 2.4.3) to minimise the trajectory estimation errors; (iii) evaluate and characterise the performance of the UDS, in terms of speed estimation error over a wide set of data.

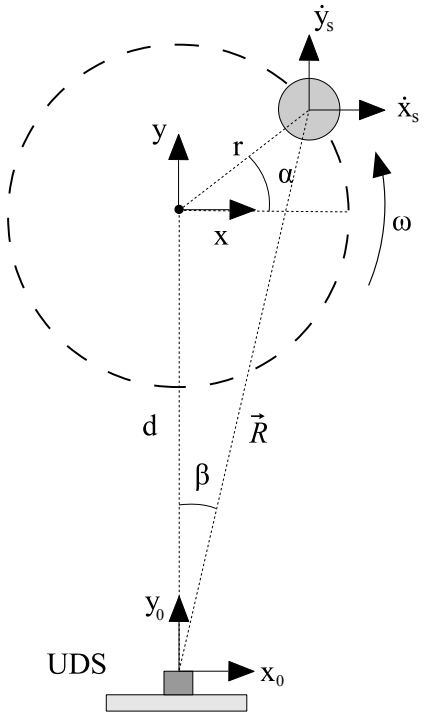

Figure 25: Plant of the UDS characterisation system.

3.2.1 *Theoretical micro-Doppler signature*

In order to evaluate the measurement system performance, a comparison between the theoretical trajectory and the obtained measures has been carried out. In Figure 25, a plant view of the experimental setup is shown. According to the micro-Doppler concepts introduced in Section 2.2, the μ-D signature caused by the target motion is due to the radial velocity v_r between the UDS and the sphere. In particular, if $\vec{v}_s$ is the vector representing the sphere speed and $\vec{u}$ is the LOS unity vector, v_r can be computed projecting $\vec{v}_s$ along $\vec{u}$. As shown in Figure 25, $\vec{v}_s = [\dot{x}_s, \dot{y}_s]$ and the range vector can be expressed as $\vec{R} = [r\cos\alpha, d + r\sin\alpha]$, with respect to the x_0-y_0 reference system located on the UDS device. The unity LOS vector $\vec{u}$ can be computed in function of $\vec{R}$, as $\vec{u} = \vec{R}/|\vec{R}|$. Furthermore, considering that $\alpha = \omega t + \alpha_0$ with α_0 denoting the initial phase, the μ-D signature in term of frequency shift $f_{\mu-D}$ can be computed as:

$$\begin{aligned} f_{\mu-D}(t) &= -2\frac{f_c}{c}\, v_r(t) = -2\frac{f_c}{c}\ <\vec{v}_s \cdot \vec{u}>, \\ &= -2\frac{f_c}{c}\ \frac{dr\omega\cos(\omega t + \alpha_0)}{\sqrt{d^2 + r^2 + 2dr\sin(\omega t + \alpha_0)}}, \end{aligned} \tag{16}$$

where f_c is the UDS transmitting frequency, c is the propagation speed of ultrasounds in air medium, $\vec{v}_s = [-r\omega \sin(\omega t + \alpha_0), r\omega \cos(\omega t + \alpha_0)]$ and $< \cdot >$ represents the dot product algebraic operation.

The agreement between the theoretical and experimental micro-Doppler signatures has been verified with a single example, in the case: $\omega = 15.71\,\text{rad/s}$ (150 rpm), $l_w = 0.233$ m. After a warm-up time allowing the sphere to reach a stable rotation, the UDS Rx signal has been acquired by the DSO at a sampling frequency F_s equal to 500 kS/S, for an acquisition time of 1 s. r has been experimentally measured through the alignment system, resulting in $r = 0.232$ m. Hence, the theoretical signature has been computed through Eq. (16). The acquired signal has been processed through the STFT according to the following parameters: $n_f = n_w = 16384$, and $n_{ol} = 14000$. As displayed in Figure 26a, the obtained spectrogram shows an horizontal dark straight line at a frequency f_c, i.e. the Tx carrier frequency, that constitutes the signal component due to stationary clutters. Superimposed, a tilted sine wave can be noticed, representing the sphere μ-D signature. The comparison between the experimental and the theoretical results is shown in Figure 26b, in which the original spectrogram of Figure 26a has been scaled to report speed along the y-axis ($\frac{c}{2f_c}$ scaling factor)[1]. The comparison demonstrates a perfect match between the theoretical speed and the measured μ-D signature. It can be noticed that the shape, frequency, and amplitude of the measured signal are the same as the theoretical trajectories ones.

The spectrogram of Figure 26a has been processed through the Hough algorithm to estimate the sphere speed. The result reported in Figure 26c shows that the measured curve does not fit perfectly the sine reconstructed by Hough transform. This is due to the model used in Hough transform. As previously described, the algorithm tries to find out a sine wave. The measured signal is indeed a pseudo-sine wave, lightly tilted on the right. However, the period of the reconstructed signal is the same as the measured signal, as well as the mean value and the amplitude. The latter one is equal to the sphere tangential speed $v_{s,t}$, easily computed as $v_{s,t} = \omega \cdot r$.

1 The initial phase α_0 has been manually varied to align the theoretical signature to the experimental one.

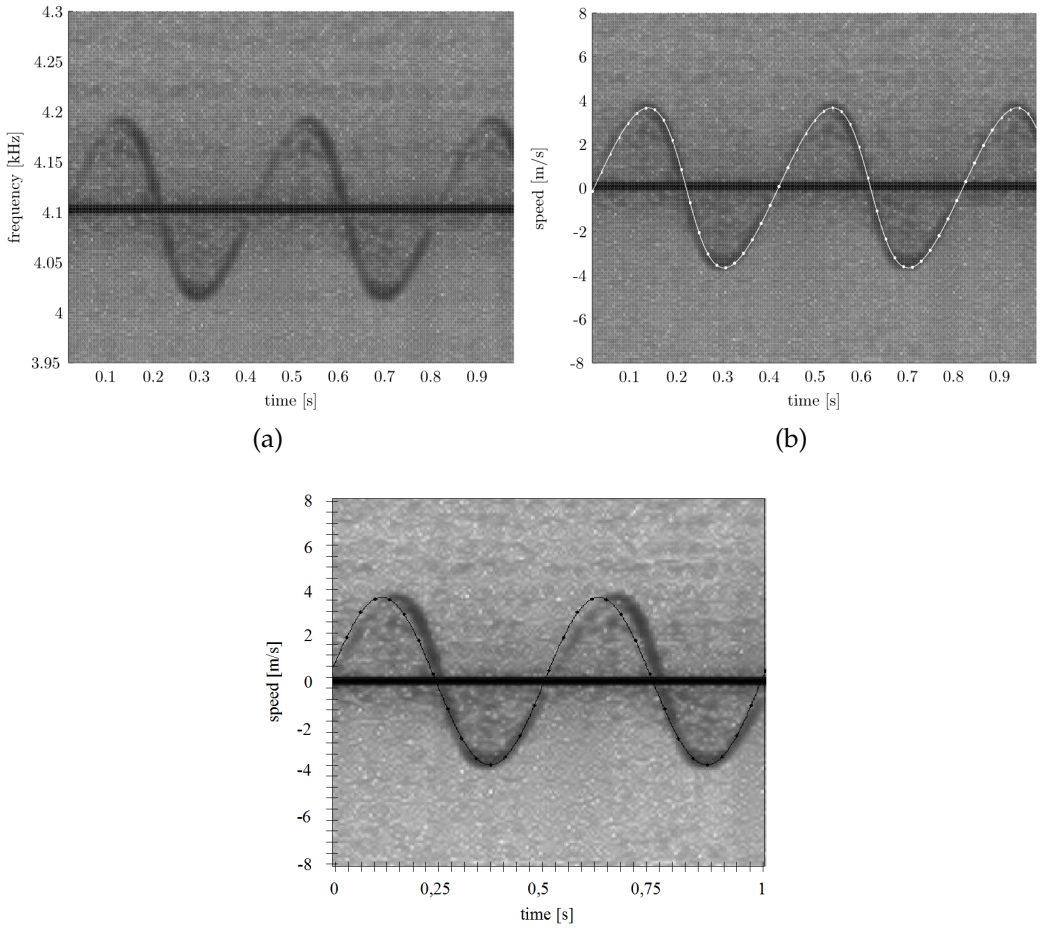

(a) (b)

(c)

Figure 26: (a) spectrogram representation of the μ-D signature induced by the rotating sphere; (b) comparison between the theoretical (white trace) and experimental signatures, in which the y-axis has been scaled to report speed; (iii) sine wave estimated through the Hough algorithm (black dotted trace).

3.2.2 *Tuning of the Hough transform parameters*

A number of 5 trials have been carried out with the aim of tuning the Hough transform parameters. The algorithm described in Section 2.4.3 is applied to the spectrogram representation of the rotating sphere $\mu - D$ signatures, in order to reconstruct the displayed sine waves, e.g. the one shown in Figure 26a. The employed Hough algorithm requires the definition of three key parameters: (i) d_y, the discretisation of the y-axis for the estimation of the sine wave mean value, y_0; (ii) dA, the discretisation of the sine wave amplitude, A; (iii) $d\varphi$, the discretisation of the sine wave

Table 3: Target rotation speed, wire's length and measured radius of the analysed circular trajectories.

Trial	l_w [m]	ω [rpm]	r [m]
1	0.153	150	0.150
2	0.153	200	0.155
3	0.233	150	0.232
4	0.233	200	0.236
5	0.328	150	0.331

initial phase, φ. As the Hough algorithm operates on images, d_y and dA are expressed in pixels, while $d\varphi$ is expressed in rad/s.

The setup adopted for the trials has been varied according to different choices of l_w and ω, as shown in Table 3. The received signals have been acquired through the DSO, with $F_s = 500$ kS/S, for an acquisition time of 1 s. For the spectrogram generation, the STFT has been applied with the following setup: $n_f = 16384$, $n_w = 16384$, $n_{ol} = 14000$ samples. This configuration yields a frequency resolution equal to 30.5 Hz and a corresponding time resolution equal to 0.033 s. Such a frequency resolution corresponds to a speed resolution nearly equal to 0.13 m/s, computed using the Doppler equation. The setup time and speed resolutions allow a proper measurement of the sphere trajectory, considering the minimum tangential target speed and the maximum rotation frequency as worst cases, and respectively equal to: (i) $v_{s,t}^{min} = \omega_{min} \cdot r_{min} = 2.35\,\mathrm{m/s}$ (trial 1); (ii) $f_{max} = \omega_{max}/2\pi = 3.33$ Hz (trials 2 and 4).

The achieved spectrograms have been subsequently processed by the Hough transform upon the variation of dy, dA, and $d\varphi$, considering two performance indexes: the estimation error of y_0 and A; the processing time. The Hough algorithm has been processed by a Matlab-developed program, running on a laptop with the subsequent features: Intel® Core™ i7-3520 @ 2.90 GHz CPU, 6 GB RAM, Windows 7 64-bit operating system.

Analysis of dy influence

Firstly, the effects of the d_y variation have been measured on the y_0 estimates. The outcomes of the analysis are the mean estimation error and the processing times, evaluated for each spectrogram obtained from the test trials. The reference value is $y_{0,r} = 151$ pixels. A set of 13 equispaced

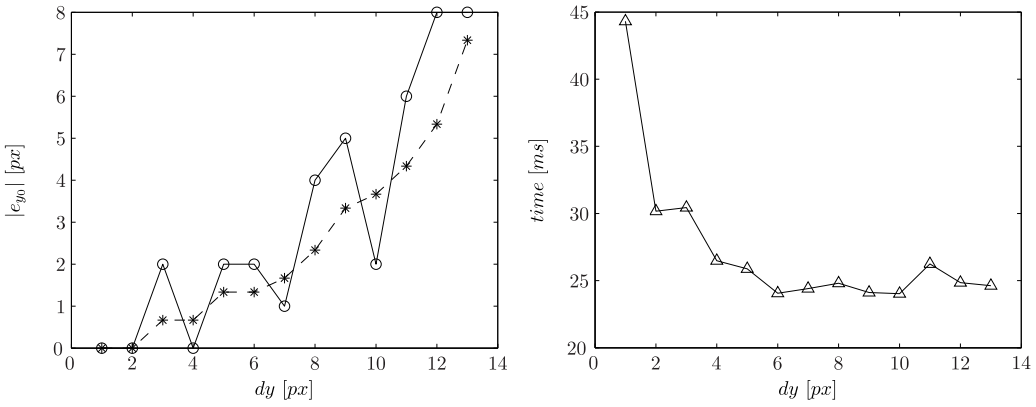

(a) (b)

Figure 27: Results of dy influence on the sine wave baseline value estimation: (a) absolute value of y_0 estimation error in solid line, three samples moving averaged version in dashed line; (b) algorithm processing time.

values for dy has been chosen, in the interval [1, 13] pixels. In order to merge the results, an arithmetical mean has been performed among the outcomes of each spectrogram processing. The results are displayed in Figure 27. In particular, Figure 27a shows that the mean of the absolute errors $|e_{y0}|$ increases as the quantisation dy increases. However, $|e_{y0}|$ does not show a monotonic behaviour. A three samples moving average is shown as well, in a dashed line with asterisk markers. Such average shows the increasing trend of $|e_{y0}|$. The oscillating component is due to the fact that, certain values of dy are integer sub multiples of the value to estimate, hence the accumulator space contains the exact value of y_0. Hence, even with a poor quantisation of the y-axis, the y_0 estimate may be even accurate. For this reason, the algorithm could become unreliable over a certain value of dy. For a reliable estimation of y_0, a maximum value for dy has been chosen as, $dy \leq 9$ [px].

In Figure 27b the processing time is reported. It varies from 45 to 24 ms.

Analysis of dA and $d\varphi$ influence

In this sub-paragraph, the effects of d_A and $d\varphi$ variation are measured on the A estimation. The analysis outcomes are the standard deviation of A estimation error, $\sigma(e_A)$, and the processing time. They have been evaluated upon the variation of dA in the interval [1, 20] pixels (step 1 pixel), and $d\varphi$ in the interval $[2\pi/200, 2\pi/10]$ rad (step $2\pi/200$ rad). The

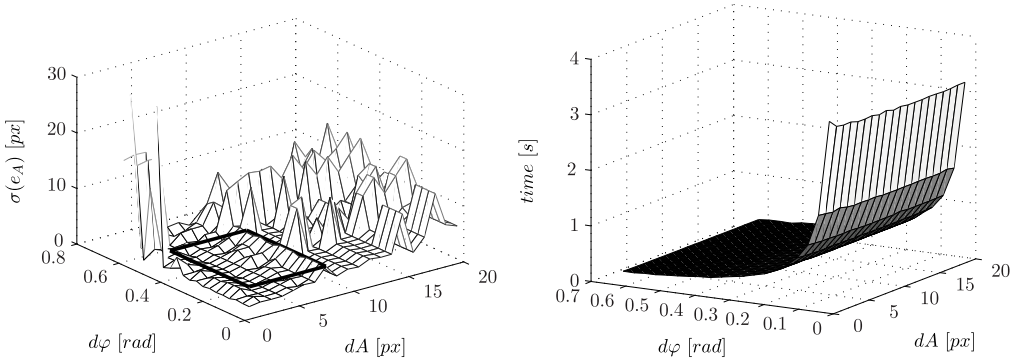

Figure 28: Results of dA and $d\varphi$ influence on the sine wave amplitude estimation: (a) variance of A estimation error, and identified rectangular working area; (b) required processing time.

reference values of A have been computed by estimating $v_{s,t}$ from the reference target setup data, shown in Table 3, and mapping the resulting tangential speed into pixels unit.

In Figure 28, the analysis results are shown. In Figure 28a, the $\sigma(e_A)$ behaviour displays an area, highlighted by a rectangle, where the estimations are reliable. The rectangle corners are {1 px, $2\pi/200$ rad} and {8 px, $13 \cdot 2\pi/200$ rad}. Within this area, $\sigma(e_A)$ is lower than 5 pixels. For increasing values of dA, $\sigma(e_A)$ shows an increasing trend with an oscillating component superimposed. Again, this is due to the fact that some particular values of dA are sub multiples of the amplitude value to measure, hence it is possible to have a small measurement error even though the quantisation is rough.

The processing time of this algorithm stage is shown in Figure 28b. It can be noticed a strong dependency of the computation time with the $d\varphi$ parameter. dA is instead not responsible of large processing time variations. This is a predictable outcome since only the $d\varphi$ parameter influences the number of iteration loops of the algorithm. A lighter effect can be imputed to the parameter dA. Indeed, as small is dA, as finer is the quantization. This cause an increasing of the matrix $m(A, \varphi)$ size, and the final operation of maximum score searching requires an increasing time.

The identified area provides a Hough parameters range that permits to estimate a sine wave in a spectrogram with the following specification: (i) measurement error of the baseline value lower than 0.225 m/s; (ii) measurement error of the amplitude lower than 0.225 m/s; (iii) maximum processing time of 1 s.

3.2.3 *Estimation of the speed measurement errors*

The UDS system has been finally characterised in terms of tangential speed estimation error, performed on a large dataset. Referring to the measurement system displayed in Figure 24, the following setup has been adopted:

- a 10 mm radius wooden sphere has been used as reference target;
- $d = 0.84$ m;
- $l_w = 0.335$ m;
- ω has been varied from 100 rpm to 300 rpm with a 20 rpm step;
- r is measured using the alignment system for each setup of ω.

The signal from the UDS has been picked up after a warm-up time useful to allow the sphere reaching a stable rotation. A total number of 110 measurements have been collected, 10 for every rotation speed setup. The DSO has been set to acquire 1 MS. In particular, a $F_s = 500$ kS/s sampling frequency has been chosen for an acquisition time equal to 2 s.

The spectrograms of the collected data have been obtained by applying the STFT using the following parameters: $n_f = 16384$, $n_w = 16384$, $n_{ol} = 14000$ samples. This configuration yields a frequency resolution, Δf, equal to $F_s/n_f = 30.5$ Hz. Each spectrogram is processed by the Hough transform algorithm. The results reported in Section 3.2.2 have allowed to choose an optimised set of the Hough parameters. In particular, the following setup has been chosen: $dy = 2$ [px], $dA = 2$ [px], $d\varphi = 2\pi/200$ [rad].

The Hough transform output is an estimation of the sine wave amplitude in pixel unit, $\hat{A}$. Such a value is relative to the micro-Doppler signature of the rotating sphere; in particular, it represents the target tangential speed. $\hat{A}$ is then mapped into m/s unit, according to the spectrogram frequency resolution and the Doppler equation. In details, the estimated tangential speed $\hat{v}_{s,t}$ can be computed as:

$$\hat{v}_{s,t} = \frac{\hat{A}\Delta f \cdot c}{2f_c}.$$

The f_c value is computed for each acquisition taking the maximum value of the Rx signal spectrum, while $c = 343$ m/s at a 20°C ambient temperature. $\hat{v}_{s,t}$ is then compared to the reference value $v_{s,t}$, simply computed according to the setup parameters, as $v_{s,t} = \omega r$.

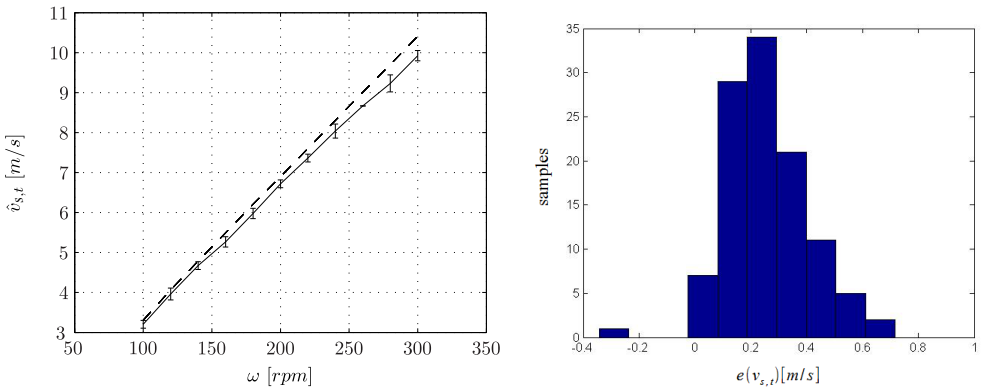

(a) (b)

Figure 29: (a) comparison between $v_{s,t}$ (dashed line) and $\hat{v}_{s,t}$ (solid line); (b) histogram of $v_{s,t}$ measurement error.

In Figure 29a, the behaviours of $v_{s,t}$ and $\hat{v}_{s,t}$ are displayed in a dashed and solid line respectively. For each value of ω, the mean value $m(\hat{v}_{b,t})$ and the standard deviation $\sigma(\hat{v}_{b,t})$ have been computed, from the 10 $\hat{v}_{b,t}$ measured samples. The values of $m(\hat{v}_{b,t})$ are displayed with the associated confidence interval, considered equal to $2\sigma(\hat{v}_{b,t})$. From Figure 29a, it can be noticed that $\hat{v}_{b,t}$ is not well aligned with $v_{b,t}$. In particular, an offset-gain error is highlighted. The offset error can be due to the entire measurement chain, as superposition of the ultrasound system, the acquisition system and the image processing algorithm impairments or errors. The gain error can be also imputed to the mechanical structure, which has not been fixed at the ground. In fact, for ω greater than 200 rpm, the rotating sphere induces a non-negligible vibration on the structure. This causes a slight stick-slip phenomena between the ground and the structure, and a slight bending of beam holding the motor.

In Figure 29b, the histogram of the tangential speed measurement error $e(v_{s,t})$ is shown. A nearly normal distribution can be noticed. The mean error is nearly equal to 0.25 m/s while the error standard deviation is approximately equal to 0.15 m/s.

3.3 HUMAN GAIT SIGNATURES ACQUISITION

A first set of acquisitions has been performed in order to familiarise with the setup and find out an optimal measurement configuration. Two different approaches have been adopted. Firstly, a number of human gait signatures have been acquired using a single UDS, according to differ-

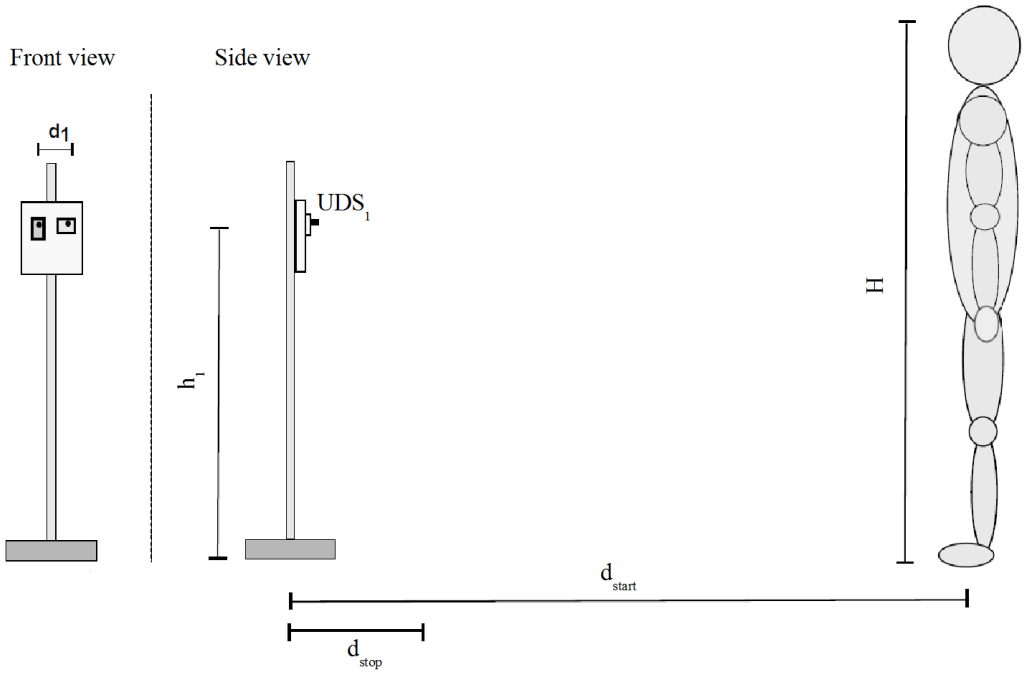

Figure 30: Measurement setup for the preliminary acquisition of human gait signatures, employing one UDS module.

ent gait styles of the test target. In this case, the transmitter and receiver boards of the UDS device have been placed very close one with the other, yielding a quasi mono-static configuration of the ultrasound radar. In a second experiment, two UDS devices have been deployed. This allows to employ two mono-static ultrasound radars for the micro-Doppler signature acquisition, focusing in two different part of the human target. In alternative, a two multi-static radars configuration can be deployed, if the cross-coupling between the two UDSs is considered.

3.3.1 *Single-UDS measurements*

In Figure 30, the adopted measurement setup is shown. A single ultrasound system UDS_1 has been deployed to acquire the μ-D signature of a walking human target. The Rx and Tx boards have been fixed to a wooden board, at a reciprocal distance d_1 equal to 5 cm. UDS_1 has been clamped to an aluminium pole at a height $h_1 = 1$ m, with respect to the floor. The UDS_1 transmitter, Tx_1 has been set in *continuous wave* mode, emitting at frequency f_c nearly equal to 40.5 kHz.

The human under test is 1.72 m tall (H), and has been asked to walk toward the ultrasound device according to 3 different styles: (i) normal

gait; (ii) slow gait; (iii) normal gait exaggerating the limbs motion. The start and stop distance of the trial have been set respectively equal to $d_{start} = 4\,\text{m}$ and $d_{stop} = 0.5\,\text{m}$.

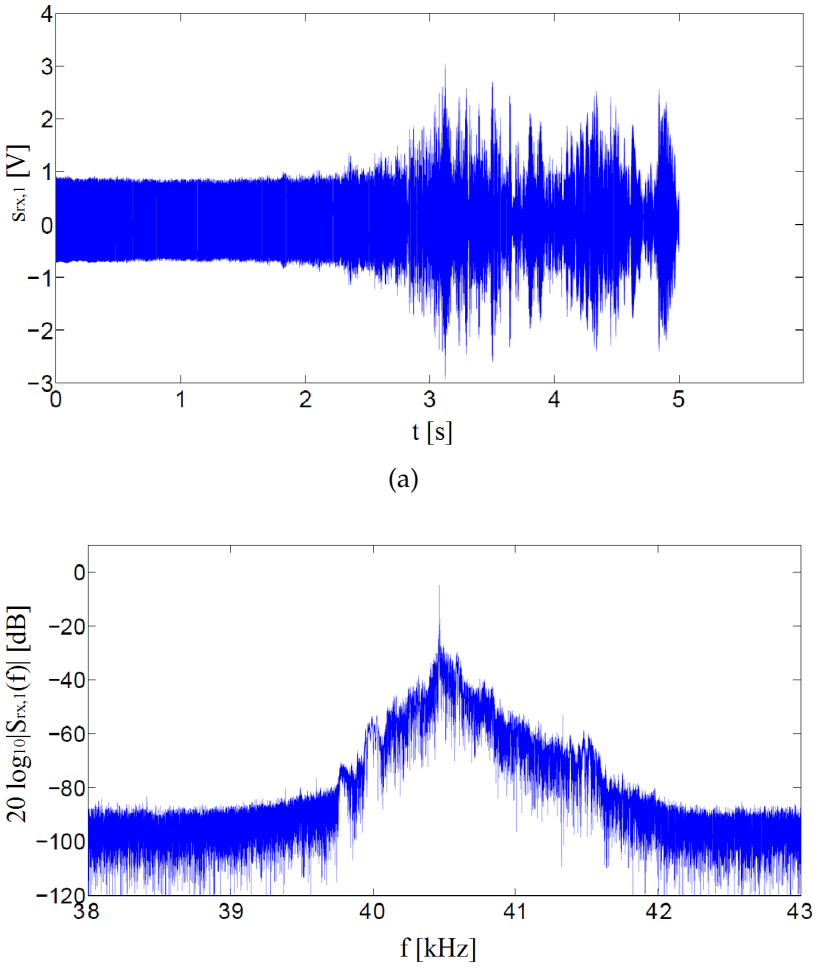

Figure 31: Example of signal acquired through the UDS employing the setup of Figure 30: (a) $s_{Rx,1}(t)$ in time domain; (b) spectrum of $s_{Rx,1}(t)$.

The ultrasound received signal $s_{Rx,1}(t)$ has been acquired by using the DSO, setting a sampling frequency of 500 kS/s. A 5 s acquisition time has been chosen, allowing the person under test to cover the whole walking path. In Figure 31a and 31b, an example for the $s_{Rx,1}(t)$ signal is shown, respectively in time and frequency domains. From the first plot, a steady signal can be noticed till $t \approx 2.3$ s, hence the signal starts oscillating. During the first phase, the target is still and only the stationary clutters contribute on the $s_{Rx,1}(t)$ signal. In a second phase, the target starts walking and the signal amplitude increases as the person approaches the stop distance. In Figure 31b, the signal spectrum $S_{Rx,1}(f)$ is shown, reported

in dB scale. A strong contribution can be identified in correspondence of f_c, due to the stationary clutters. Sidebands can be noticed around the main carrier frequency. Such shifts are induced by the target movement according to the Doppler effect phenomenon. The sideband width is approximately equal to 2.8 kHz.

$s_{Rx,1}(t)$ has been then processed through the STFT, setting a time window duration of 0.15 s and a 90% overlap among segments. In Figure 32, the spectrogram representations of $s_{Rx,1}(t)$ is reported, for each analysed gait style. In particular, Figure 32a displays the spectrogram relative to the normal gait, from which a number of considerations can be drawn:

- the black trace corresponding to a frequency equal to f_c represents the Tx_1 carrier, and it is due to the still objects surrounding the environment (0 Doppler components).
- The superimposed and merged sinusoidal-like traces represent the micro-Doppler signature of the walking human under test. The darker the traces the greater the received signals. Furthermore, traces that are external with respect to f_c are characterised by higher frequency shifts, and hence greater speeds.
- The external traces can be associated to the feet, legs and arms motion, as they constitute the fastest body parts during the gait.
- The trace that can be distinguished in the middle of the signature can be imputed to the thorax motion. The intensity of such a component is greater with respect to the other ones. In fact, the thorax has the largest surface with respect to the other body parts, and hence it causes stronger backscatter.
- The signature intensity tends to increase as the person gets closer to the UDS_1 device.

In Figure 32b, the spectrogram associated to the slow gait style is shown. A lower frequency shift can be noticed, as well as a greater periodicity of the traces. Indeed, a slower gait causes a longer steps repetition time, and a lower limbs speed. Finally, Figure 32c displays the spectrogram relative to a normal gait, but with an exaggerated motion of arms and legs. The traces have got nearly the same periodicity of the ones displayed in Figure 32a. However, the augmented limbs motion provokes an higher frequency shift, due to greater motion speeds.

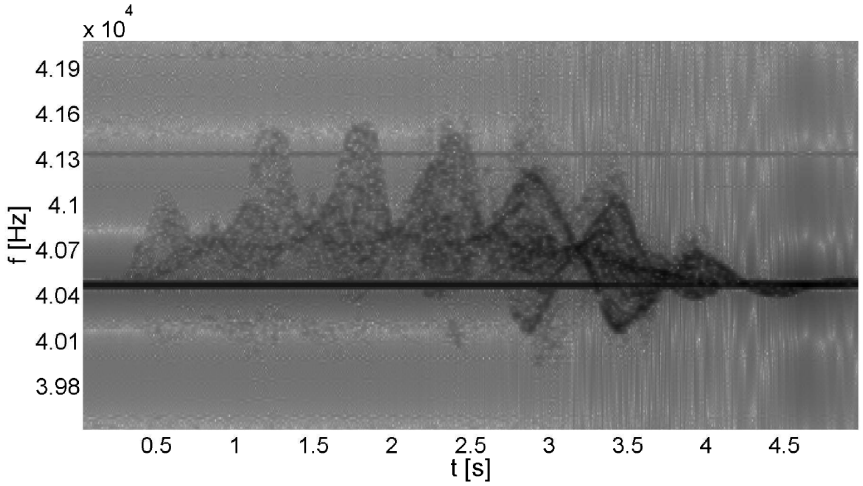

(a)

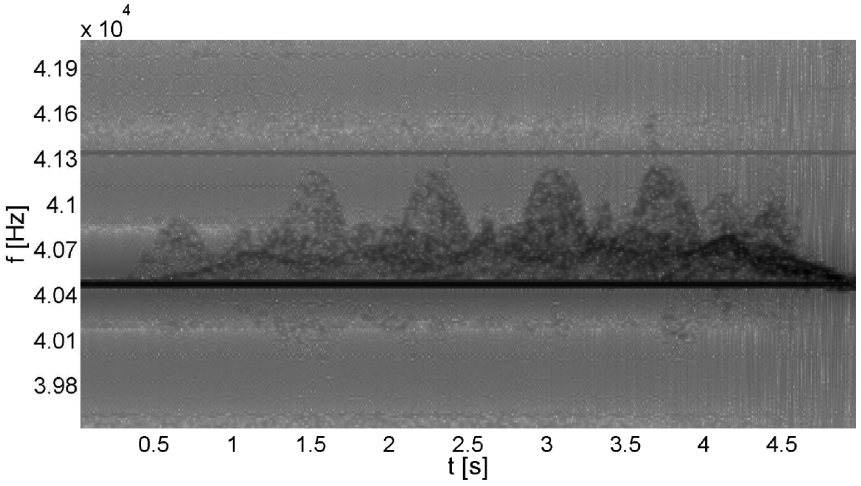

(b)

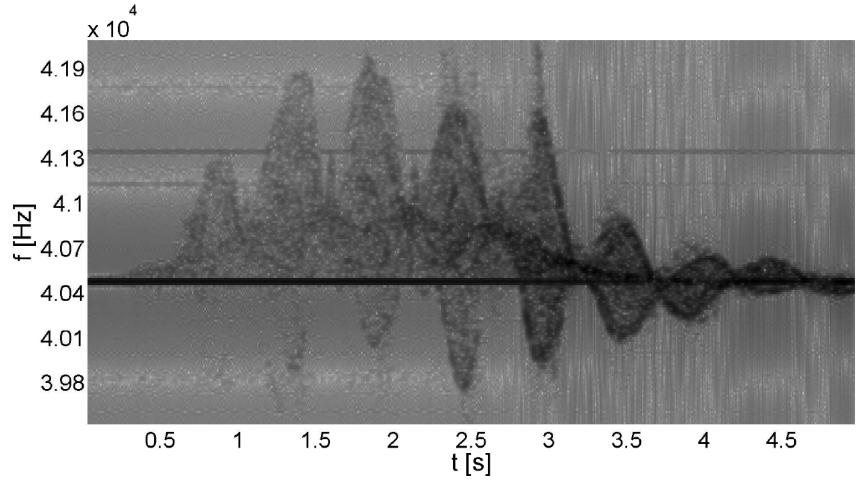

(c)

Figure 32: Spectrogram representations of the human μ-D signatures: (a) normal gait; (b) slow gait; (c) normal gait exaggerating the limbs movements.

3.3.2 *Two-UDSs measurements*

In a second measurement setup, as displayed in Figure 33, two ultrasound systems have been deployed at the same time. UDS_1 and UDS_2 have been clamped to the supporting pole at two different heights, respectively $h_1 = 0.95$ m and $h_2 = 0.1$ m. The ultrasound devices have been set to work at two different carrier frequencies, $f_{c,1} = 43$ kHz and $f_{c,2} = 37$ kHz. The difference between $f_{c,1}$ and $f_{c,2}$ has been chosen in compliance with the Doppler frequency bandwidth estimated during the previous experiments.

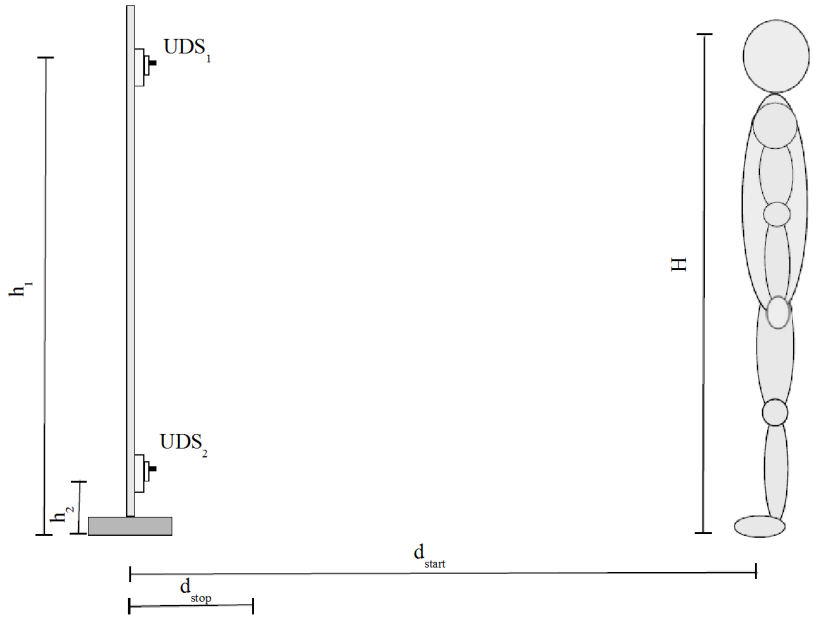

Figure 33: Measurement setup for the preliminary acquisition of human gait signatures, employing two UDS modules.

The same test person has been asked to walk normally, starting from a $d_{start} = 3.5$ m and stopping at $d_{stop} = 0.5$ m. The received signals $s_{Rx,1}(t)$ and $s_{Rx,2}(t)$ have been acquired and processed according to the same setup previously deployed. In Figure 34, portions of the obtained spectrograms are displayed, relative to the signals received by both Rx_1 and Rx_2. In particular, Figure 34a shows the $s_{Rx,1}(t)$ spectrogram representation. Two frequency components can be shown, corresponding to the employed transmitting frequencies. The signature of the walking target at 43 kHz is due to the Tx_1 transmission, and it shows a strong trace due to the thorax motion, while the signal coming from the limbs is much weaker. The contribution at 37 kHz is due to Tx_2. In this case, the limbs

traces are more visible, while the thorax trajectory is less evident. These results can be explained focusing on the setup geometry, as shown in Figure 33. The UDS_1 is directed toward the human chest, while UDS_2 illuminates mainly the lower parts of the body. Hence, the receiver of UDS_1 (Rx_1) collects the backscatters mainly coming from the upper body parts, i.e. the power of the signal components coming from the lower body parts is weaker. On the contrary, Rx_2 receives a stronger signal relatively to the backscatters from the lower body parts and vice versa.

In Figure 34b, the spectrogram obtained through the processing of $s_{Rx,2}(t)$ is shown. It contains the contributions of both Tx_1 and Tx_2. In this case, the signature at $f_{c,2}$ permits the clear distinction of the legs traces. At the time $t = 2.4$ s, some noisy traces can be highlighted, probably associated to the floor-feet friction. The thorax trace is instead almost invisible. This is due to the location of Tx_2. At a distance of 0.1 m from the ground, Tx_2 only partially illuminates the upper part of the body. Moreover, according to the setup geometry shown in Figure 33, the signal backscattered by the thorax can hardly return to UDS_2. The signature due to the transmission of Tx_1 is displayed on the upper part of Figure 34b. The signal associated to the thorax is visible, while the legs contribution is almost absent. The reason can be again explained by geometric considerations related to the measurement setup.

The employment of more than one ultrasound device can be useful whether a focused measurement has to be performed. In the specific test case, the deployed UDS_1 and UDS_2 allow to focus respectively on the thorax and feet movements.

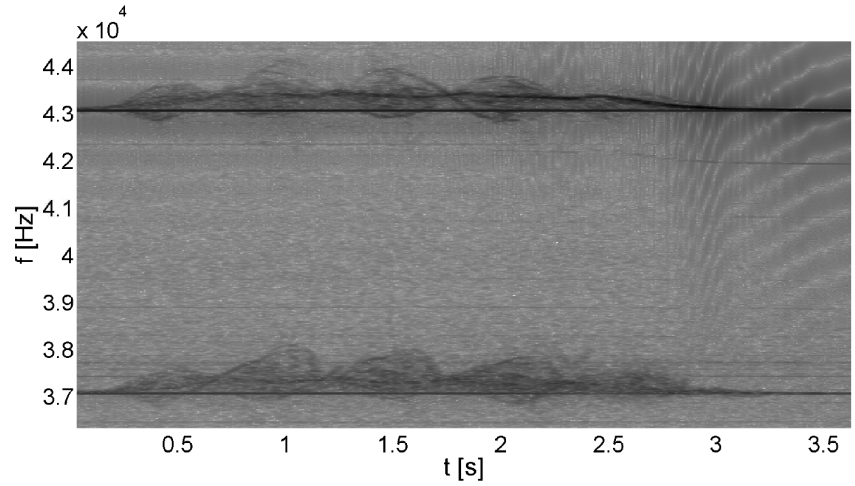

(a)

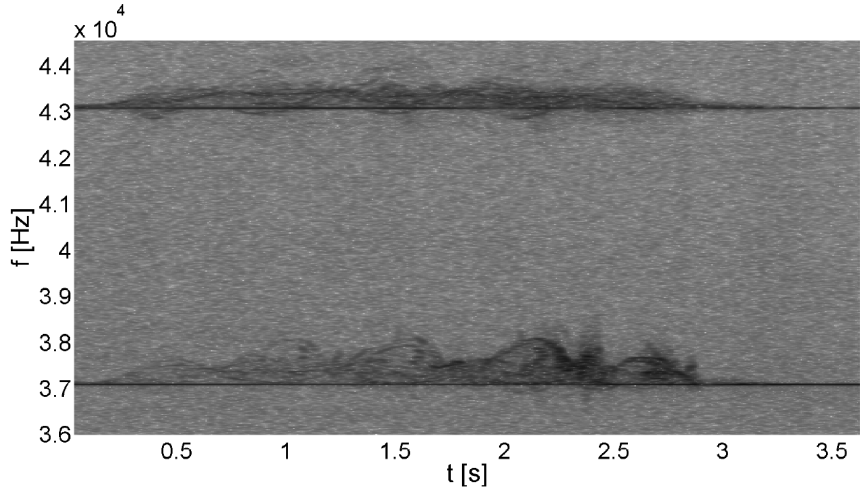

(b)

Figure 34: Spectrogram representations of the human μ-D signatures obtained with the two UDS modules setup: (a) spectrogram of $s_{Rx,1}(t)$; (b) spectrogram of $s_{Rx,2}(t)$.

4

ULTRASOUND AND CAMERAS-BASED SYSTEMS COMPARISON

In this chapter, the ultrasound Doppler system previously designed has been characterised by using a very accurate cameras-based system. The modularity and lightweight characteristic of the designed UDS have allowed the deployment of the measurement system at the *Bioengineering of the Movement Laboratory*, at the Information Engineering Dept. of the University of Padova. It is equipped with a motion capture system, composed of six infrared cameras and two force plates embedded under the floor. Basically, the target to analyse is suitably prepared by attaching a set of reflecting markers, that can be detected by the cameras-based system. While the target performs the defined movements, the motion capture system can detect the displacement trajectories of the markers, with an accuracy of 1 mm.

Hence, the achieved trajectories have been exploited as a reference for the characterisation of the UDS. In particular, several experiments have been carried out, by analysing both simple and complex movements of a human test target. The purpose is to highlight how every single body part contributes on the ultrasound micro-Doppler signature. Moreover, the estimation of some body parts trajectories is investigated, in the case of simple movements.

4.1 MOTION CAPTURE SYSTEM DESCRIPTION

A picture of the laboratory is shown in Figure 35. It is equipped with a motion capture system, composed of six infrared cameras and two force plates embedded under the floor. This cameras-based system is indirect, not-invasive and based on the application of reflecting markers on anatomic points of the human body. The cameras track the markers displacements during the performed movement, and the measurement system is then capable to reconstruct the body segments and their movements. The acquisition system can capture frames up to a 120 frame/s frequency. The accuracy of the markers position measurement is lower than 1 mm; moreover, the markers speed can be measured with a 0.01

Figure 35: Equipments of the *Bioengineering of the Movement Laboratory*. The four frontal cameras are circled as well as the force plates. Besides, the detail of the camera is shown.

m/s accuracy. Further technical details about the equipments and the software modules employed can be found in Section 4.1.1. The fine measurement capabilities of the motion capture system has been deployed as a reference for the validation of the developed ultrasound Doppler system.

A number of trials has been performed both using the UDS and the motion capture system at the same time. Different movements of the human test target have been analysed, and the trajectories estimated by the cameras-based system have been superimposed to the images (spectrograms) obtained from the UDS signals. The human under test has been suitably prepared. He has been asked to wear only shorts, and a set of reflecting markers has been then fixed by using an adhesive material. The protocol for the markers placing is shown in Figure 36a, while Figure 36b displays the test subject with the applied markers. Among the placed markers, the main ones are here enlisted. In particular, the markers located on the inferior body part are:

- RASIS/LASIS, right/left anterior superior iliac spine;
- RGT/LGT, right/left greater trochanter;
- RLE/LLE, right/left lateral epicondyle of the femur;
- RME/LME, right/left medial epicondyle of the femur;
- RLM/LLM, right/left lateral malleolus;
- RMM/LMM, right/left medial malleolus;

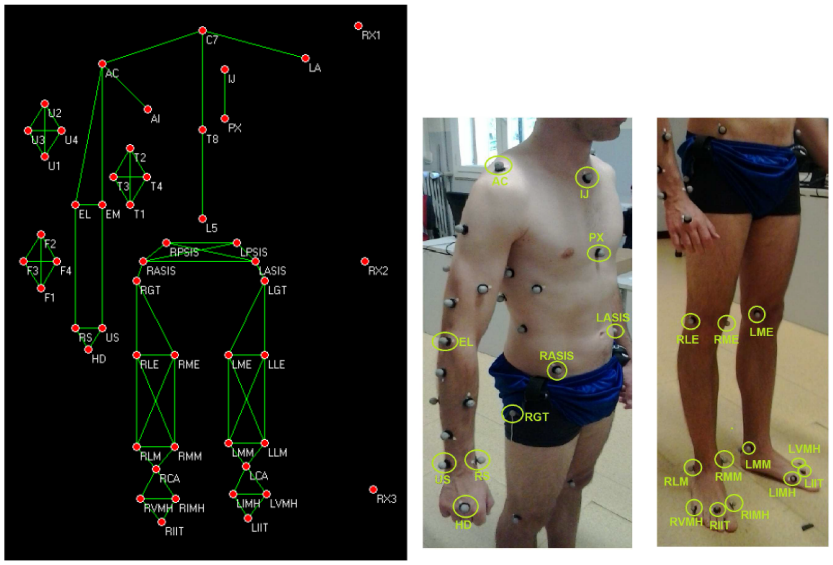

(a) (b)

Figure 36: Location of the reflecting markers: (a) employed protocol; (b) picture of the test human target.

- RVMH/LVMH, right/left fifth metatarsal distal head;
- RIMH/LIMH, right/left first metatarsal distal head;
- RIIT/LIIT, right/left proximal phalanx of the second digit.

While, for the superior body part, the main considered markers are:

- AC, right acromion;
- EL, right lateral epicondyle of the humerus;
- RS, right radial styloid process;
- US, right ulnar styloid process;
- HD, right distal head of the third metacarpus;
- IJ, suprasternal notch;
- PX, xiphoid process.

The chosen markers set has been deployed for all the experimental measurements reported in this chapter.

The processing system adopted by the laboratory acquires all the images from the cameras, during the whole trial. Subsequently, a *tracking* operation is performed at the post-processing stage, by using the *SMART*

Tracker software tool (described in Section 4.1.1). Every acquired frame must be reviewed to check the correctness of the marker automatic assignment, according to the adopted protocol. Finally, a second software (*SMART Analyser*) is deployed to filter and smooth the markers trajectories. In Figure 37, a frame obtained after the software tool processing is shown. The reference system 0 represents the absolute reference, which is employed by the motion capture system as origin for expressing all the estimated trajectories. As displayed on the right part of the picture, the three circled markers represent the positions of the employed ultrasound Doppler systems, placed in front of the test target. In this way, the range vector between a generic marker and a UDS can be easily computed as difference between the marker and UDS coordinates.

The designed ultrasound system allows to obtain images of a moving target, and it is influenced by the radial velocity of the target components. Hence, in order to compare the outputs of the two systems, the trajectories measured by using the motion capture system have to be further processed, as enlisted:

1. the displacement trajectories are translated into the UDS reference system. This operation only required the knowledge of the UDS position, expressed with respect to the reference system 0.

2. A time derivative operation is performed to obtain the velocity trajectories of the analysed markers. Subsequently, a moving average filter is applied to smooth the curves.

3. The speed vector of a generic marker is projected along the UDS-marker range vector (line of sight) to compute the radial velocity with respect to the ultrasound device (see Section 2.2.1). The range vector is computed from the knowledge of the UDS and the marker positions in the absolute reference system.

At end of the processing stage, the marker-UDS radial velocity trajectories can be directly superimposed to the spectrograms achieved by acquiring and processing the ultrasound signals. Such a comparison can be exploited to cross-check the traces of the obtained spectrogram, and/or to achieve speed estimations from the ultrasound signal (with an error evaluation).

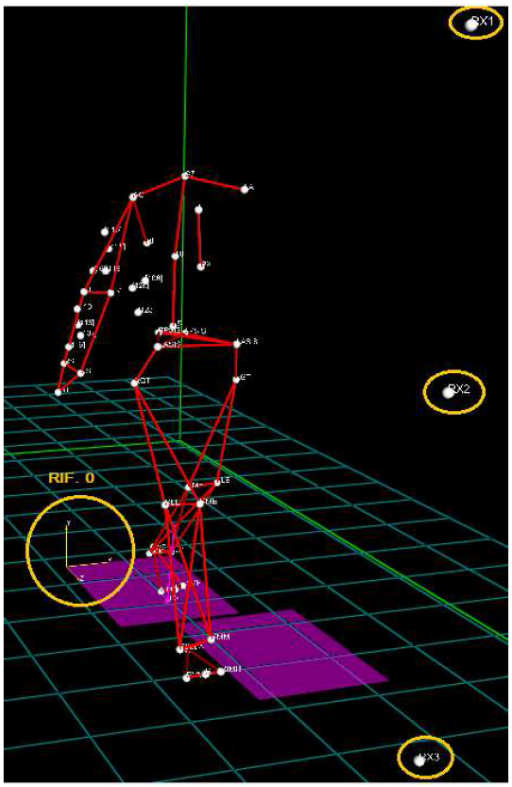

Figure 37: Screenshot of the SMART Tracker software employed to check the markers assignment.

4.1.1 *Equipments and tools details*

The measurements have been carried out at the *Bioengineering of the Movement Laboratory* of the University of Padova. The deployed stereophotogrammetry SMART System, produced by BST, enlists the following equipments and tools:

- a set of passive reflecting (in the infrared wavelength) markers.
- Six digital Charge-Coupled-Device (CCD) videocameras, equipped with infrared optical filters. They can acquire frames at a 60/120 Hz frequency.
- Six infrared illumination device, characterised by high power and digital control of the emission level. Each illumination device is mounted on each camera, and emits luminous pulses of 250 μs duration to avoid interferences due to solar and environmental light.
- A set of 3.5 mm lenses and two 6-12 mm zoom lenses. The focus and diaphragm can be manually adjusted.

- Two digital M-HUB as power supplier and synchronisation system for the cameras and illumination devices. Each M-HUB can handle three cameras, providing the timing of the luminous pulses and the camera shutter control.
- Cables to connect the HUBs to the cameras, illumination devices, and a workstation.
- Workstation: is a personal computer equipped with an analog-to-digital PCI acquisition board and two frame-grabber PCI boards. The boards are connected to the HUBs to gather timing information and acquire the captured frames.
- Software suite:
  - *SMART Capture*: allows to calibrate the cameras system, acquire dynamic and kinematic data, display the markers position in real time.
  - *SMART Tracker*: performs the three-dimensional reconstruction of the markers trajectory from the acquired frames information. Each marker is labelled and tracked for all the acquisition time. It is also possible to analyse the force vectors measured by the force plates.
  - *SMART Analyser*: allows to perform a biomechanical analysis of the kinematic and dynamic data, visualise the markers trajectories, and export the data in several formats.
- two force plates, manufactured by Bertec Corporation, FP4060-10 model. Each plate exploits four load cells (based on strain gages), mounted at the plate corners. The embedded electronic circuitry amplifies, filters and digitalises the load cells signals, which are then forwarded to the HUBs.

4.2 ANALYSIS OF BASIC MOVEMENTS

A first analysis has been performed by considering a simple movement. A sketch of the measurement setup in shown in Figure 38. The test target has been prepared as shown in Figure 36b, and has been asked to extend and contract the right arm. The movement starts from an extended arm position and terminates as the hand is close to the shoulder. The target has been asked to move so that to limit the hand motion along the x_1 and

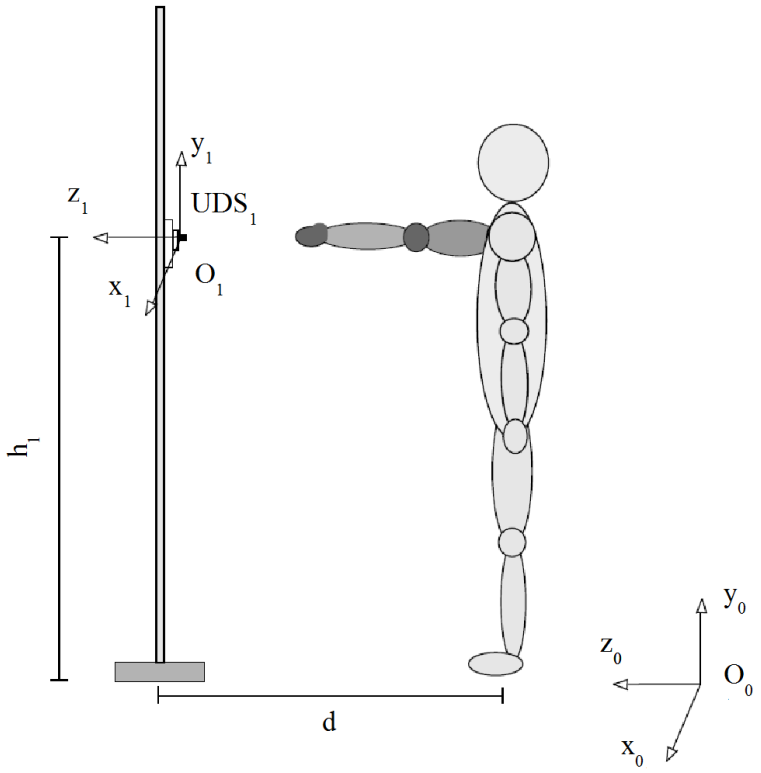

Figure 38: Measurement setup for the hand motion tracking.

y_1 axes. In this way, the hand trajectory will be mainly directed along the z_1 axis. Referring to the setup shown in Figure 38, the UDS has been placed at a height $h_1 = 1.43$ m from the ground, nearly at the same target's shoulder height. The horizontal distance d between the target and the UDS has been set equal to 1 m. The tern x_0-y_0-z_0 represents the absolute reference system of the motion capture system.

A number of 10 acquisitions has been carried out, each one 15 s long, deploying at the same time the UDS and the cameras-based system. Only for a single measure, the entire set of markers has been tracked, but limited to the right arm. In details, the following markers have been tracked: AC, EL, RS, US, HD. The measured trajectories have been expressed in the x_1-y_1-z_1 reference system, and then the speed trajectories have been derived as described in Section 4.1. In Figure 39, some of the trajectories measured by the motion capture system are shown. In Figure 39a, 39b and 39c, the displacement trajectories of the considered markers are plotted. The translations along x_1 and y_1 of the markers HD, RS and US (near the hand) are limited with respect to the ones along the z_1 axis, as expected from the chosen setup conditions. This is valid even for the speed trajectories, as shown Figure 39d, 39e and 39f. The HD, RS and US

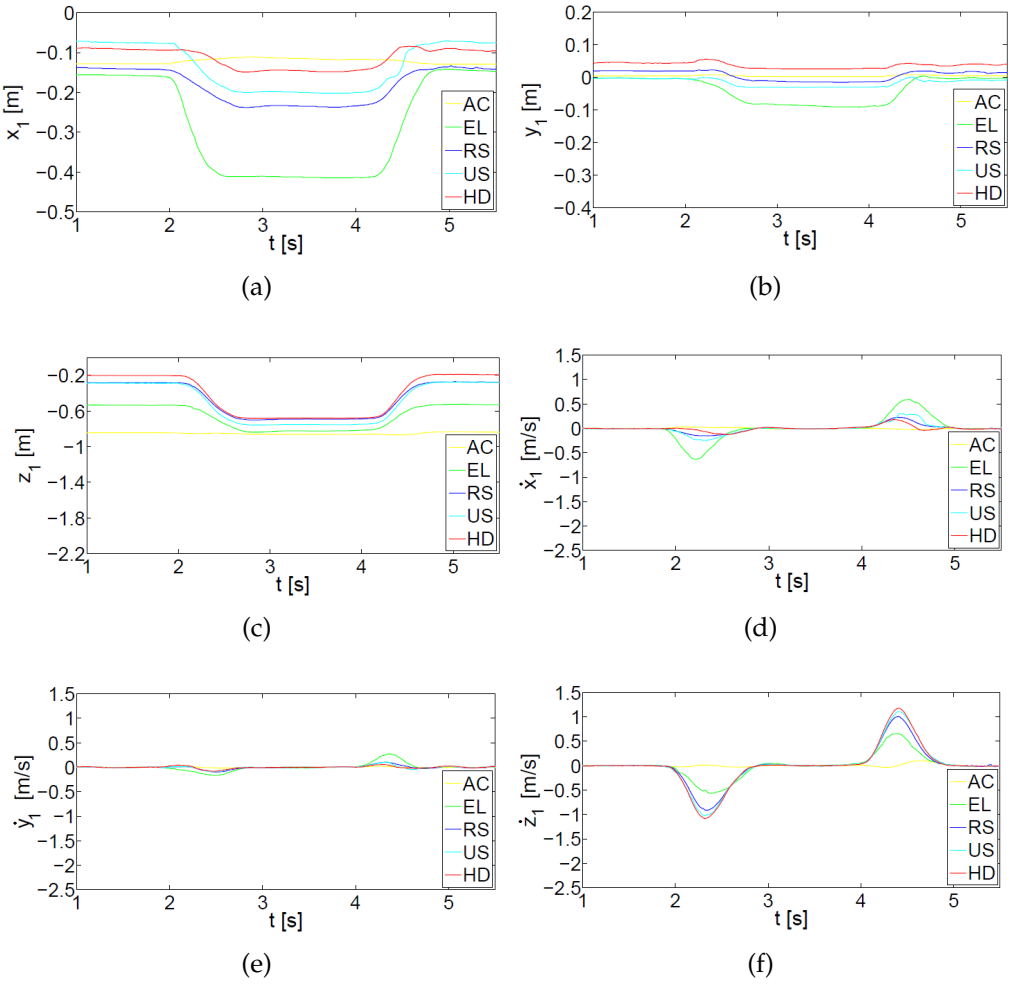

Figure 39: Measured trajectories of the enlisted markers: (a) position trajectories along x_1 axis; (b) position trajectories along y_1 axis; (c) position trajectories along z_1 axis; (d) velocity trajectories along x_1 axis; (e) velocity trajectories along y_1 axis; (f) velocity trajectories along z_1 axis.

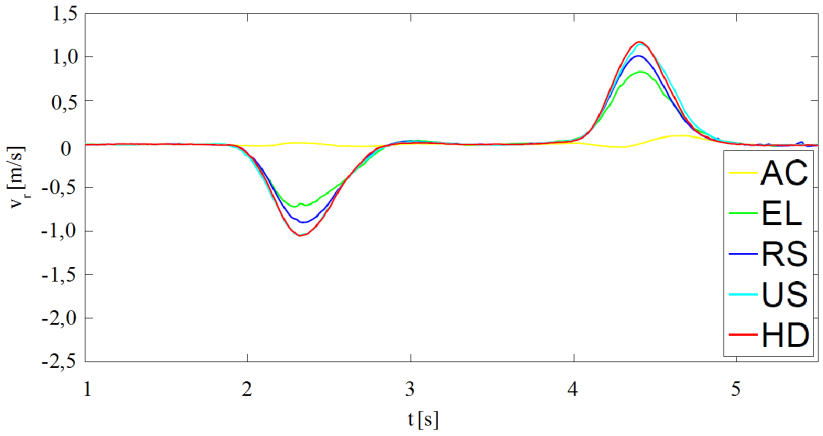

(a)

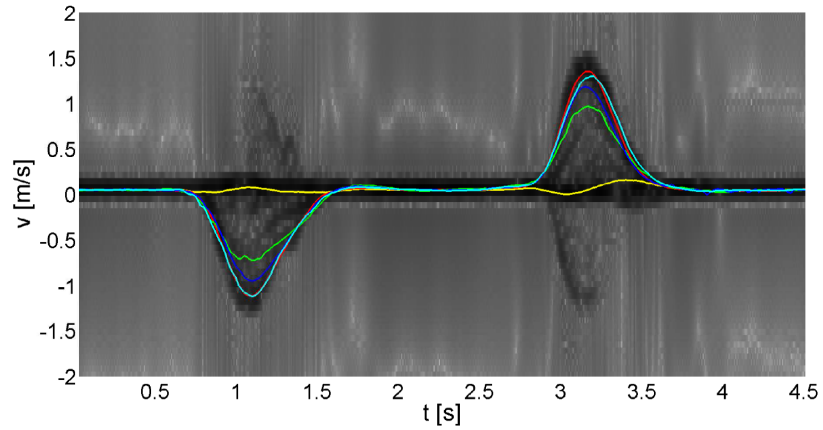

(b)

Figure 40: (a) Radial velocity trajectories of the considered markers; (b) comparison with the spectrogram obtained through the ultrasound system.

speed trajectories along x_1 and y_1 vary in the range ± 0.2 m/s, while the ones along the z_1 axis are comprised within [-1.2, 1.4] m/s.

Subsequently, the radial velocity (with respect to the UDS position) of each marker is computed, by projecting the speed components along the UDS-marker vector. This operation allows to directly compare the spectrogram obtained by the UDS signal with the speed trajectories achieved through the motion capture system. In Figure 40a, the computed radial velocity trajectories are shown. The latter ones appear very similar to the speed along the z_1 axis (Figure 39f). As expected, the measurement setup and the way the movement is performed cause the hand motion to be directed towards the UDS, and hence along the z_1 axis.

The received ultrasound signal has been digitised through a DSO, setting a sampling frequency of 500 kS/s. Then, it has been processed by

a STFT to achieve a spectrogram representation, choosing a 0.15 s long time window, and an overlap value equal to 90%.

In Figure 40b, the radial velocities displayed in Figure 40a have been superimposed to the achieved spectrogram. As reported in previous results, the spectrogram shows a set of merged trajectories, difficult to access singularly. The EL and US markers (near the wrist) trajectories show a similar trend, but they do not seem to contribute on the μ-D signature displayed in the spectrogram. This is reasonable since the wrist is not well illuminated by the UDS device, according to the adopted measurement setup. Moreover, the limited surface makes the wrist less visible, i.e. the backscatter is poor. The AC (shoulder) trajectory shows a slighter movement with respect to the other markers. In fact, during the movement, the test target extends and contracts the right arm, resulting in a limited shoulder motion. A good fit can be noticed between the HD (nearly the hand centre) and the darkest trace of the spectrogram. This is due to three reasons: (i) during the target movement, the hand is the closest body part with respect to the ultrasound sensor; (ii) the hand is well illuminated by the UDS device; (iii) it is also the fastest body part for the particular choice of the target movement.

In this case, where a particular body part motion can be highlighted and distinguished on the micro-Doppler signature, the speed trajectory can be easily estimated from the spectrogram.

4.2.1 *Hand speed trajectory estimation*

The HD trajectory is the most distinguishable component in the achieved spectrograms. Hence, an estimation of such a trajectory has been performed for all the collected micro-Doppler signatures. The comparison with the motion capture system results allows to characterise the UDS in terms of speed measurement error.

A suitable Matlab-developed algorithm has been applied to the spectrograms, performing the following sequence of operations:

1. transformation of the spectrogram, from a grayscale to a black and white image, as shown in Figure 41a. This requires a proper choice of a threshold level, experimentally chosen equal to 0.32.

2. Every column of the image is inspected to extract the lower and higher envelope of the displayed trajectory. The obtained envelopes

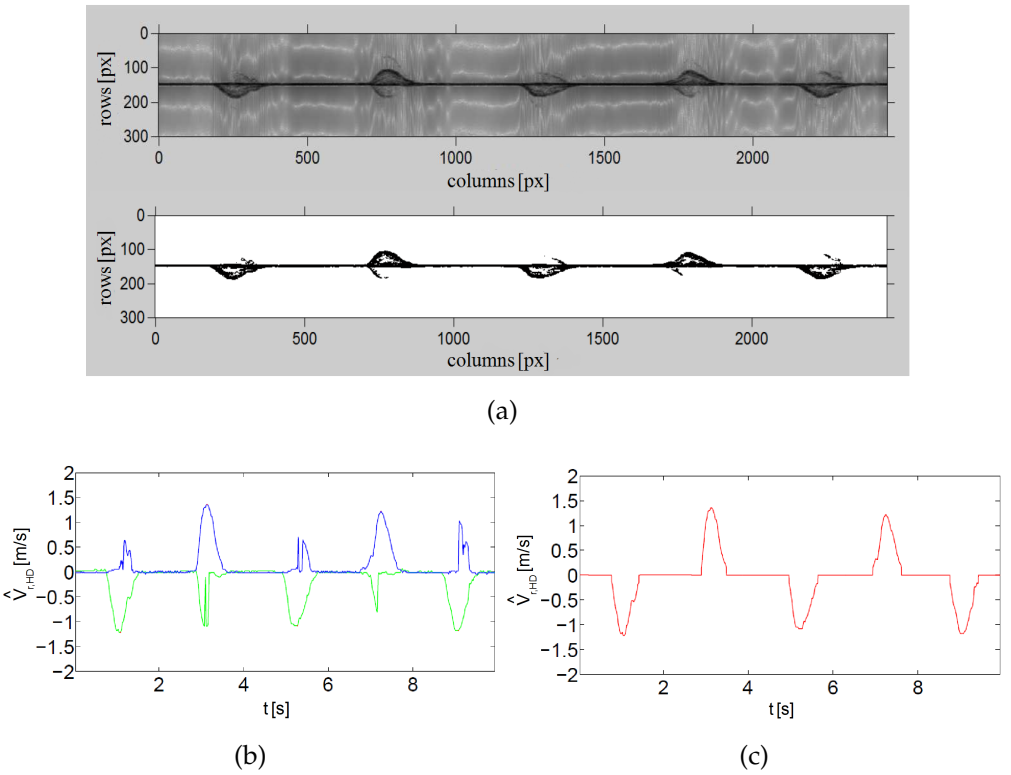

Figure 41: (a) Transformation of the obtained spectrogram into a binary image; (b) upper and lower envelopes estimated from the spectrogram; (c) estimation of the hand (HD) speed trajectory.

are displayed in Figure 41b, where the x and y axes have been rescaled to report time and speed respectively.

3. The upper and the lower enveloped are compared and combined to obtain the final estimated trajectory $\hat{v}_{r,HD}(t)$, as shown in Figure 41c.

In Figure 42, a comparison is shown among the spectrogram, the estimated $\hat{v}_{r,HD}(t)$ (white trace) and $v_{r,HD}(t)$ (red trace), which represents the speed trajectory of HD as measured by the motion capture system. A good agreement can be noticed between $\hat{v}_{r,HD}(t)$ and $v_{r,HD}(t)$.

The measurement error of each trial has been estimated as: $e_{v,HD}(t) = \hat{v}_{r,HD}(t) - v_{r,HD}(t)$. The mean value m_e and standard deviation σ_e of $e_{v,HD}(t)$ have been then computed for each trial, as shown in Table 4. By concatenating all the trials, a mean error equal to -0.014 m/s has been computed along with a standard deviation equal to 0.09 m/s.

Finally, the histogram of $e_{v,HD}$ for all the trials has been obtained and displayed in Figure 43. It reports the normalised frequencies along the y-axis, and the normalised values of the measurement error along the x-

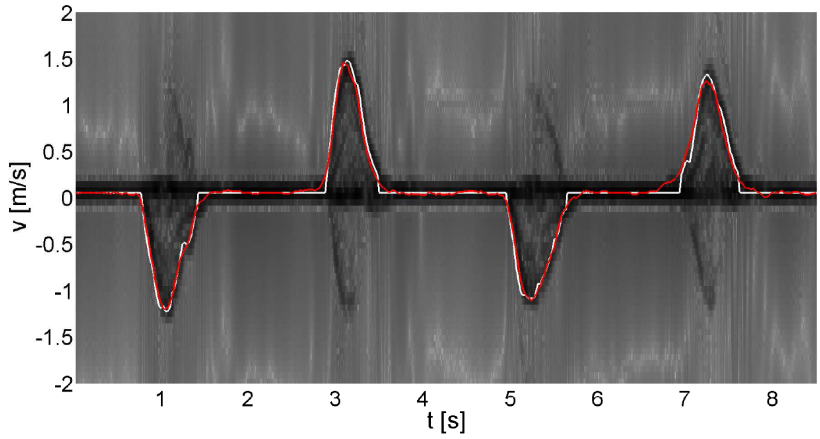

Figure 42: Superposition of the spectrogram, the reference $v_{r,HD}$ trajectory (red trace) and the estimated $\hat{v}_{r,HD}$ trajectory (white trace).

Table 4: Values of m_e and σ_e, relative to the hand speed measurement error, reported for each trial and overall.

trial	m_e [m/s]	σ_e [m/s]
1	0.00	0.09
2	-0.02	0.07
3	-0.01	0.06
4	-0.02	0.15
5	-0.02	0.08
6	-0.03	0.08
7	0.00	0.08
8	-0.01	0.07
9	-0.01	0.12
10	-0.01	0.09
TOT	-0.01	0.09

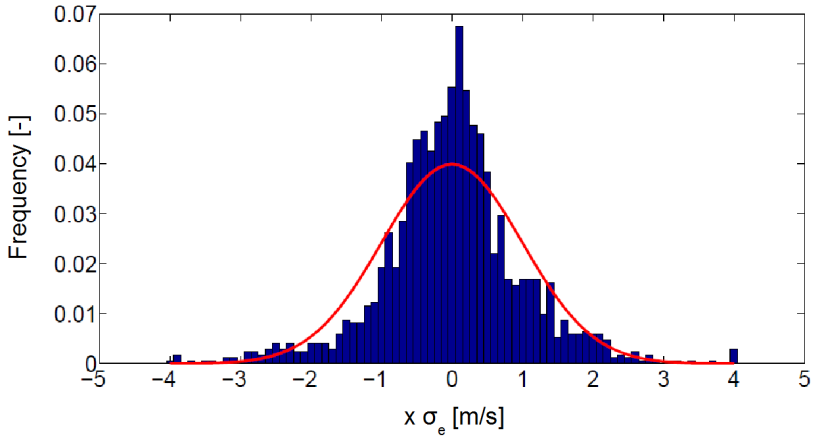

Figure 43: Histogram of the measurement errors $e_{v,HD}$.

axis. The values of $e_{v,HD}$ have been normalised by subtracting the mean value and then dividing for the standard deviation. The histogram well fits a Gaussian distribution.

4.3 GAIT ANALYSIS

The ultrasound Doppler system has been then tested to characterise the human gait. The obtained micro-Doppler signatures have been compared with the measures achieved through the motion capture system with the following aims: (i) highlight how every single body part contributes on the overall μ-D signature; (ii) evaluate the match quality between the spectrogram representation of the ultrasound signal and the trajectories measured by the cameras; (iii) evaluate eventual hidden body parts within the signature, or particularly visible contributions.

The employed measurement setup is shown in Figure 44. The UDS_1 device has been fixed at height $h_1 = 1\,m$ from the floor. The test target has been asked to walk normally, from a distance d_{start} to a distance d_{stop} with respect to UDS_1. d_{start} and d_{stop} have been chosen to allow the target performing 3/4 steps, and are respectively equal to 2.5 m and 0.5 m. A set of ten acquisitions has been performed; in every test, the target has walked toward the ultrasound device following a straight line.

The UDS_1 has been set to transmit a continuous sine wave at a 40.5 kHz frequency. The received signal has been collected through the DSO, according to a sampling frequency equal to 500 kS/s. Finally, the ultrasound signal has been processed by a STFT to achieve a spectrogram

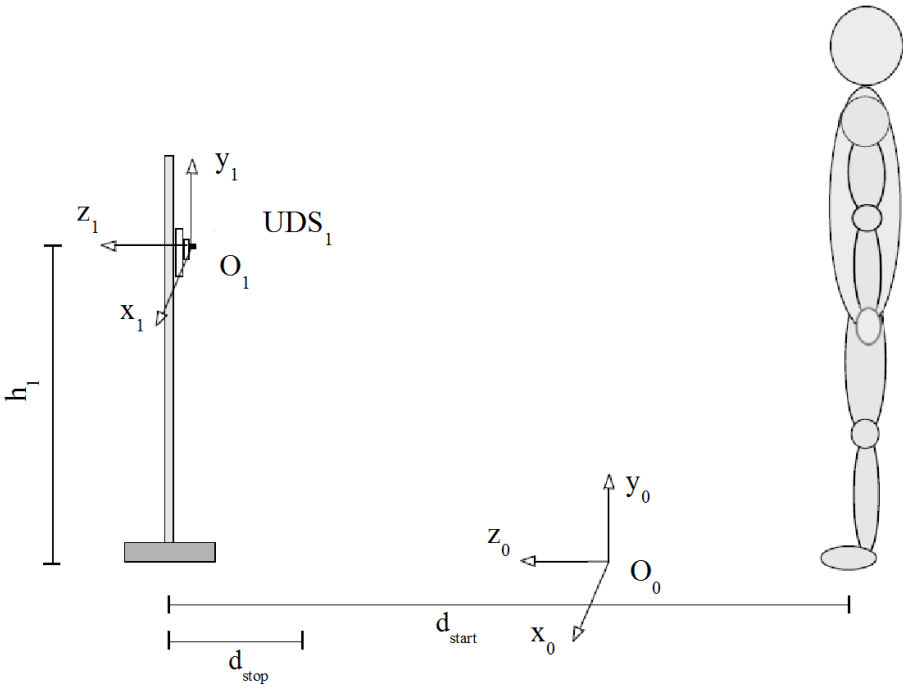

Figure 44: Measurement setup for the human gait signature analysis.

representation. For this analysis, the STFT has been applied by choosing a 0.15 s long time window, and an overlap value equal to 90%.

Simultaneously, the trajectories of target-attached markers have been acquired through the motion capture system. It provides, as outputs, the markers displacement trajectories, with respect to the reference system located in O_0 (Figure 44). Then, a change of coordinates has been applied to express the trajectories according to the UDS_1 reference system, i.e. x_1-y_1-z_1. In Figure 45 and 46, some of the displacement trajectories along the z_1 axis are reported, according to the reference system centred in O_1. All the displayed trajectories tend to a 0.5 m value, which represents the chosen stop distance. The trajectories associated to the limbs show a steps characteristic, typical of the gait motion. Instead, the trajectories of the markers close to the thorax show a smoother behaviour. The speed trajectories are then computed through a time derivative stage and a moving average filtering. Finally, the radial velocities with respect to the UDS_1 are computed. The obtained radial speed trajectories can be considered redundant. Indeed, the markers applied to the same articulation show an almost equal speed trajectory, e.g. the RLE and RME trajectories. Considering the purpose of this analysis, the speed trajectories of the same articulation have been combined by an arithmetic mean, obtaining a *virtual marker* that represents a single articulation. For exam-

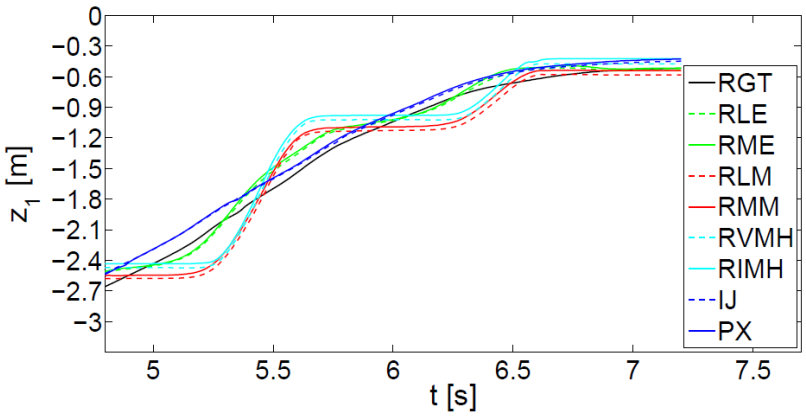

Figure 45: Displacement trajectories along z_1 of the enlisted markers.

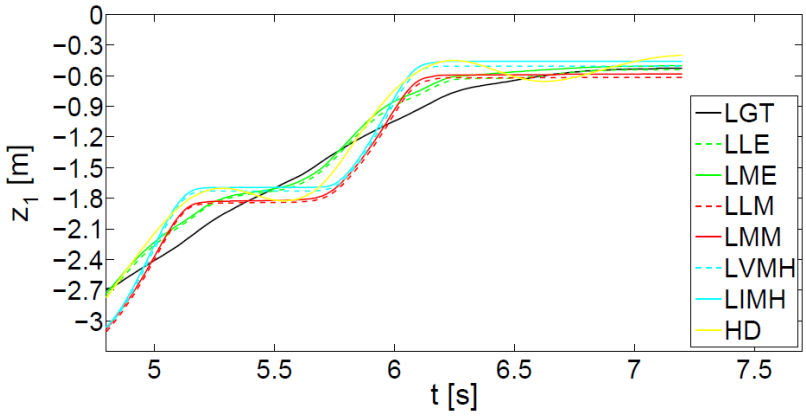

Figure 46: Displacement trajectories along z_1 of the enlisted markers.

ple, the RLE and RME trajectories have been merged to obtain the virtual right knee speed curve. Similarly, the following couples of markers have been merged: RLM/RMM, RVMH/RIMH, LLE/LME, LLM/LMM, LVMH/LIMH, IJ/PX. Hence, as displayed in Figure 47, a set of radial velocity trajectories is obtained, to be used as comparison with the spectrogram representation of the signal collected by UDS_1. A spectrogram is shown in Figure 48, relative to the same markers trajectories plotted so far. The displayed μ-D signature is characterise by a set of merged curves, very similar to the ones plotted in Figure 47. Some markers exhibit a good fit with the spectrogram traces. Figure 49 plots the IJ/PX mean trajectory superimposed to the spectrogram. The markers IJ and PX are located on the thorax; in fact, a good match can be noticed with the spectrogram darkest trace. This confirms the results of the simulation reported in Section 2.5.3, and it also agrees with the outcomes of some preliminary measurements reported in Section 3.3. As expected, the trace associated to the thorax is very distinguishable on the displayed spectrogram. In fact, the large thorax surface causes a strong ultrasound backscatter, that appears in a darker trace on the spectrogram.

Other body parts are less visible and discernible. In Figure 50, the mean RLE/RME (right knee) and LLE/LME (left knee) speeds are displayed and superimposed to the μ-D signature. They do not match any spectrogram traces. Knees are in fact body parts characterised by a small surface, and hence the associated spectrogram traces tend to be confused with other body parts trajectories, having larger surface but similar movement speeds. In Figure 51, the trajectory speed of the hand-attached marker (HD) is shown. A clear match with the corresponding spectrogram trace can be noticed. Moreover, during the backward movement, the hand speed trajectory assumes negative values.

Finally, Figure 52 displays most of the marker trajectories, bundled and superimposed to the ultrasound micro-Doppler signature. As the target maintains a steady gait speed (till $t = 4.5$ s), the feet are the body parts characterised by a greater velocity. While the human target slows down to stop at the defined distance, the feet speed dramatically reduces, while the hands become the fastest parts, due to inertially effects. Moreover, in Figure 52, a spectrogram trace without an associated marker trajectory can be noticed. It is located in the time interval $5 < t < 5.5$ s, on the positive part of the y axis. Such a trace is probably due to the left hand movement, where no markers are present. Indeed, according to the em-

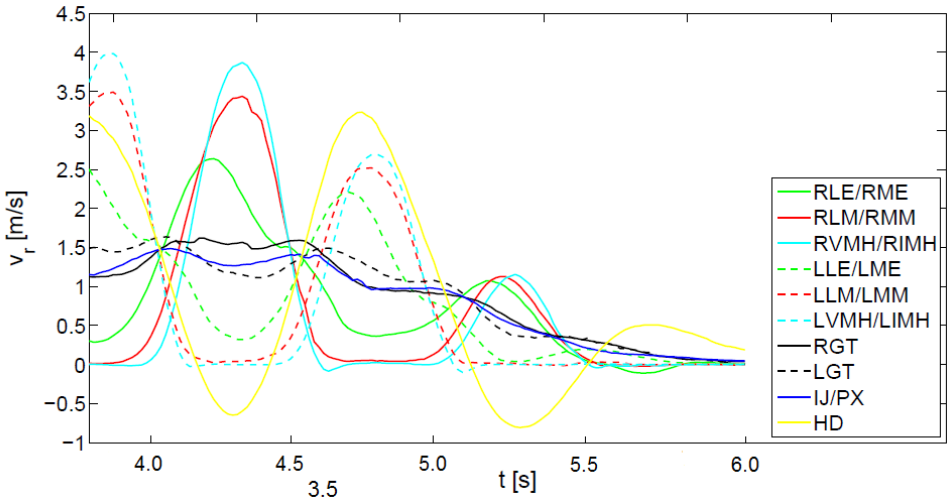

Figure 47: Radial velocities of markers RGT, LGT, HD and mean radial velocities of RLE/RME, RLM/RMM, RVMH/RIMH, LLE/LME, LLM/LMM, LVMH/LIMH.

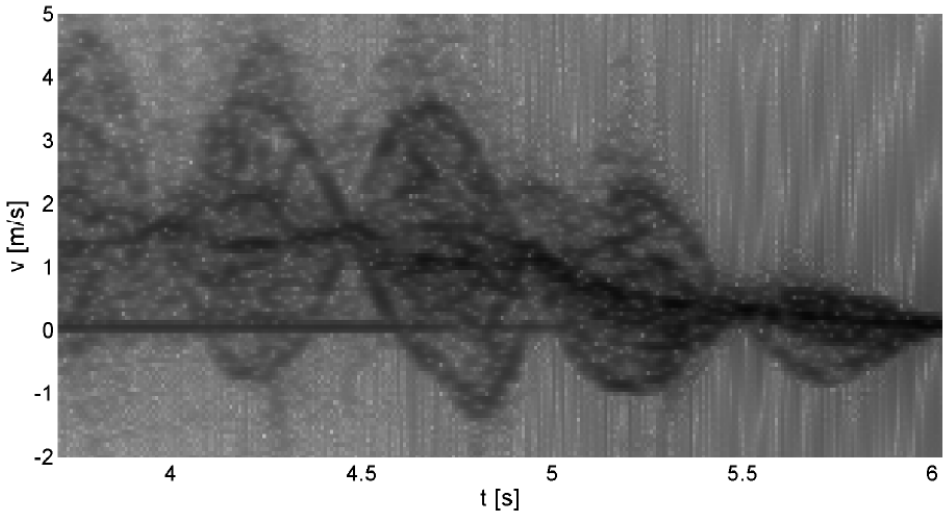

Figure 48: Part of spectrogram obtained after the processing of the ultrasound signal received by the UDS_1 device.

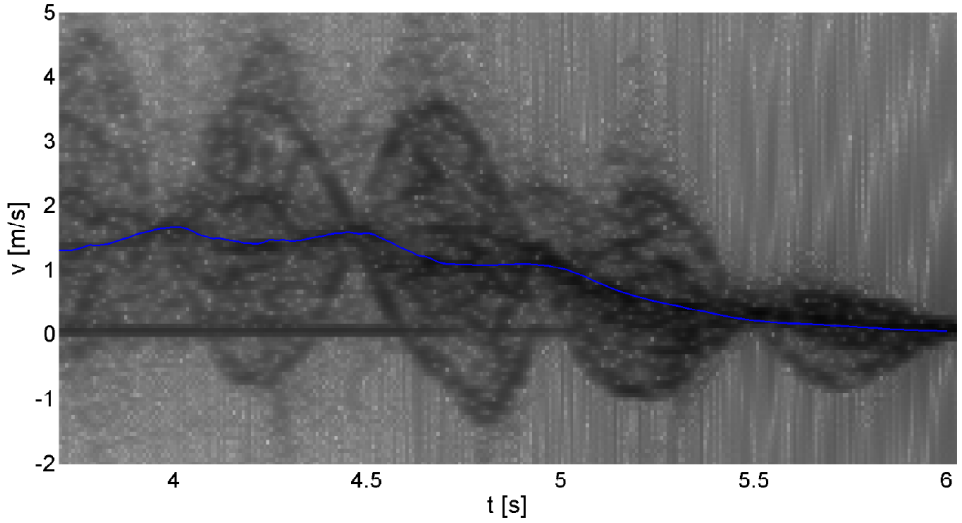

Figure 49: Mean IP/PX radial velocity trajectory superimposed to the achieved spectrogram.

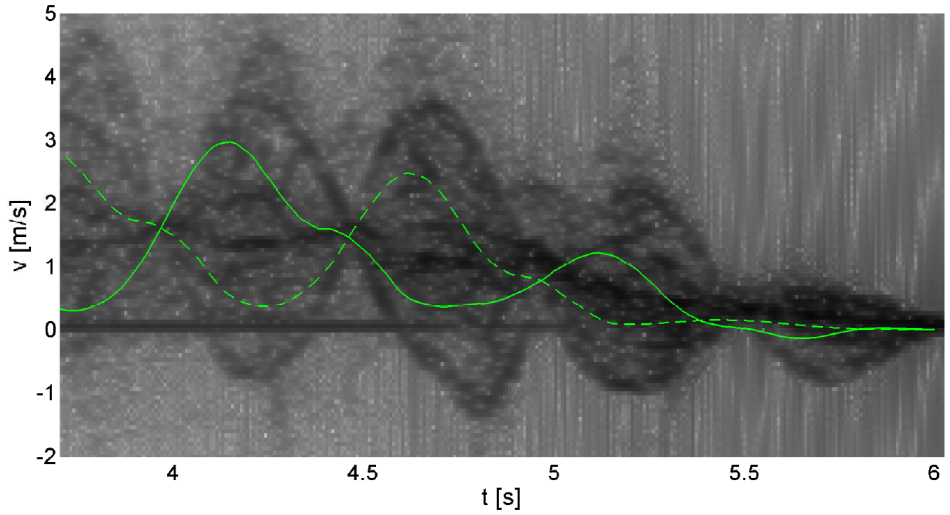

Figure 50: Mean RLE/RME (solid line) and LLE/LME (dashed line) radial velocities superimposed to the spectrogram.

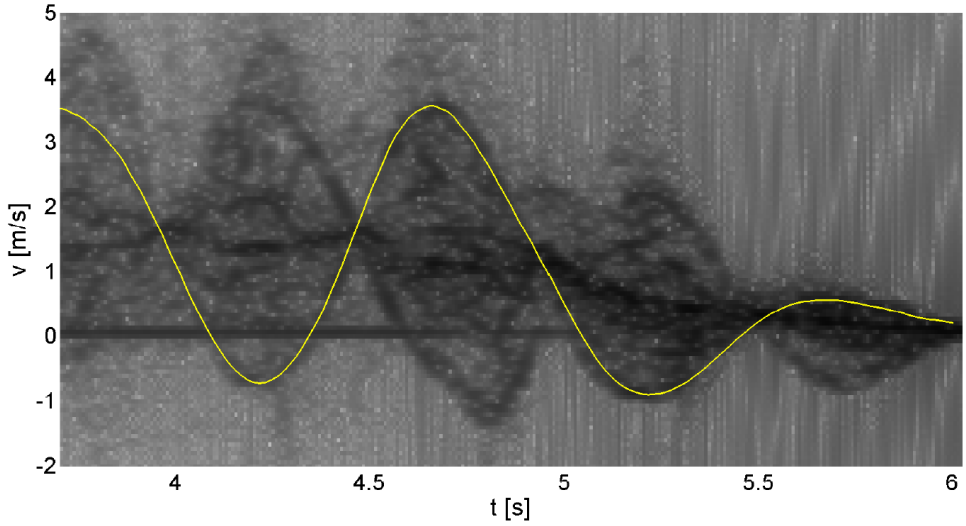

Figure 51: Mean HD radial velocity superimposed to the achieved spectrogram.

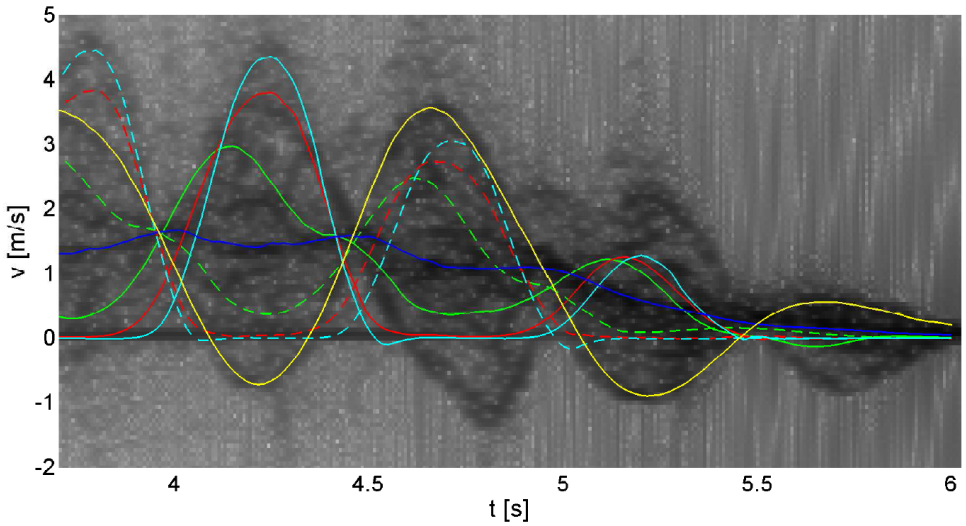

Figure 52: Superposition of the radial velocity trajectories with the achieved spectrogram: RLE/RME (solid green); LLE/LME (dashed green); RLM/RMM (solid red); LLM/LMM (dashed red); RVMH/RIMH (solid cyan); LVMH/LIMH (dashed cyan); HD (yellow); IJ/PX (blue).

ployed markers protocol (Figure 36a), the whole left arm has not been labelled with reflectors.

Based on the achieved characterisation results, the estimation of some body parts trajectories represents a very challenging task, especially for complex movements. The spectrogram traces can be discerned only for some particular movements, that have to be predefined according to the ultrasound system characteristics.

Instead, the overall micro-Doppler signatures as displayed on spectrograms show a very unique signature of the human motion, that can be deployed for human identification and recognition purposes.

5

HUMANS CLASSIFICATION IN ULTRASOUND DATA

Following the measurement approach presented in Chapter 2, a measurement setup has been realised, to be used for collecting and classifying human micro-Doppler signatures. Thus, the approach has been tested in the case of ultrasounds, by deploying the developed ultrasound Doppler system, presented and characterised on Chapters 3 and 4. The measurement setup consists of a treadmill hosting the analysed Human Target (HT), the developed UDS, and a post-processing unit for extracting μ-D features and classifying the analysed HT. Aim of the section is to present the system and to show how it can be profitably used for the identification of pre-registered walking individuals, with very good accuracy levels with respect to current applications and references. To this aim, a set of ultrasound μ-D signatures from 10 different human targets have been gathered, from which a set of features describing each HT has been extracted. Finally, the classification of the HTs has been carried out by using three different classifiers.

5.1 EXPERIMENTAL SETUP

The measurement system for the identification of human targets has been realised according to the architecture sketched in Figure 53. It is composed of the following elements: (i) an electric treadmill hosting the HT and allowing it to walk steadily and comfortably at different velocities v_{ht}; (ii) the developed ultrasound Doppler system working as a transceiver; (iii) a support for the positioning of the UDS at a height $h_{tr} = 0.9$ m from the treadmill carpet; (iv) a LeCroy HRO64Zi 2GS/s Digital Signal Oscilloscope (DSO) for the acquisition of the received signal $v_{rx}(t)$, (v) a laptop for the processing of the DSO's acquired signals; (vi) a motor driver for the treadmill motor and the control of v_{ht}.

The UDS consists of an ultrasound Tx-Rx pair built as described in Chapter 3, with low-cost and off-the-shelf components, and characterised by an operating frequency f_c nearly equal to 40 kHz. The UDS has been set to work in *continuous mode*, i.e. transmitting a continuous sinusoidal wave. Rx collects the incident echoes, and amplifies the signals by a 40

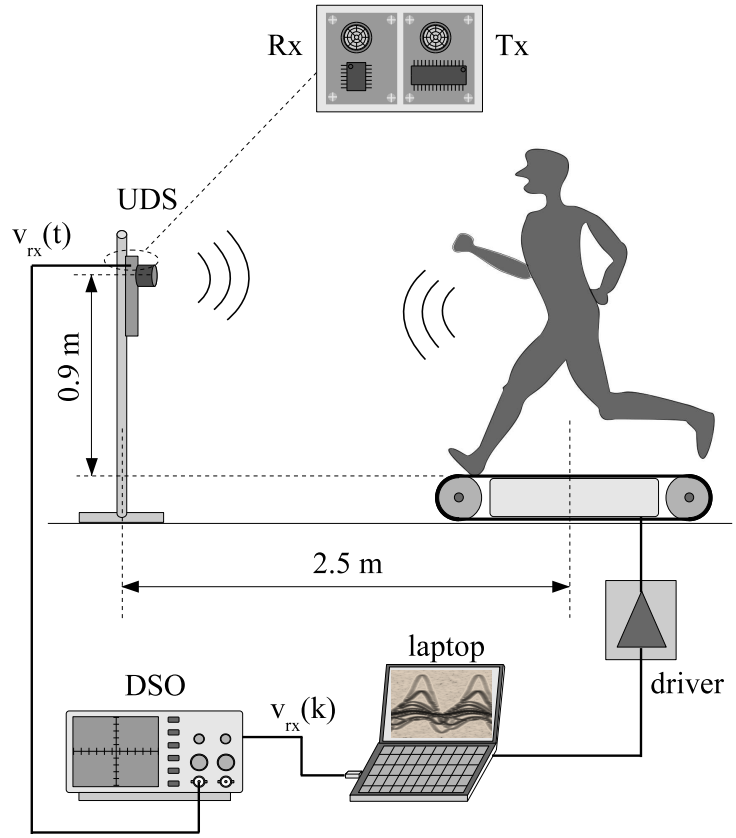

Figure 53: Measurement setup for human motion analysis.

dB factor, to be then forwarded to the oscilloscope. The DSO operates at a reduced sampling rate F_s equal to 100 kS/s over an acquisition time interval equal to 10 s. It performs a uniform sampling of $v_{rx}(t)$ providing sequences of 12 bit samples $v_{rx}(nT_s)$, with n integer and where $T_s = 1/F_s$ is the sampling time.

5.2 SIGNAL PROCESSING

The acquired ultrasound echoes have been saved on a laptop to be post-processed by a Matlab-developed program. The processing task is made up of a six stages sequence. Firstly, $v_{rx}(nT_s)$ is frequency down-converted. Indeed, the micro-Doppler information about HT is contained within a limited frequency band, around f_c. Hence, $v_{rx}(nT_s)$ is translated in a lower frequency band. Then, the STFT is applied to achieve a spectrogram representation of the micro-Doppler signature induced by the HT. The spectrogram is then transformed into a new image, from which a set of features are extracted, describing synthetically the HT motion characteristics. Finally, the features are forwarded to a classifier to recognise the

HT identity. The details of every stage regarding the signal processing are below provided.

5.2.1 *Frequency down-conversion*

The first operation is a frequency down translation of $v_{rx}(nT_s)$ by a quantity $f_{dc} = f_c - 1$ kHz. The output is a new sampled signal $v_{dc}(nT_s)$, defined as $v_{dc}(nT_s) = v_{rx}(nT_s) \cdot e^{-j2\pi f_{dc} nT_s}$, and where j is the imaginary unit. This operation shifts the spectrum of $v_{rx}(nT_s)$ around 1 kHz, allowing to reduce the computational burden of the subsequent processing stages and at the same time preserves the desired bandwidth and spectral content. The frequency translation is carried out: 1) multiplying $v_{rx}(nT_s)$ by a $f_{dc} = 39$ kHz cosine function, 2) filtering the result by means of a second-order low pass filter having a cut-off frequency equal to 7 kHz. A decimation is also applied after the down conversion stage so that to reduce the computational burden. F_s is decreased from 100 to 14 kHz. The adopted setup allows a maximum signal bandwidth equal to 2 kHz, which, according to Eq. (1), gives a detectable speed range equal to [-4.5, 4.5] m/s.

5.2.2 *Short Time Fourier Transform*

The second operation is a STFT carried out on the down converted samples $v_{dc}(nT_s)$. Such samples are ordered in such a way as to form time windows partially overlapped one with another. Each window has a length N_w equal to 2048 and a 90% overlapping with the adjacent ones. In each window, samples are shaped by a Hanning windowing and transformed by a STFT algorithm. STFT provides a sequence of frequency traces, $S(hT_w, kF)$, where k is the index denoting the position of the k-th frequency bin, with $k = 1, ..., N_w$, h is the index denoting the h-th window, and $T_w = N_w \cdot T_s/10 \cong 14.63$ ms is the time delay between two adjacent windows. The obtained traces $S(hT_w, kF)$, characterised by a frequency resolution $F = 1/\Delta T_s \cong 6.83$ Hz, with $\Delta T_s = N_w \cdot T_s \cong 146.3$ ms, are reported on a frequency versus time diagram, i.e. a spectrogram, showing the time evolution of the frequencies associated to the signal backscattered by the HT under analysis.

5.2.3 *Fast Fourier Transform*

A further transformation is applied in order to better highlight the periodicities associated to the spectrogram trajectories. Transformation consists of a Hanning windowing followed by a FFT, both applied along each row of the spectrogram, i.e. for each k, with $k = 1, ..., N_w$, to each function $S(hT_w, kF)$. The operation provides a new image on a frequency versus frequency diagram $C(h'F', kF)$, called *cadence map*, which gives a picture of the periodicity associated to the spectrogram trajectories.

5.2.4 *Human target features extraction*

In Figure 54a, an example of a spectrogram $S(hT_w, kF)$ and a cadence map $C(h'F', kF)$ is shown, achieved in the presence of a HT walking on the treadmill, and where f_d, f, and t denote kF, $h'F'$, and hT_w, respectively. The spectrogram highlights a superimposition of periodical trajectories, each related to the motion of a corresponding body part, and providing a unique signature of HT. The cadence map instead shows the main frequencies associated to the analysed HT's gait and an estimate of the maximum velocities reached by the body parts. From such images, the parameters $\{\hat{X}_1, \hat{X}_2, \ldots, \hat{X}_L\}$ and the corresponding reference values $\{\hat{X}_{R,1}, \hat{X}_{R,2}, \ldots, \hat{X}_{R,L}\}$ introduced in Figure 10 can be estimated. As described on the designed measurement approach reported in Chapter 2, the two set of values, $\{\hat{X}_i\}$ and $\{\hat{X}_{R,i}\}$ represent two set of features that can be extracted from the micro-Doppler signature to synthetically characterised the analysed HT.

Three possible features are shown in Figure 54, and correspond to three kinematic characteristics of the human gait: 1) $\hat{X}_1 = f_{cad}/\sqrt{v_{ht}}$, related to the step cadence frequency; 2) $\hat{X}_2 = (\frac{f_{d,max} \cdot c}{2f_c})/v_{ht}$, related to the maximum velocity reached by the body parts; 3) $\hat{X}_3 = (\frac{f_{d,min} \cdot c}{2f_c})/v_{ht}$, related to the minimum velocity reached by the body parts, where v_{ht} is the average walking speed measured from the treadmill speed control system and c is the sound propagation speed in air (343.8 m/s, at a 20^oC environmental temperature). These three parameters are strictly related to the physical structure of the HT as well as his walking style. For example: - all of the three parameters are strictly related to the human height, - the asymmetries in the walking style strongly influence $f_{d,max}$ and $f_{d,min}$, - taller persons typically have a lower step cadence frequency than shorter

ones, etc. These relationships allow creating a connection between measurable parameters $\{\hat{X}_i\}$ and HT physical characteristics. As shown in Figure 54, f_{cad}, $f_{d,max}$ and $f_{d,min}$ can be estimated from the spectrogram, but also, and better, from the cadence map, in particular: f_{cad} from the x-axis position of the first frequency component, $f_{d,max}$ and $f_{d,min}$ from the peak amplitudes, positive and negative respectively, associated to the component at f_{cad} frequency. From the estimation of f_{cad}, $f_{d,max}$ and $f_{d,min}$, the values of the parameters $\hat{X}_1$, $\hat{X}_2$ and $\hat{X}_3$ can be computed.

Another possible parameter (an array), $\hat{X}_4$, is obtained from the cadence map $C(f, f_d)$ and in particular from the values assumed at $f = f_{cad}$, as $\hat{X}_4(f_d) = C(f_{cad}, f_d)$. An example of this function, from the case of Figure 54b, is shown in Figure 55. It represents the Doppler spectrum of the signal backscattered by the HT associated to the only body parts moving at the f_{cad} frequency. Such a trace can be considered as a further signature of that HT. The three introduced parameters $\{\hat{X}_i$, with i =1,.., 3$\}$ and the spectral function $\hat{X}_4(f_d)$ are finally used as input values of two classifiers, below introduced, for the identification of the analysed HT.

5.2.5 *Bayesian classifier*

A Bayesian classifier is a simple and well-known probabilistic classifier based on the Bayes theorem and requiring a strong independence relationship among the input variables. It allows to identify a subject S_i starting from a set of estimated parameters like the three ones above considered: $\hat{\mathbf{X}} = [\hat{X}_1, \hat{X}_2, \hat{X}_3]$, where $\hat{\mathbf{X}}$ is called parameters vector. A set of discriminant functions $g_k(\hat{\mathbf{X}})$, each associated to a subject S_i, are used to process and judge these values. In particular, the vector $\hat{\mathbf{X}}$ is assigned to the subject class S_i if and only if $g_i(\hat{\mathbf{X}}) > g_k(\hat{\mathbf{X}})$ for every $i \neq k$. This is known as the maximum a posteriori decision rule. By the Bayes theorem, the conditional probability $P(S_i|\hat{\mathbf{X}})$ can be written as follows:

$$P(S_i|\hat{\mathbf{X}}) = \frac{p(\hat{\mathbf{X}}|S_i)P(S_i)}{p(\hat{\mathbf{X}})}, \tag{17}$$

where $p(\hat{\mathbf{X}}|S_i)$ is the probability density function of $\hat{\mathbf{X}}|S_i$, $P(S_i)$ is the probability of the S_i presence, and $p(\hat{\mathbf{X}})$ is the probability density function of $\hat{\mathbf{X}}$. Under the hypothesis that $p(\hat{\mathbf{X}})$ is constant and positive, and that, as in the present application, $P(S_i)$ is constant, the evaluation of $P(S_i|\hat{\mathbf{X}})$ can be reformulated in terms of discrimination functions, and by

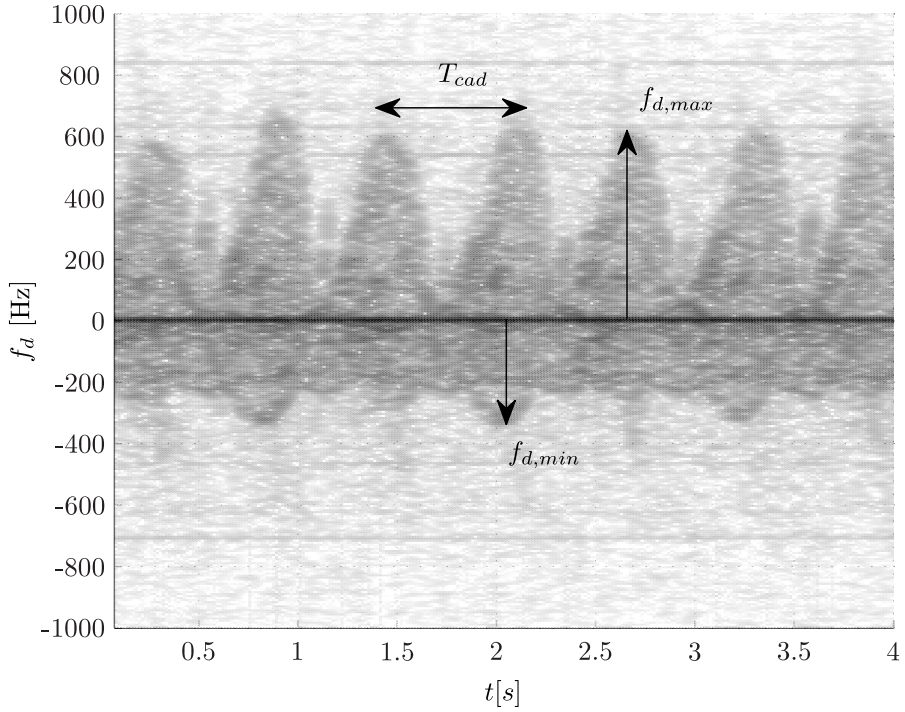

(a)

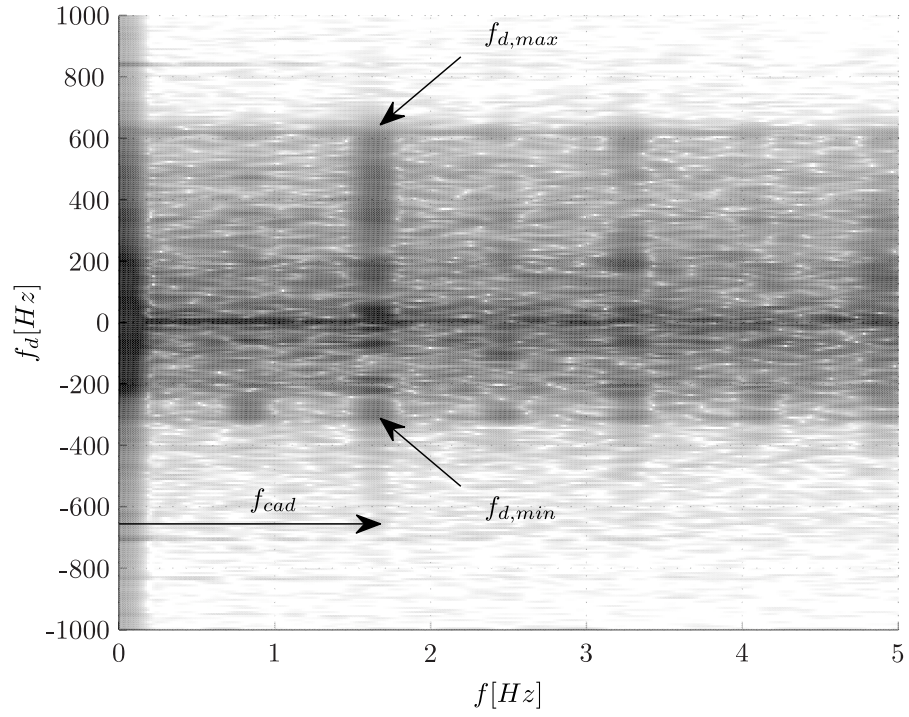

(b)

Figure 54: Examples of: a) a spectrogram; b) a cadence map, and the corresponding estimated parameters.

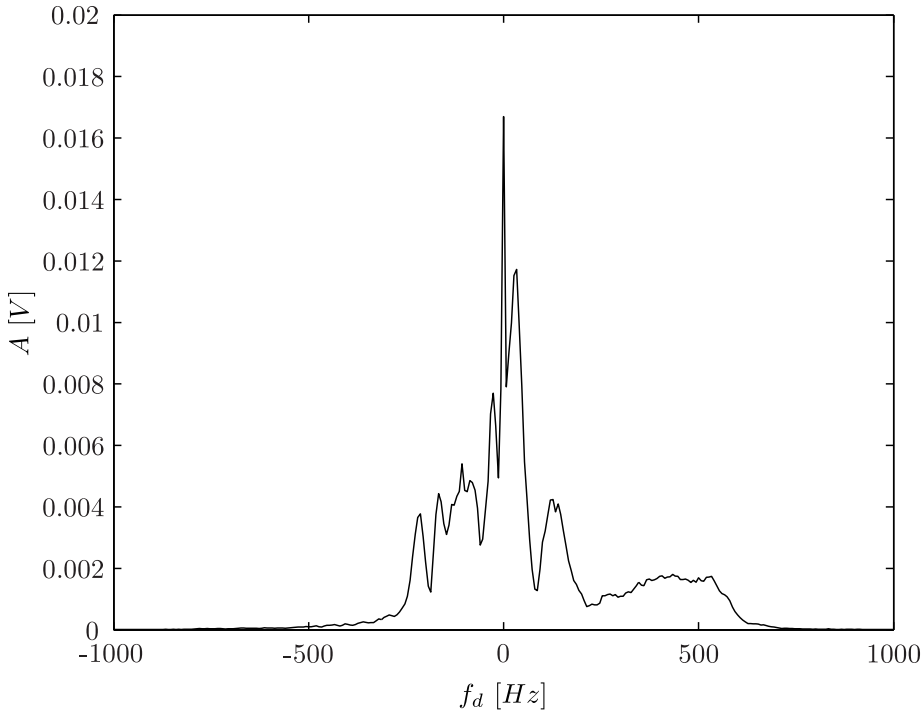

Figure 55: Example of a Doppler spectrum $\hat{X}_4(f_d)$ obtained from Figure 54b.

evaluating only $p(\hat{\mathbf{X}}|S_i)$. Posed that $p(\hat{\mathbf{X}}|S_i)$ is normal, it can expressed as:

$$P(\hat{\mathbf{X}}|S_i) = \frac{1}{(2\pi)^{\frac{3}{2}}\,|\Sigma_i|^{\frac{1}{2}}}\,\mathrm{e}^{-\frac{1}{2}(\hat{\mathbf{X}}-\mu_i)^T\Sigma_i^{-1}(\hat{\mathbf{X}}-\mu_i)}, \tag{18}$$

where μ_i and Σ_i are the expectation and covariance matrix of $\hat{\mathbf{X}}|S_i$. From Eq. (18), by applying a logarithmic monotonic function and considering that $(2\pi)^{\frac{3}{2}}$ is constant, the i-th discriminant function $g_i(\hat{\mathbf{X}})$ can be defined as follows:

$$g_i(\hat{\mathbf{X}}) = -\frac{1}{2}[\ln|\Sigma_i| + (\hat{\mathbf{X}}-\mu_i)^T\Sigma_i^{-1}(\hat{\mathbf{X}}-\mu_i)], \tag{19}$$

where μ_i and Σ_i are determined during a "training procedure", required at the beginning to register the i-th subject S_i. The measured input vector $\hat{\mathbf{X}}$ is thus assigned to the i-th subject S_i if the i-th discriminant function $g_i(\hat{\mathbf{X}}) > g_k(\hat{\mathbf{X}})$, for every $k \neq i$. Such a S_i represents, in this case, the subject having the best likelihood to be the one corresponding to the analysed HT.

5.2.6 *Shape similarity spectrum classifier*

The second classifier is based on the analysis of the correlation between $X_4(f_d)$ and a set of N_S reference spectra $\{\hat{X}^i_{R,4}(f_d)\}$ pre-registered during

a training procedure performed on the subjects S_i, with $i = 1, ..., N_S$. The correlation between the trace $X_4^x(f_d)$ measured from an unknown target x and the i-th reference spectrum is assessed by evaluating the Pearson correlation coefficient $\rho_{x,i}$ defined as:

$$\rho_{x,i} = \frac{\text{cov}(\hat{X}_4^x(f_d), \hat{X}_{R,4}^i(f_d))}{\sigma_x \, \sigma_i}, \tag{20}$$

where σ_x and σ_i are the standard deviation associated to the two spectra. The classification is performed by associating to the analysed HT the subject S_i having the highest coefficient $\rho_{x,i}$.

5.3 DATABASE CREATION

A first measurement campaign has been carried out with the aim of gathering a set of reference values $\{\hat{X}_{R,1}, \hat{X}_{R,2}, \hat{X}_{R,3}\}$ and N_S reference traces $\{\hat{X}_{R,4}^i(f_d)$ with $i = 1, ..., N_S\}$ according to the approach described in Figure 10, to be used for the subsequent experiments. To this aim, ten subjects S_i have been analysed walking on the treadmill of Figure 53 and having different height (between 1.58 and 1.92 m) and weight (between 50 and 90 Kg). For each of them, a set of $N_o = 10$ observations have been performed, for a total of 100 acquisitions. Data registration has been performed after a warm-up time interval of one minute length, to allow the HT walking on the treadmill in a steady way. The mean walking speed v_{ht} has been monitored during all the measurement stage. The results obtained in terms of $\hat{X}_1$, $\hat{X}_2$ and $\hat{X}_3$ are summarised in Figure 56 and 57 in the form of $2\sigma_i$-amplitude intervals centred around their mean values and where σ_i is the standard deviation for each set of N_o observations. Such intervals, as well as the mean values for each subject, are recorded as reference values $\hat{X}_{R,1}$, $\hat{X}_{R,2}$ and $\hat{X}_{R,3}$ for subsequent identification tasks. The three sets of results show that the intervals, despite some overlapping, are different in terms of amplitude and position. Through the Bayesian classifier, such differences allow to identify the most likelihood subject S_i to be assigned to the analysed HT.

In Figure 58 and 59, an example of reference trace $\hat{X}_{R,4}^7(f_d)$ obtained in the presence of S_7 after ten acquisitions and an average operation performed frequency by frequency, is shown and compared with two observed traces: $\hat{X}_4^7(f_d)$ and $\hat{X}_4^2(f_d)$. The traces show that between $\hat{X}_{R,4}^7(f_d)$ and $\hat{X}_4^7(f_d)$ there is a much more visible similarity than that existing between $\hat{X}_{R,4}^7(f_d)$ and $\hat{X}_4^2(f_d)$. This similarity is confirmed by a Pearson

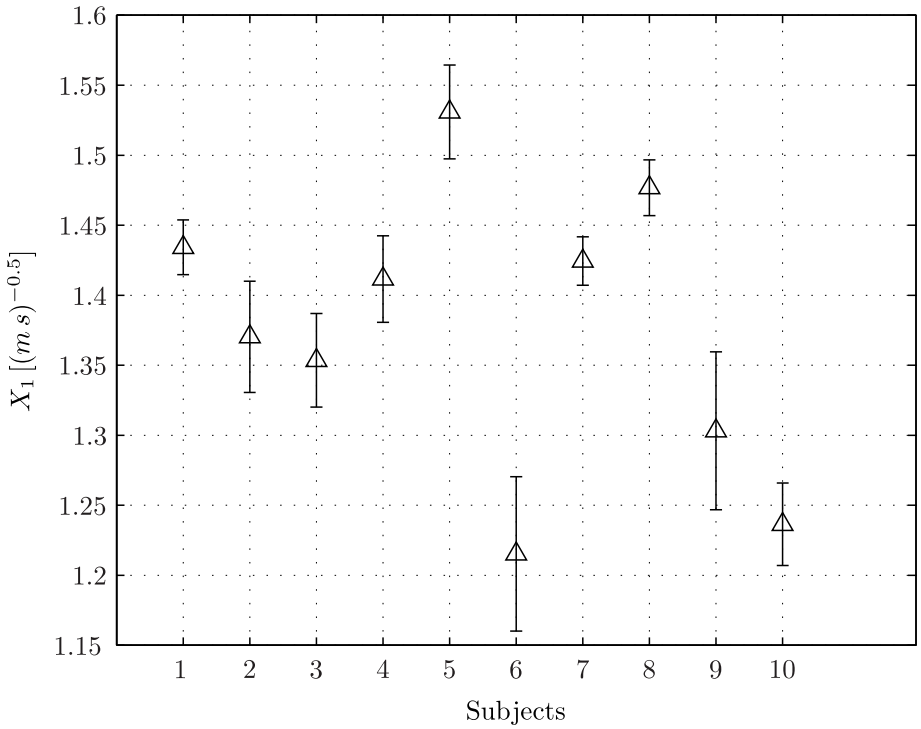

Figure 56: Estimates of $\hat{X}_{R,1}$ for the N_S analysed subjects.

coefficient $\rho_{7,7} = 0.962$ higher than $\rho_{7,2} = 0.906$. Through the spectrum classifier, such differences allow to identify the most likelihood subject S_i to be assigned to the analysed HT.

5.4 EXPERIMENTAL RESULTS

A variable and randomly chosen subset of preliminary observations for each S_i has been used for evaluating the reference values $\{\hat{X}_{R,1}, \hat{X}_{R,2}, \hat{X}_{R,3}\}$ and traces $\{\hat{X}^i_{R,4}(f_d)\}$ (training stage) required to identify the subjects. t_r is defined as the percentage of observations N_o used in the training procedure.

Subsequently, a second measurement campaign has been carried out with the aim of assessing the effectiveness of the proposed system (validation stage), as well as the performance of the deployed classifiers. A number of $N_r = 10$ readings have been performed for every analysed subject S_i, with $i = 1, ..., N_S = 10$. Performance have been evaluated in terms of the parameter *success rate*, s_r, intended as the ratio between the number of times in which the HTs are correctly identified and the total number of readings, i.e. $N_S \cdot N_r$.

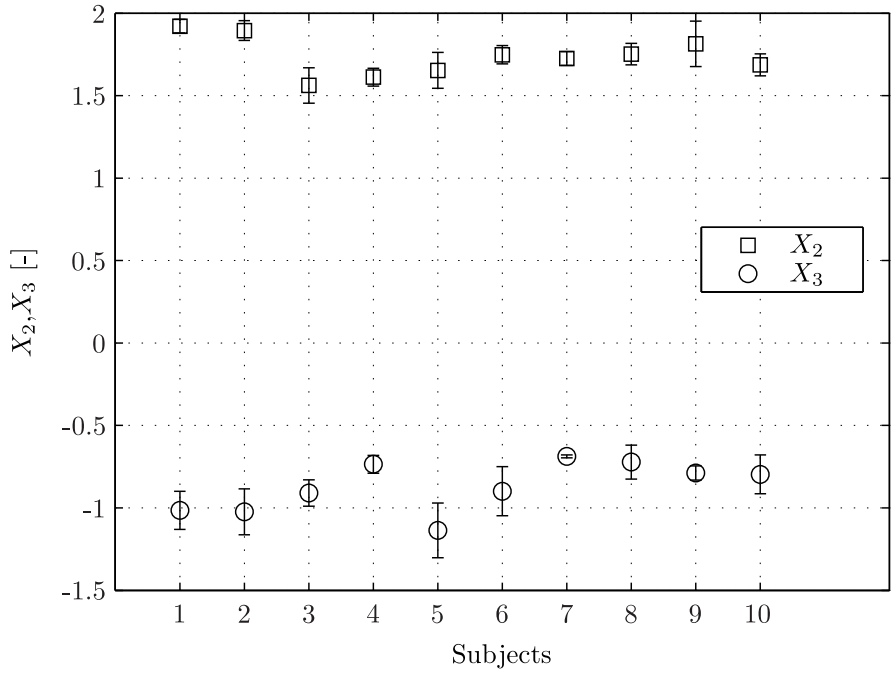

Figure 57: Estimates of $\hat{X}_{R,2}$ and $\hat{X}_{R,3}$ for the N_S analysed subjects.

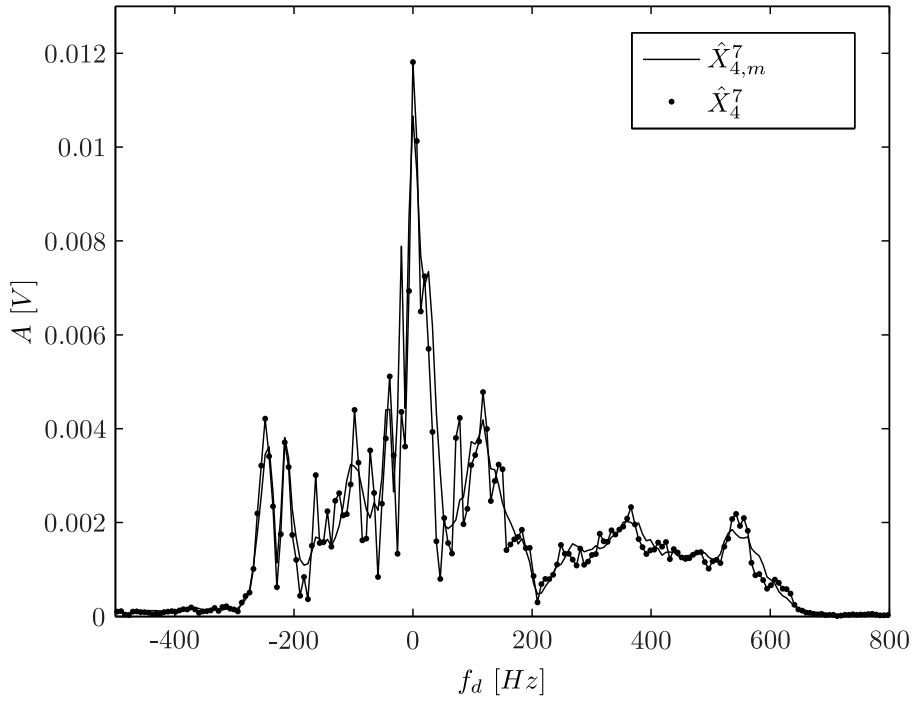

Figure 58: Comparison between the reference trace $\hat{X}^7_{R,4}(f_d)$ obtained from the analysis of S_7 and an observed trace $\hat{X}^7_4(f_d)$ associated to S_7.

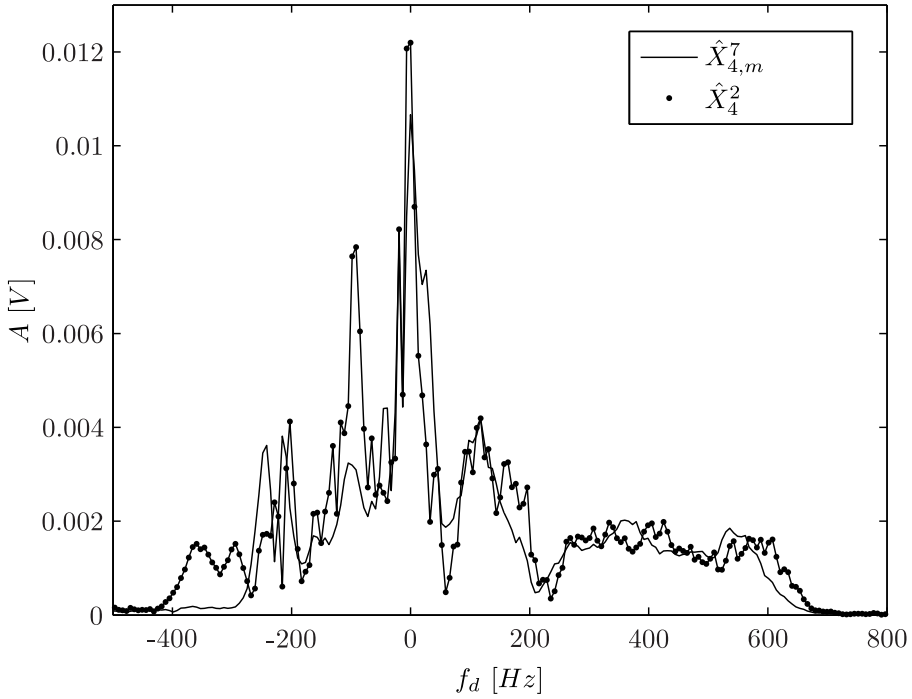

Figure 59: Comparison between the reference trace $\hat{X}^7_{R,4}(f_d)$ obtained from the analysis S_7 and an observed trace $\hat{X}^2_4(f_d)$ associated to S_2.

5.4.1 *Bayesian classifier*

In Figure 60a, the obtained percentage values of s_r are shown upon the variation of the parameter t_r, from 30 to 80%. These results have been achieved by deploying the Bayesian classifier and all of the three considered parameters $\{\hat{X}_1, \hat{X}_2, \hat{X}_3\}$. An interval is also shown around the mean value to indicate the dispersion of the results. The amplitude of these intervals is equal to $2 \cdot \sigma_{s_r}$ where σ_{s_r} is the standard deviation of the obtained estimates of s_r. The diagram highlights the importance of the training procedure in the performance rate of the system. The greater t_r the greater s_R. It can also be seen that the increasing of s_r tends to saturate. This means that the increasing of t_r can become useless beyond a given threshold, and thus other improvements or solutions are needed in this case.

In Figure 60b, the estimated values of s_r are shown upon the variation of the number of parameters (N_p) used by the Bayesian classifier and with a constant training set percentage equal to 70%. In particular, the following conditions have been considered: (i) $N_p = 1$ with only $\hat{X}_1$; (ii) $N_p = 2$ with $\hat{X}_1$ and $\hat{X}_2$; (iii) $N_p = 3$ with $\hat{X}_1$, $\hat{X}_2$, and $\hat{X}_3$. The results

Table 5: Confusion matrix for the Bayesian classier applied with a 70% of training measures.

	S_1	S_2	S_3	S_4	S_5	S_6	S_7	S_8	S_9	S_{10}
S_1	71	21	0	0	2	0	0	0	6	0
S_2	11	73	2	1	0	4	9	0	0	0
S_3	0	0	71	17	0	1	0	0	1	10
S_4	0	0	10	73	0	0	4	13	0	0
S_5	0	6	0	4	85	0	0	5	0	0
S_6	0	1	6	0	0	50	0	0	2	41
S_7	0	7	0	2	0	0	74	17	0	0
S_8	0	3	2	5	15	0	12	63	0	0
S_9	1	9	0	0	0	6	0	0	56	28
S_{10}	0	0	1	0	0	33	0	0	29	37

highlight that N_p strongly influences the system performance, and that the relationship between s_r and N_p is nearly linear. This suggests that the Bayesian classifier performance can be improved by increasing the number of considered variables.

In Table 5, a confusion matrix is reported summarising the results of the identification process, in percentage units, in the case of $t_r = 70\%$ and $N_p = 3$. The index of the table rows indicates the subject to identify, while the one of the column indicates the subject classified. In the table, only the values lying on the main diagonal can be considered as s_r estimates. The remaining ones are failure indexes showing errors in the identification process. For example, S_6 has been identified as S_{10} about the 41% of attempts. On the contrary, S_{10} has been identified as S_6 about the 33% of attempts. In other words, the system tends to confuse subjects 6 and 10, and this could probably be due to the similarity of the analysed HTs, regarding the gait styles as well as the physical structure. It could be also due to the fact that S_6, as shown in Figure 56, is characterised by a very wide standard deviation, probably due to some problems experienced by S_6 in walking on the treadmill.

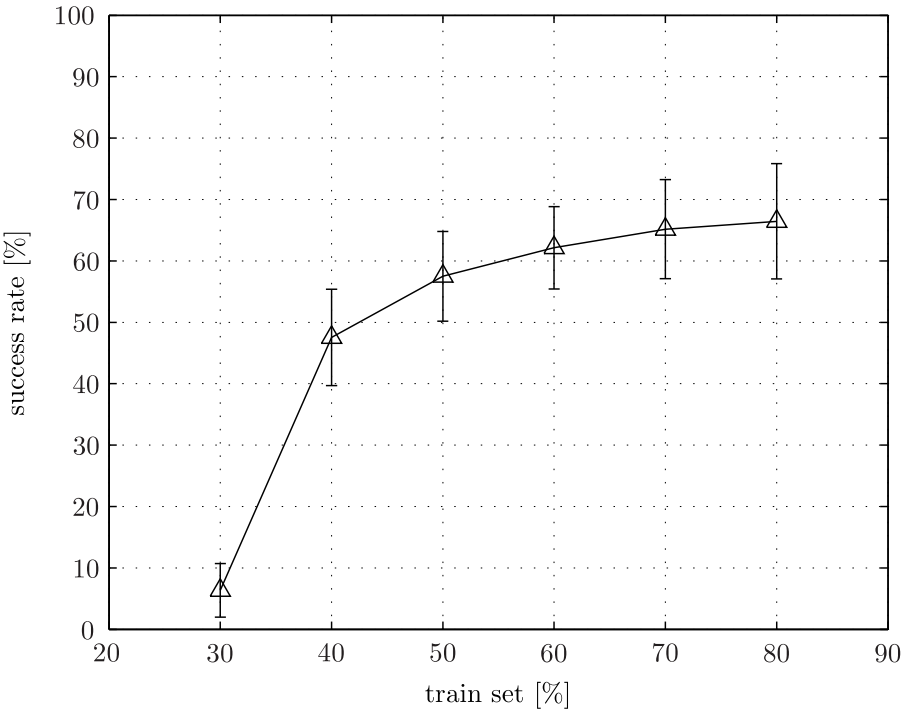

(a)

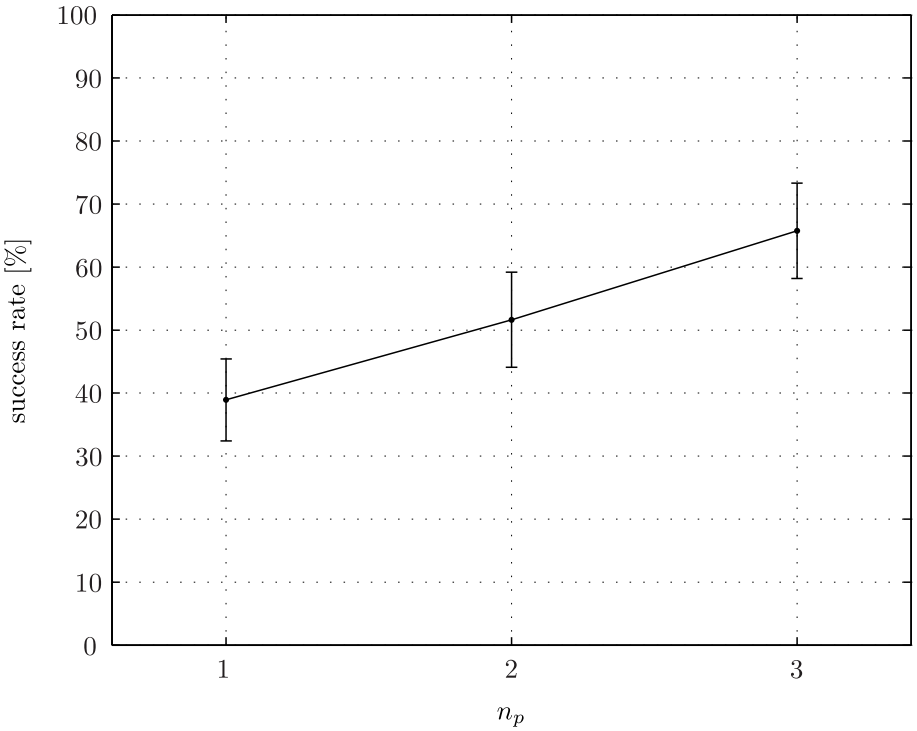

(b)

Figure 60: Bayesian classifier performance upon the variation of: a) t_r; b) number of employed parameters.

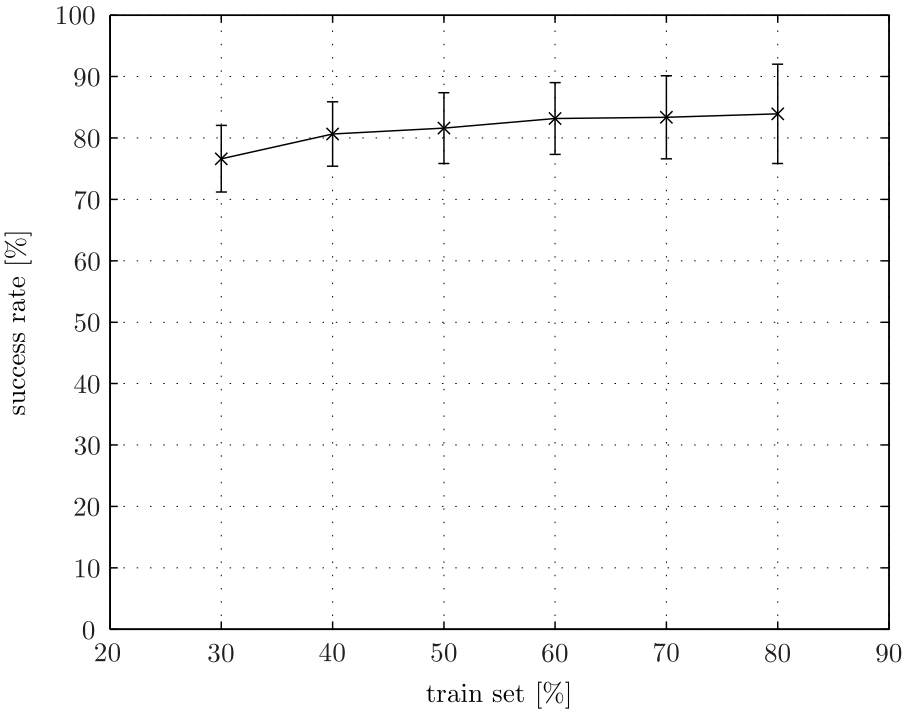

Figure 61: Performance of the spectrum classifier upon the variation of t_r.

5.4.2 *Spectrum classifier*

In Figure 61, another set of s_r estimates are shown upon the variation of t_r from 30 to 80%. These results have been achieved by deploying the spectrum classifier and the procedure illustrated in Section 5.2.6. With respect to the Bayesian classifier, the spectrum one provides much better results, around 80%. In this case, the percentage of measures considered for the training procedure seems to less influence s_r. The curve is in fact positive in the slope but rather flat, with respect to that of Figure 60a.

From a comparison between the two classifiers, one can note: (i) the spectrum classifier can achieve higher performance; (ii) the spectrum classifier does not need to consider many measures for the training stage; (iii) the spectrum classifier requires a higher database size for each target (reference values are arrays not scalars). In Table 6, the confusion matrix for the Spectrum classifier is shown in the case of a training set percentage equal to 70%. It can be noticed that 7 of 10 subjects are successfully classified in the 80% of tests.

Table 6: Confusion matrix for the spectrum classier applied with a 70% of training set.

	S_1	S_2	S_3	S_4	S_5	S_6	S_7	S_8	S_9	S_{10}
S_1	94	0	0	0	2	0	0	4	0	0
S_2	10	82	0	0	0	0	1	7	0	0
S_3	0	0	56	0	0	0	26	18	0	0
S_4	0	0	0	100	0	0	0	0	0	0
S_5	0	0	0	0	98	2	0	0	0	0
S_6	0	0	1	0	0	95	0	1	0	3
S_7	0	0	7	0	0	0	92	0	0	1
S_8	17	0	7	0	2	0	7	67	0	0
S_9	0	0	0	0	0	6	0	0	82	12
S_{10}	0	0	1	0	0	17	3	0	11	68

5.4.3 *Combined classifier*

A third classifier has been implemented by deploying both the two considered classifiers, and adopting the information contained in the confusion matrices. Both the classifiers provide an estimation of the recognised target. If the results disagree, the outcome is picked from the classifier having a lower probability to fail, according to the two previously achieved confusion matrices. This allows to strongly reduce the number of false identifications and increase the number of successful ones. For example, with a 70% of measures used as a training set, a mean success rate equal to 88.9% has been obtained, much higher than the Bayesian and the spectrum classifier, which in the same conditions provided values of s_r respectively of 65.1% and 83.3%.

6

HUMANS CLASSIFICATION IN RADAR DATA

In this chapter, the effectiveness of the designed measurement approach described in Chapter 2 has been verified in the case of radio-frequency signals. During a six months abroad experience, it was possible to use the facilities of the Cranfield University, Defence academy of the United Kingdom. The chapter presents the results of an experimental trial to collect micro-Doppler signatures of four different human targets walking and running on a treadmill, by using a continuous wave radar operating at 10 GHz (X-band). An analysis of recognition performance has been carried out on the experimental data using the developed features for both a Naïve Bayesian classifier and a shape-similarity-spectrum classifier. Recognition performance has been assessed as a function of key parameters, such as the dwell time on the target and the size of the training set, to investigate the level of robustness of the proposed features. Results show that high level recognition performance can be achieved for both walking and running humans.

In the last part of the chapter, a comparison between ultrasound and radar μ-D signatures classification has been performed. In particular, nine persons have been asked to walk and run on a treadmill, while monitored by both a 10 GHz radar and a 40 kHz ultrasound system. Radar and ultrasound signatures have been gathered, to be then used for features extraction and target classification. Finally, a comparison between the two systems overall performance has been achieved, according to different training conditions.

6.1 EXPERIMENTAL SETUP

The measurements have been carried out at the Defence Academy of the United Kingdom in 2014 using a Continuous Wave (CW) radar operating at 10 GHz (X-band). A sketch of the experimental set up is shown in Figure 62a together with a photo taken at the time of the experiments (Figure 62b). The radar consists of two analogical outputs, which provide the in-phase (I) and in-quadrature (Q) components of the received signal, and is composed of two identical 2x3 cm horn antennas separated of 16

Table 7: Physical characteristics of the analysed human targets.

Target	**Height** [m]	**Weight** [Kg]	**Leg length** [m]	**Arm length** [m]
1	1.78	80	0.97	0.77
2	1.77	73	0.97	0.75
3	1.74	72	0.93	0.77
4	1.80	85	0.90	0.75

cm. The two antennas transmit and receive in cross-polarisation in order to increase isolation between the transmitting and the receiving channels.

The radar has been used to collect micro-Doppler signatures of four human targets performing two activities: walking at 5 m/s and running at 9 m/s on a treadmill at a distance of 2.9 m from the radar. The two radar antennas has been deployed at a height of 1.5 m above the ground level. The experimental geometry has been chosen so to have the entire target inside the antenna beams. The I component $s_I(t)$ and the Q component $s_Q(t)$ of the target echoes have been digitised with a TiPie HS4 oscilloscope at a sampling rate $F_s = 10$ kHz and with a 12-bit resolution. The digitised echoes have been then memorised in a file for post processing. A total of $N_m = 120$ micro-Doppler signatures of 10 s duration have been collected for each target and for each activity. The physical characteristics of the targets are given in Table 7.

6.2 DATA PROCESSING

The complex signal of each target echo $s(n) = s_I(n) + js_Q(n)$ has been obtained by combining the in-phase and in-quadrature components. The mean value of the data:

$$\eta = \frac{1}{N} \sum_{n=0}^{N-1} s(n),$$

has been subtracted from $s(n)$ to suppress the zero-Doppler components containing the contribution from stationary clutters. The target micro-

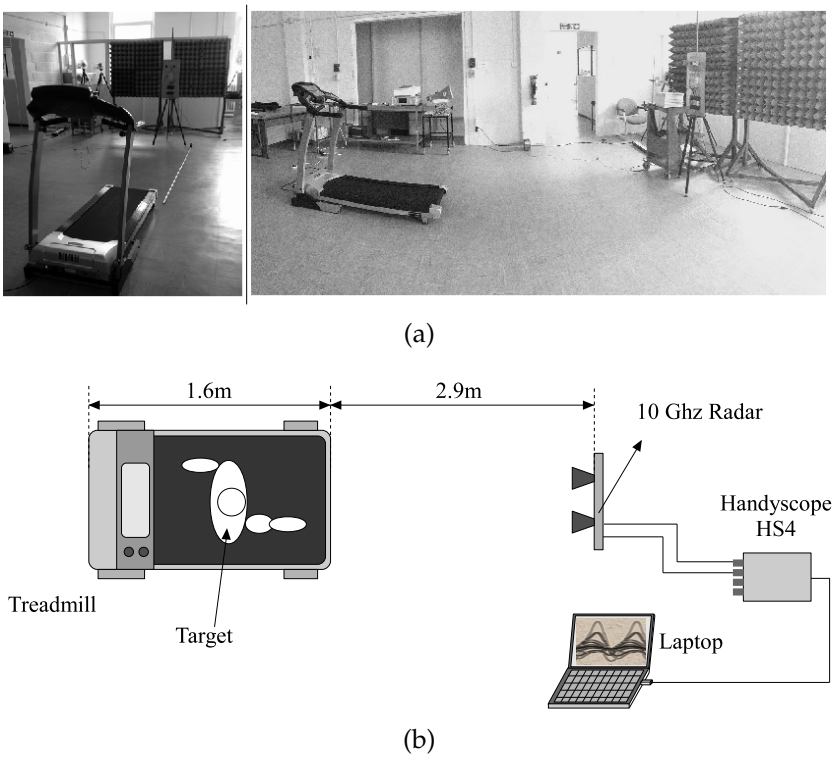

Figure 62: Picture (a) and sketch (b) of the employed measurement setup to record human μ-D signatures.

Doppler signatures have been extracted by calculating the STFT of $\hat{s}(n) = s(n) - \eta$ as:

$$\begin{aligned} &\hat{S}(l,K) = \frac{1}{N_w} \sum_{n=0}^{N_w-1} \hat{s}(n + l \cdot \Delta l)\, w(n)\, \mathrm{e}^{\frac{-j2\pi Kn}{N_1}}, \\ &K = 0 \ldots N_1 - 1, \\ &l = 0 \ldots N_b - 1, \end{aligned} \tag{21}$$

where $w(n)$ is an Hanning window of length N_w, N_1 is the number of points of the Fast Fourier Transform (FFT), Δl is the number of overlapping samples between two consecutive windows and N_b is the total number of windows.

Figure 63a shows the normalised amplitude of the STFT of Target 1 walking on the treadmill at 5 m/s. This has been obtained with a dwell time $T_w = N_w/F_s$ =0.15 s and with 50% overlapping windows. Results show the micro-Doppler signature of the target is periodic with a frequency of about 2 Hz which is typical of the motion characteristics of limbs in walking humans [25]. The maximum Doppler shift is induced by the movement of the foot moving away from the radar and is about to 400 Hz, corresponding to a velocity of 6 m/s. This is in agreement with

the experimental geometry and it has been corroborated by additional measurements in which the arms of the target have been kept stationary.

The STFT has been processed through a second FFT stage to generate the Cadence Velocity Diagram (CVD) $Y(m, K)$ as:

$$Y(m,K) = \frac{1}{N_b} \sum_{l=0}^{N_b-1} |\hat{S}(l,K)|\, w(l)\, \mathrm{e}^{\frac{-j2\pi ml}{N_2}}, \qquad (22)$$
$$K = 0 \ldots N_1 - 1,\ m = 0 \ldots N_2 - 1,$$

where N_2 is the number of points of the FFT calculated for each Doppler bin of the STFT and $w(l)$ is an Hanning window of the same duration of the micro-Doppler signature. The image $Y(m, K)$ does not depend on the initial phase of the gait cycle and hence is not a time-dependent representation of the human micro-Doppler signature. It is produced to extract the periodic properties of each Doppler bin of the micro-Doppler signature. Because each window of the STFT is generated every $T_{sw} = (N_w - \Delta_l)T_s = 1/F_{sw}$ seconds, the maximum step repetition frequency of the targets that can be detected without ambiguities is $F_{sw}/2$. The expression above can also be expressed as a function of the window duration T_w and the time of overlapping between two consecutive windows $T_{ovlp} = \Delta_l\, T_s$ as:

$$T_w - T_{ovlp} < \frac{1}{2\, F_{sw}}. \qquad (23)$$

The equation describes an hyperbole on the T_w-T_{ovlp} plane which identifies the aliasing free region.

Figure 63b shows the CVD of Target 1, obtained from the image of Figure 63a. The y-axis indicates the Doppler bins, corresponding to the Doppler frequency shifts induced by the target micro-motions whilst the x-axis represents the frequency components of each Doppler bin. Results show two main components: a first harmonic component which represents the repetition frequency of the target gait and a second harmonic component which appears as the oscillatory movement of the limbs is not a pure sine wave.

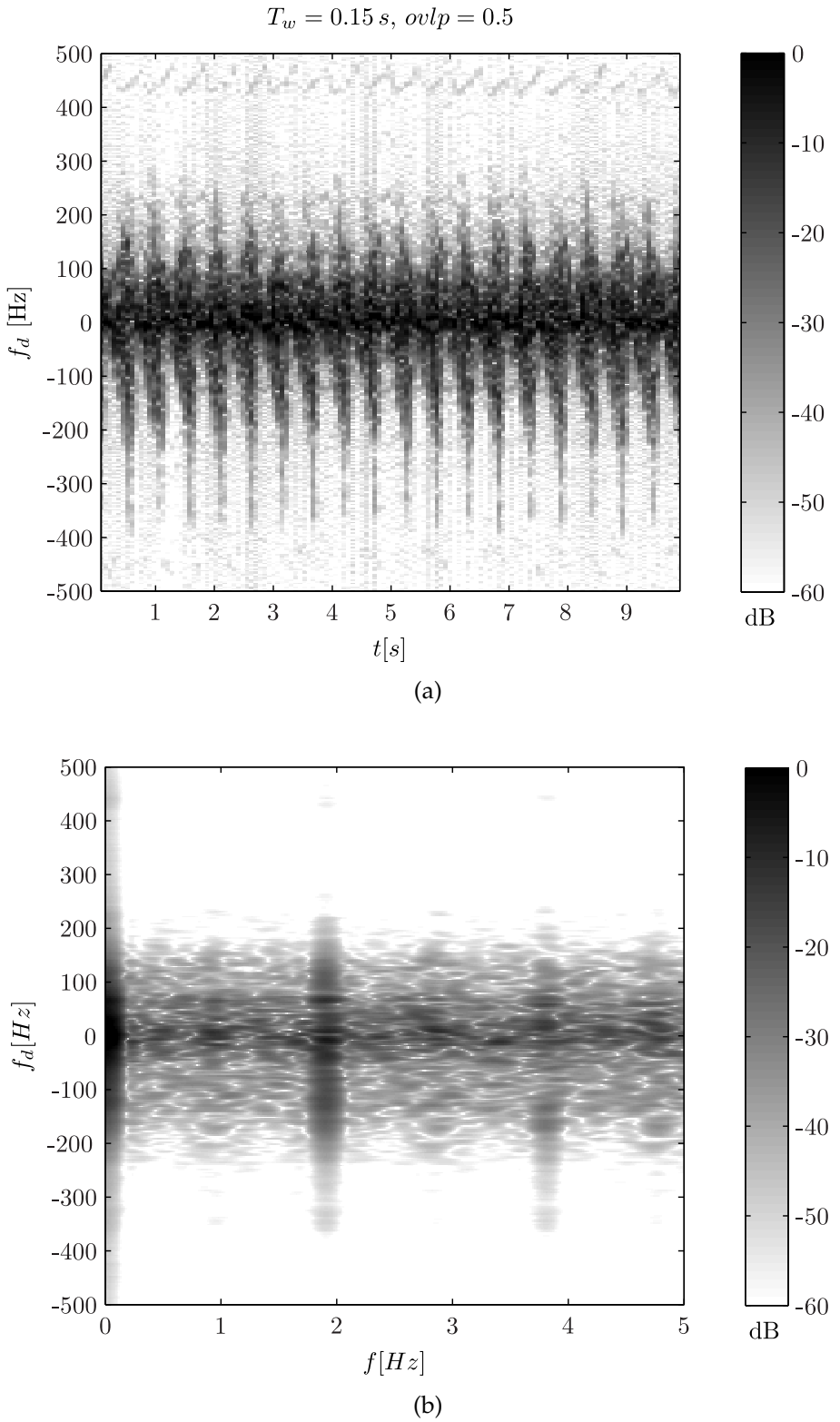

Figure 63: Representation of a spectrogram obtained from Target 1 (a), and the corresponding cadence-velocity diagram (b).

6.2.1 *Feature extraction*

The first feature f_1 represents the step cadence, or step repetition frequency of the micro-Doppler signature. It is obtained from $Y(m,K)$ by calculating the mean cadence spectrum $\bar{Y}(m)$ as:

$$\bar{Y}(m) = \frac{1}{N_1} \sum_{K=0}^{N_1-1} |Y(m,K)|, m = 0 \dots N_2 - 1. \tag{24}$$

The frequency that corresponds to the bin m_{pk} which gives the maximum value of $\bar{Y}(m)$ is an estimate of the step repetition frequency and is the feature $f_1 = m_{pk}/(Tsw * N_2)$.

The second feature f_2 and the third feature f_3 have been obtained by calculating the mean spectrum $\tilde{Y}(K)$ around f_1 as:

$$\tilde{Y}(K) = \frac{1}{2\,\Delta m + 1} \sum_{m=m_{pk}-\Delta m}^{m=m_{pk}+\Delta m} |Y(m,K)|, \quad K = 0 \dots N_1 - 1. \tag{25}$$

$\tilde{Y}(K)$ represents the mean spectrum over $2\,\Delta m + 1$ samples along the x-axis of $Y(m,K)$ and around the frequency f_1. In the equation Δm is an integer number which describes the size of the averaging window. It has been experimentally found that suitable values for Δm range between 1 and 5. The maximum and minimum values of $\tilde{Y}(K)$, $\tilde{Y}_{max}$ and $\tilde{Y}_{min}$, have been calculated to determine the value of the threshold $T = (\tilde{Y}_{max} - \tilde{Y}_{min})\gamma$, with γ being a number between 0 and 1. The first sample K_1 for which $\tilde{Y}(K_1) > T$ has been used to determine the feature $f_2 = K_1 * F_{sw}/N_1$. Similarly, the last sample K_2 for which $\tilde{Y}(K_2) > T$ has been used to determine the feature $f_3 = K_2 * F_{sw}/N_1$.

The fourth feature $\mathbf{f_4}$ is defined as the spectrum $\tilde{Y}(K)$.

Figure 64 shows an example of $\tilde{Y}(K)$ related to the image $Y(m,K)$ of Figure 63b, for $\Delta m = 5$. On the graph, T is highlighted with an horizontal line ($\gamma = 0.05$), and the intersections with $\tilde{Y}(K)$ provide the values of f_2 and f_3, respectively equal to -195 Hz and 142 Hz.

From a physical point of view the features f_1, f_2 and f_3 are an indication of the characteristics of different human gait and can be used to enhance classification performance. The feature $\mathbf{f_4}$ is a Doppler spectrum which represents the modulations induced by each body component that moves with the same periodicity as the step repetition frequency.

f_1, f_2 and f_3 have been used to assess the performance of a Naïve Bayesian classifier. The vector feature $\mathbf{f_4}$ has been used to assess the performance of the shape-similarity-spectrum classifier.

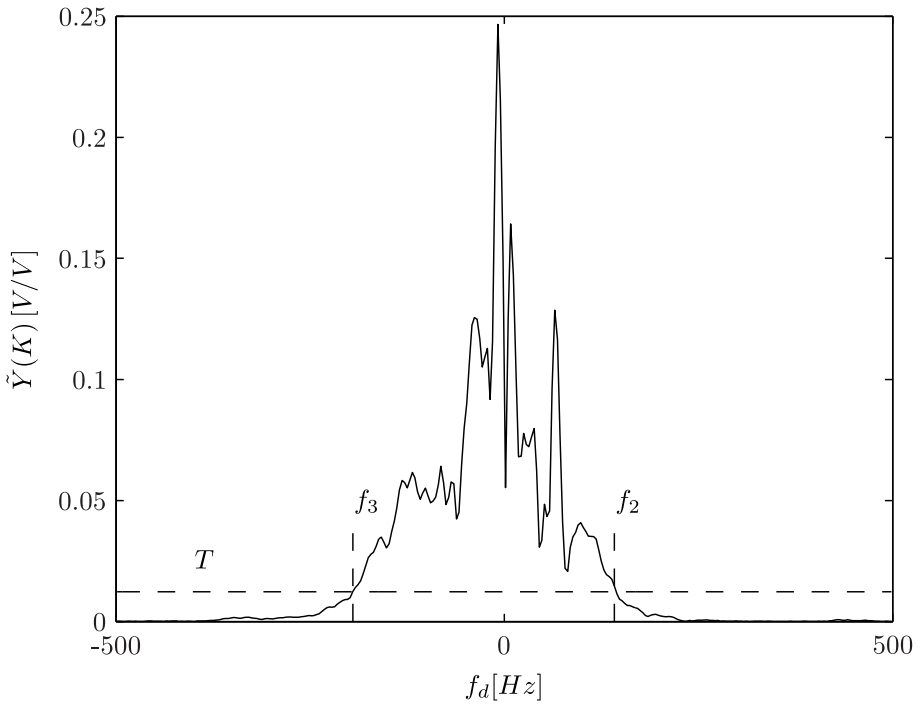

Figure 64: Example of $\tilde{Y}(m, K)$ obtained from the cadence-velocity diagram of Figure 63b.

6.2.2 *Naïve Bayesian classifier*

The vector $\mathbf{f} = (f_1\, f_2\, f_3)^T$ consisting of the features f_1, f_2 and f_3 has been used to assess the performance of a Naïve Bayesian classifier [49]. For each target class T_j , the features f_1, f_2 and f_3 have been assumed to be Gaussian distributed and statistically independent from each other and their joint probability density function (pdf) can be expressed as:

$$f_{\mathbf{f}}(x_1, x_2, x_3/T_j) = \prod_{i=1}^{3} \frac{1}{\sqrt{2\pi\sigma^2_{i/T_j}}} e^{\frac{(x_i - \bar{f}_{i/T_j})^2}{2\sigma^2_{i/T_j}}}, \tag{26}$$

where $\bar{f}_{i/T_j}$ and σ_{i/T_j} are the mean value and the standard deviation of the ith feature for the target T_j, respectively. The mean value and standard deviation of each feature, for each target, have been estimated by using the signatures belonging to the training test. Each feature vector under test $\hat{\mathbf{f}}$ has been assigned to the class T_j that generates the highest value of $f_{\mathbf{f}}(\hat{\mathbf{f}}/T_j)$.

6.2.3 *Shape similarity spectrum classifier*

The feature vector $\mathbf{f_4}$ representing the spectrum shape about the cadence repetition frequency has been considered to be a signature of the target motion under the expectation that acquisitions of the same target would generate spectra with a similar shape. The Pearson linear correlation coefficient has been used as a measure of similarity between acquisitions and it has been selected in order to take into account of potential amplification or scaling effects on the signature. This has been calculated as:

$$\rho_{x,y} = \frac{|\mathrm{cov}(\hat{\mathbf{f}}_4^x, \hat{\mathbf{f}}_4^y)|}{\sigma(\hat{\mathbf{f}}_4^x)\sigma(\hat{\mathbf{f}}_4^y)}, \tag{27}$$

where $\hat{\mathbf{f}}_4^{\mathbf{x}}$ and $\hat{\mathbf{f}}_4^{\mathbf{y}}$ represent the two features to be compared, and $\sigma(\hat{\mathbf{f}}_4^{\mathbf{x}})$ and $\sigma(\hat{\mathbf{f}}_4^{\mathbf{y}})$ their standard deviations. For each target T_j, the mean shape spectrum $\bar{\mathbf{f}}_{\mathbf{4/T_j}}$ has been calculated as:

$$\bar{\mathbf{f}}_{\mathbf{4/T_j}} = \frac{1}{N_{Train}} \sum_{k=1}^{N_{Train}} \mathbf{f}_{\mathbf{4/T_j}}^{\mathbf{k}},$$

where, $\mathbf{f}_{\mathbf{4/T_j}}^{\mathbf{k}}$ is the k-th feature vector of the training set associated with T_j, and N_{Train} is the total number of signatures bundled in the training set. The Pearson linear correlation coefficient has been calculated between each feature vector under test $\hat{\mathbf{f}}_4$ and the mean shape spectrum $\bar{\mathbf{f}}_{\mathbf{4/T_j}}$ of each target T_j as:

$$\rho_j = \frac{\mathrm{cov}(\hat{\mathbf{f}}_4, \bar{\mathbf{f}}_{\mathbf{4/T_j}})}{\sigma(\hat{\mathbf{f}}_4)\,\sigma(\bar{\mathbf{f}}_{\mathbf{4/T_j}})}.$$

Each feature vector under test has been assigned to the class T_j which generates the maximum Pearson linear correlation coefficient.

6.3 FEATURE ANALYSIS AND CLASSIFICATION PERFORMANCE

The features have been extracted from the $N_m = 120$ micro-Doppler signatures collected for each target and for each activity in order to assess the level of class separability and feature robustness. For the analysis, the STFT has been calculated by using 50% overlapping windows which consisted of $Nw = 1350$ samples, leading to a dwell time $T_w = 0.135$ s. The Fourier transform of each window has been calculated on $N_1 = 2\,N_w$ points and the corresponding CVD has been obtained over a number of

Table 8: Reference values for features plot of Figure 65 and 66.

$\bar{f}_{1/T_1}$ [Hz]	$\bar{f}_{2/T_1}$ [Hz]	$\bar{f}_{3/T_1}$ [Hz]
1.90	137.61	-210.85

points $N_2 = 4\,N_b$. The features f_1 has been obtained by setting the parameter $\Delta m = 5$ whilst the features f_2 and f_3 have been obtained by applying the threshold resulting from setting the parameter γ to 5% ($\gamma = 0.05$).
The mean value $\bar{f}_{i/T_j}$ and the standard deviation σ_{i/T_j} of f_1, f_2 and f_3 for each target T_j have been estimated from the data as:

$$\bar{f}_{i/T_j} = \frac{1}{N_m} \sum_{k=1}^{N_m} f^k_{i/T_j}, \tag{28}$$

$$\sigma_{i/T_j} = \sqrt{\frac{1}{N_m} \sum_{k=1}^{N_m} (f^k_{i/T_j} - \bar{f}_{i/T_j})^2}, \tag{29}$$

and have been used to make a comparison between all targets and all activities. Figure65 and Table 9 show the results obtained with signatures produced by the targets walking on the treadmill. Figure 65 shows the mean value and the standard deviation interval of each features f_1, f_2 and f_3, for all the targets $T_1 \ldots T_4$. In the interest of graphical clarity the properties of each feature are plotted with respect to the mean value of the feature f_1 for all targets. The corresponding reference values are given in Table 8.
Results shows that although there may be some overlaps between classes over specific features there are not substantial and simultaneous overlaps across all the features f_1, f_2 and f_3 for each target combination. For example T_1 and T_3 overlap for f_2 and f_3 but are clearly separable in the dimension of f_1. This suggests that the employment of such features in a Naïve Bayesian classifier may lead to promising recognition results. The same analysis has been repeated for the mean Pearson correlation coefficient of $\mathbf{f_4}$. In Table 9, the mean Pearson correlation coefficient among the targets is shown. Table has been obtained by computing $\rho_{x,y}$ for all the combinations of features $\mathbf{f_4}$ extracted within the whole measures database. The mean value and standard deviation of $\rho_{x,y}$ has been then computed for each target pairs. Results show that on the average the mean Pearson correlation coefficient within each class, corresponding to the values on the main diagonal of the resulting matrix, is higher than all the other

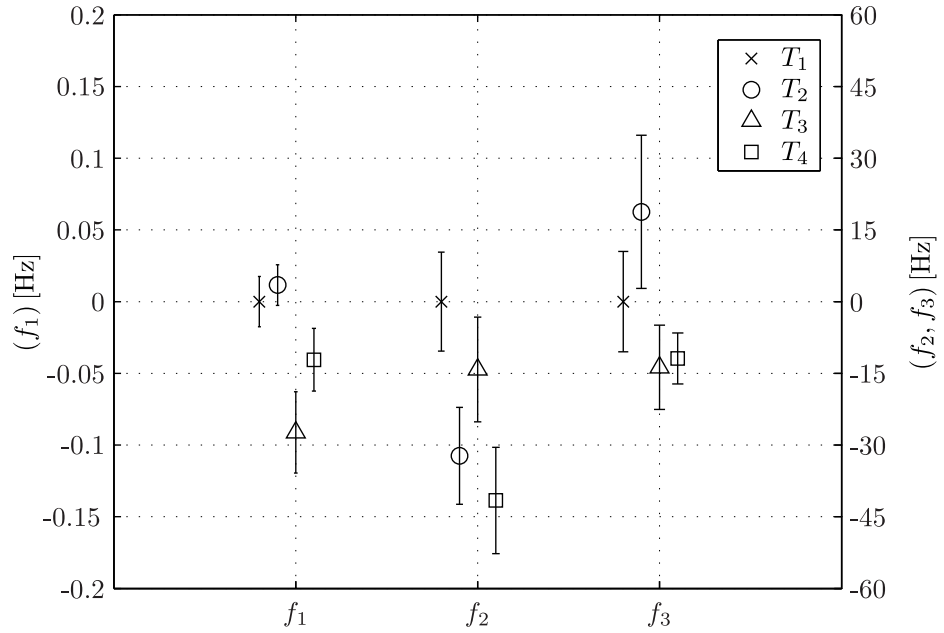

Figure 65: Mean values, standard deviations of features f_1, f_2 and f_3 relatively to walking activity.

Table 9: Mean value and standard deviation of $\rho_{x,y}$ relative to feature f_4, for the walking activity.

$\bar{\rho}_{x,y}$, $\sigma(\rho_{x,y})$	T_1	T_2	T_3	T_4
T_1	0.940, 0.024	0.884, 0.032	0.866, 0.033	0.839, 0.042
T_2	0.884, 0.032	0.960, 0.019	0.901, 0.033	0.865, 0.047
T_3	0.866, 0.033	0.901, 0.033	0.956, 0.018	0.863, 0.036
T_4	0.839, 0.042	0.865, 0.047	0.863, 0.036	0.936, 0.030

elements. The standard deviation values are low enough to ensure the classes separability. This suggest that the shape spectrum classifier may be successfully deployed to classify the targets in the database.
Figure 66 shows the features f_1, f_2 and f_3 for the running activity. This are given with respect to the same values in Table 8 in order to allow a direct comparison with the features obtained for walking activity. Results show that the features f_1 and f_2 are characterised by higher mean values compared to the walking activity, while the mean value of f_3 tends to decrease. The step repetition frequency f_1 of running humans is over 0.5 Hz greater than that of walking humans and the resulting Doppler bandwidth is much larger due to the higher velocity. As for the walking activity there are no simultaneous overlaps between all the three features

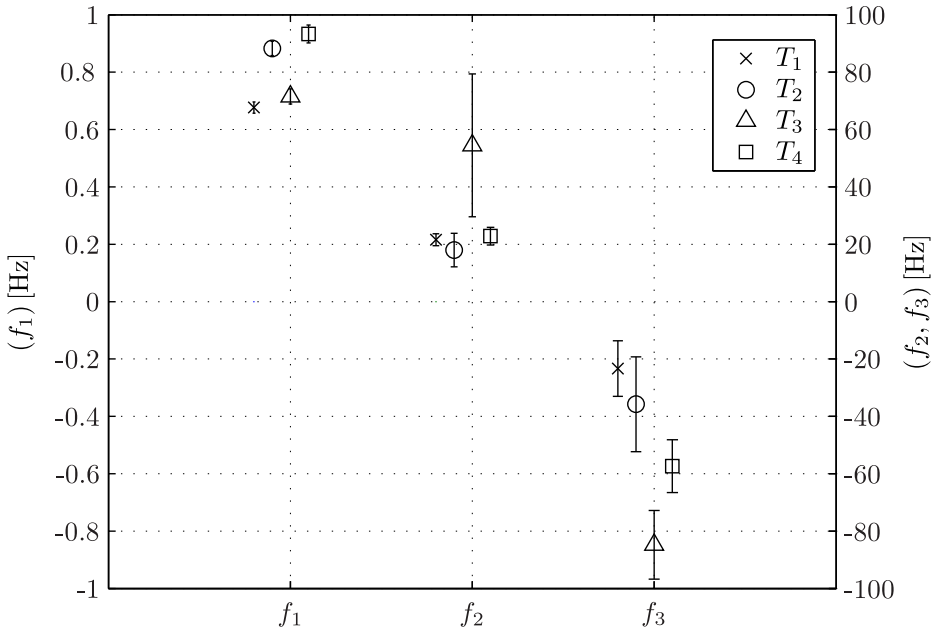

Figure 66: Mean values, standard deviations of features f_1, f_2 and f_3 relatively to running activity.

Table 10: Mean value and standard deviation of $\rho_{x,y}$ relative to feature f_4, for the running activity.

$\bar{\rho}_{x,y}$, $\sigma(\rho_{x,y})$	T_1	T_2	T_3	T_4
T_1	0.951, 0.018	0.790, 0.040	0.881, 0.039	0.913, 0.025
T_2	0.790, 0.040	0.930, 0.030	0.829, 0.045	0.786, 0.042
T_3	0.881, 0.039	0.829, 0.045	0.920, 0.033	0.860, 0.044
T_4	0.913, 0.025	0.786, 0.042	0.860, 0.044	0.939, 0.021

in each class. Table 10 shows a strong correlation of feature $\mathbf{f_4}$ for each class.

An assessment of recognition performance for both classifier and both activities has been carried out and the results are given in Table 11, Table 12, Table 13 and Table 14. The results have been obtained using 30% of the micro-Doppler signatures to train the classifiers ($N_{Train} = 36$) while the remaining $N_{Test} = 84$ signatures have been used to form the test set. Results show that high level recognition performance (over 90%) amongst the four targets can be achieved with both classifiers and for both activities.

In order to assess the effectiveness and robustness of the proposed features the analysis of classification performance has been repeated as a

Table 11: Confusion matrix: walking activity, Naïve Bayesian classifier, training set 30%

Target	1	2	3	4
1	94.15	5.29	0.56	0
2	2.36	97.64	0	0
3	4.71	0.19	90.43	4.67
4	0.26	4.30	11.42	84.02

Table 12: Confusion matrix: walking activity, shape similarity spectrum classifier, training set 30%

Target	1	2	3	4
1	98.96	1.04	0	0
2	0	100	0	0
3	0	0.05	99.95	0
4	0	1.22	0	98.78

function of the window duration T_w and the percentage of overlapping between two consecutive windows $ovlp = \frac{T_{ovlp}}{T_w} = \frac{\Delta l}{N_w}$. For this purpose the parameter T_w has been varied from 0.01 s to 0.185 s with a step of 0.025 s whilst $ovlp$ has been varied from 0.1 to 0.9 with a step of 0.1. Half of the collected signatures have been used to form the training set and the remaining half has been used to test the classifiers. The values of the parameters T_w and $ovlp$ have been chosen so to ensure the extraction of the step repetition frequency f_1 with no ambiguities up to 3 Hz. In order to reduce systematic errors, the training and test sets have been randomly selected 100 times and the resulting average of recognition performance has been recorded.

Figure 67 shows resulting recognition performance as a function of T_w and $ovlp$ for both the running and walking activities and for both the Naïve Bayesian classifier and the shape similarity spectrum classifier. Results show that correct classification success performance varies from a minimum of 30.1% (Figure 67a) to a maximum of 99.6% (Figure 67c). Both the classifiers show a drop in performance when the window duration T_w falls below 0.025 s. Lower values of T_w result in a poorer frequency resolution which leads to less accurate features. For example, the feature vector $\mathbf{f_4}$ becomes shorter and consecutively carries less detailed

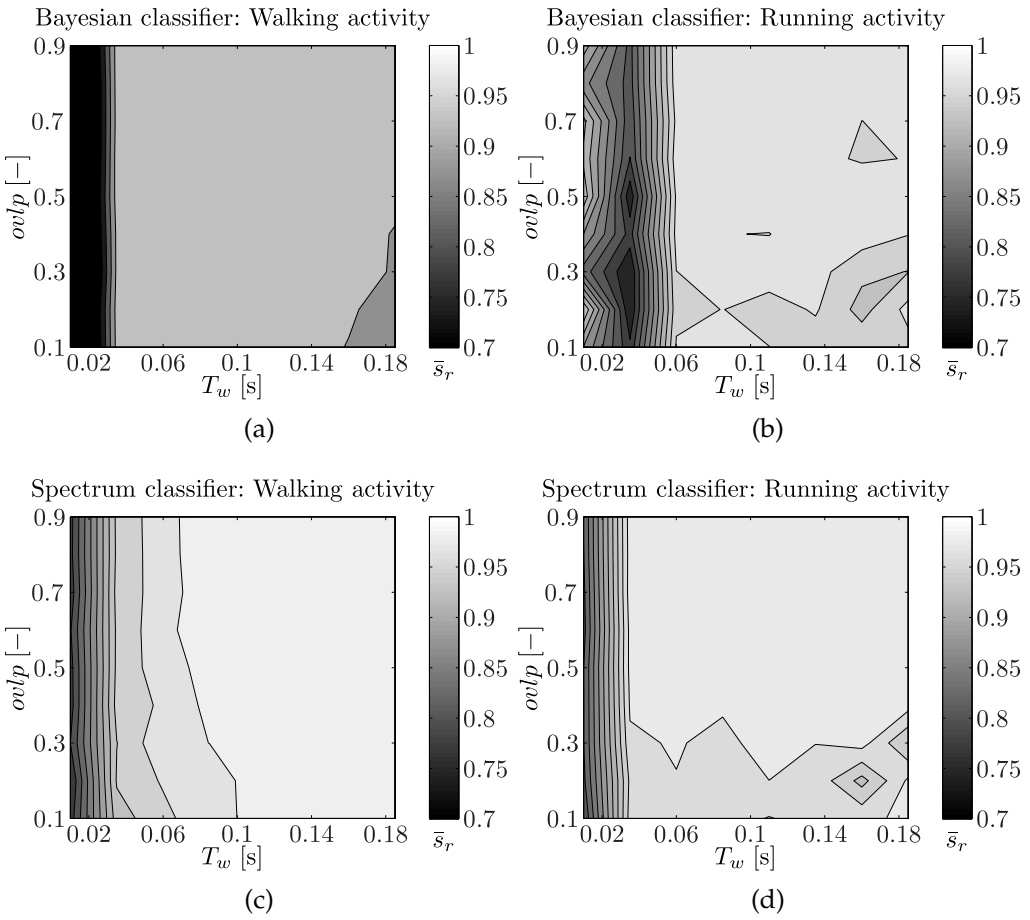

Figure 67: Results of the classification upon the variation of T_w and $ovlp$. The performance are displayed for both running and walking activity, and for both the employed classifiers.

Table 13: Confusion matrix: running activity, Naïve Bayesian classifier, training set 30%

Target	1	2	3	4
1	100	0	0	0
2	0.02	92.96	0.93	6.09
3	3.86	0.15	95.99	0
4	0	6.49	0	93.51

Table 14: Confusion matrix: running activity, shape similarity spectrum classifier, training set 30%

Target	1	2	3	4
1	97.86	0	0.79	1.35
2	0	100	0	0
3	2.58	2.62	93.21	1.59
4	2.20	0	0.01	97.79

information on the target. Overall the shape similarity spectrum classifier shows better performances with respect to the Naïve Bayesian classifier for both the running and walking activity over a wider range of values. The comparison between Figure 67a and Figure 67b shows that the Naïve Bayesian classifier achieves higher classification performance for running humans than walking humans. This is in a agreement with the properties of the features analysed in the previous section according to which the standard deviation of features f_1, f_2 and f_3 are lower for the running activity. Classification performance of the shape similarity spectrum classifier are comparable for both the activities. The plots clearly identify regions on the $(T_w, ovlp)$ plane where classification performance is maximised. In particular, results show that classification performance reaches the highest values when the windows used to generate the STFT are overlapped of at least over 40%. Results also show that for low values of $ovlp$ classification performance tends to drops. Low values of $ovlp$ result in a more granular time resolution of the STFT which is not ideal for targets that move faster. Results show that both classifiers achieve high classification performance for both activities when T_w is in the interval [0.08, 0.185] and $ovlp$ in [0.5, 0.9].

To complete the analysis classification performance has been further as-

sessed as a function of the total number of signatures N_{Train} used to train the classifiers.
Figure 68a and Figure 68b show the results for both the walking and running activity associated to $T_w = 0.135$ and $ovlp = 0.5$ when the number of training windows varied from 48 (10%) to 432 (90%). As for the previous analysis the training set has been randomly selected 100 times and the averaged classification performance has been recorded. Results show that very high recognition performance (over 95 %) can be achieved for both activities. On the average the shape similarity spectrum classifier performs better than the Naïve Bayesian classifier, with a difference in performance reaching up to 12% offset for the walking activities and for the case when a low number of training windows has been used. Overall the level of classification performance does not show a strong dependency on the size of the training set over the selected range of N_{Test}. The shape similarity spectrum classifier shows a nearly flat characteristic for both activities and the Naïve Bayesian classifier shows an increase of the performance of about 5% at the most for the walking activity. This is in agreement with the principles on which the Naïve Bayesian classifier is based upon, for which the training set must be large enough to allow suitable estimates of the mean value and variance of the data for each target. Overall results show that classification performance are robust and that high level performance can be achieved even with a relatively small training set when the proposed features are used.

6.4 ULTRASOUND AND RADAR SYSTEMS COMPARISON

Another experimental trial has been performed in order to compare the ultrasound and radar systems performance. The setup remained the same as the one shown in Figure 62b, but adding an ultrasound system beside the radar device. In Figure 69, a picture of the ultrasound system is shown. It is made of an ultrasound loudspeaker and an high bandwidth microphone (200 kHz). The loudspeaker is driven by a signal generator which outputs a 10 V_{pk-pk} sine wave, at frequency $f_{c,US} = 40$ kHz. The signal transduced through the microphone is forwarded to 20 dB gain pre-amplifier and then acquired by the Handyscope HS4 mobile oscilloscope together with the radar I and Q channels, both digitised at a sampling frequency equal to 100 kHz. Nine people have been asked to walk and run on the electric treadmill, while monitored through both the radar and the ultrasound device. A total number of 10 acquisitions have

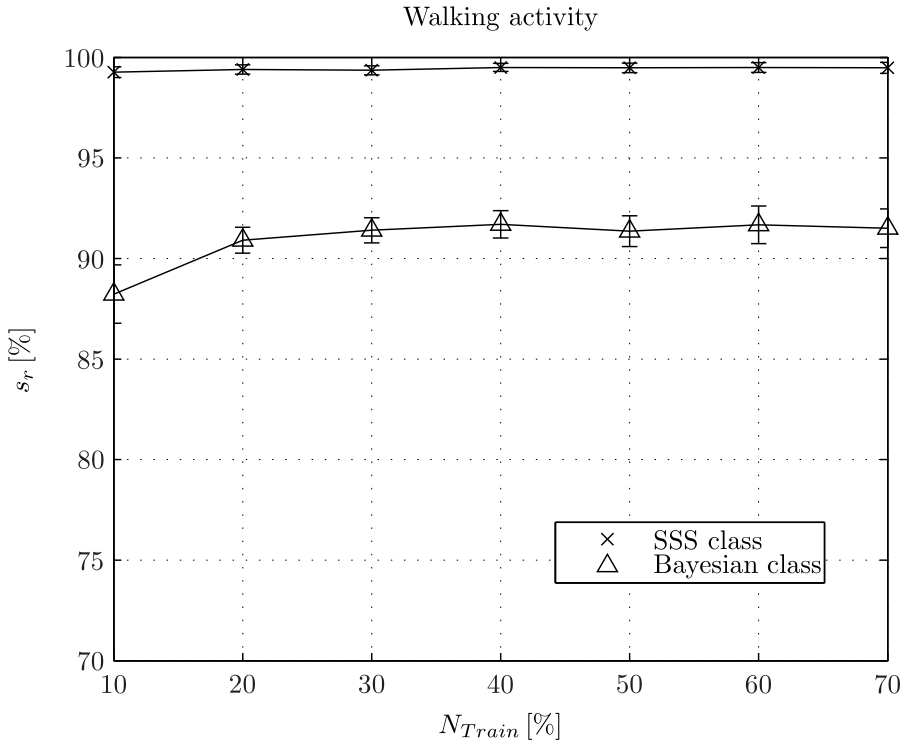

(a)

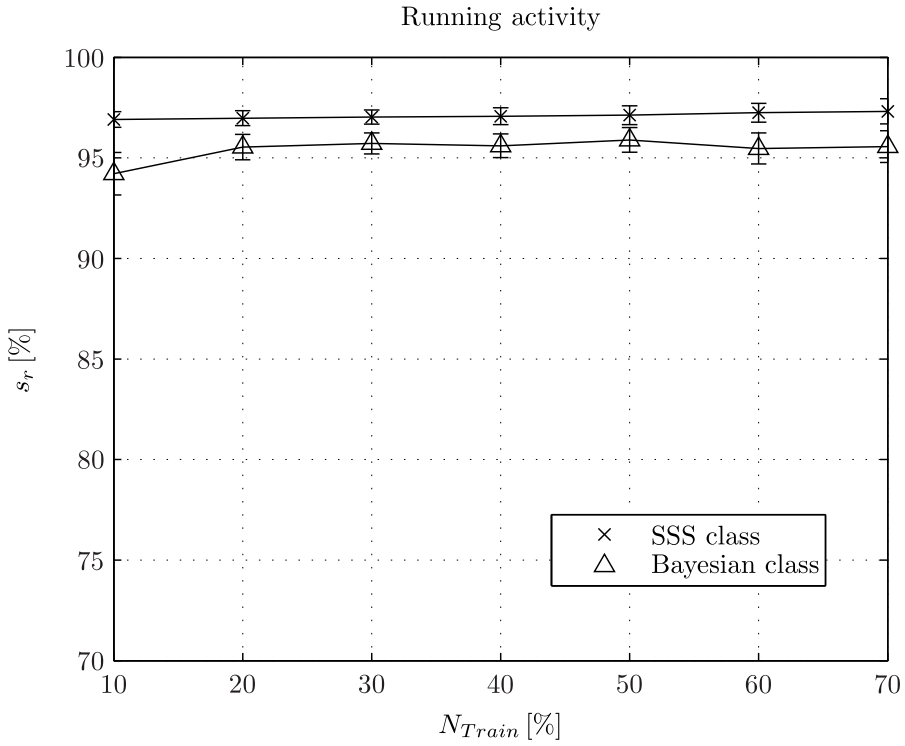

(b)

Figure 68: Analysis of the training set size influence: (a) walking; (b) running.

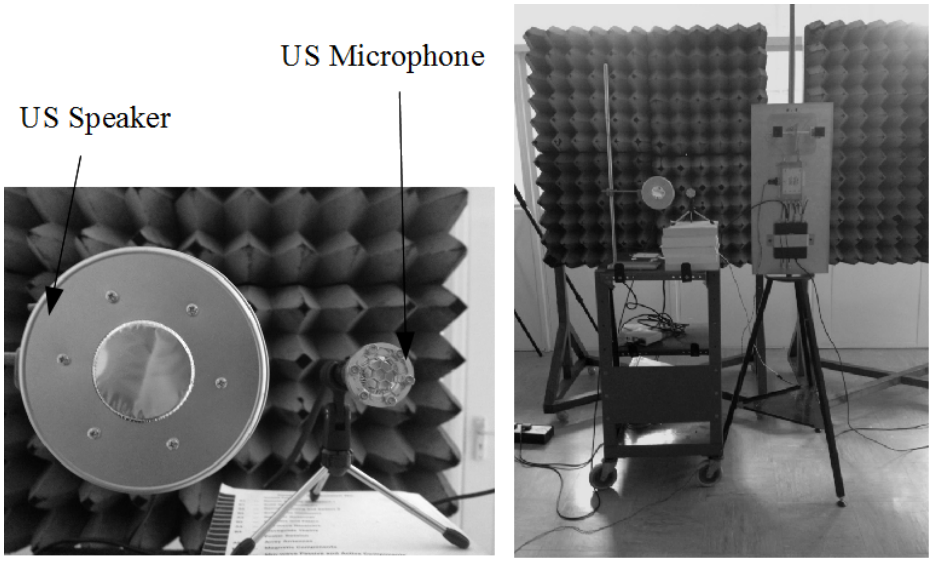

Figure 69: Picture of the measurement devices, a 10 GHz radar and an ultrasound loudspeaker-microphone working at 40 kHz.

been gathered for each activity (walk and run) and for each subject. The oscilloscope has been set to acquire a 10 s signature.

While the processing algorithm of the radar signatures has remained the same as the one described in Section 6.2, some pre-processing of the ultrasound collected signals has been performed. In particular, firstly, the Hilbert transform has been applied to achieve the analytic form of the ultrasound signal, and then the baseband signal has been obtained by a multiplication with $\exp\{-j2\pi f_{c,US}\, t\}$, where t is the time vector and j the imaginary unit.

The spectrogram have been obtained from the acquired signatures, by adopting a 0.15 long time window, and 60% of overlap. The chosen values belong to the optimal intervals previously identified. Then, the features f_1, f_2, f_3 and $\mathbf{f_4}$ have been extracted from both the ultrasound and radar μ-D signatures, as described in Section 6.2.1, and the classification performance has been finally accessed.

In Figure 70 and 71, success rates of the classification task are shown, respectively for the walking and running activity. In the mean, the classification of the running activity results in better performance, of nearly 10%. The Spectrum classifier performs better in all the trials with respect to the Bayesian one. The signatures collected by the ultrasound system are classified with better positive rates, except in the running activity. In this case, the classification of radar signatures shows an higher classifica-

tion rate (referring to the spectrum classifier). Although the difference is very slight, nearly equal to 2%.

The ultrasound system is capable to collect signatures characterized by higher Doppler shifts (US wavelength is nearly 1/3 of the radar wavelength). Hence, the features extraction task is more accurate and consequently the classification performance is higher with respect to the radar signature classification. The radar system is preferable whenever longer distances must be covered. The attenuation of ultrasounds in air is indeed much greater than the radio-frequency wave attenuation.

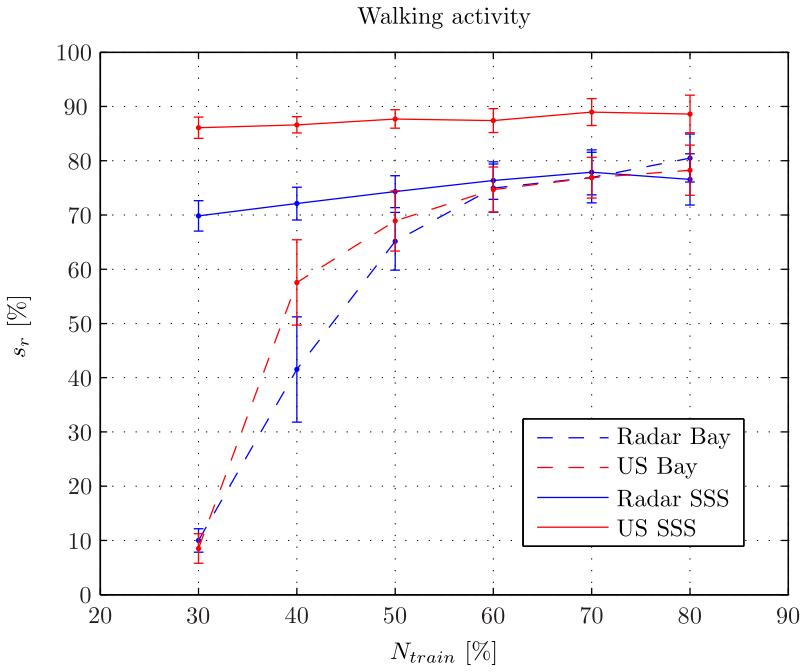

Figure 70: Walking activity: classification results of μ-D signatures gathered by radar and ultrasound device, and employing both the Bayesian and the spectrum classifier.

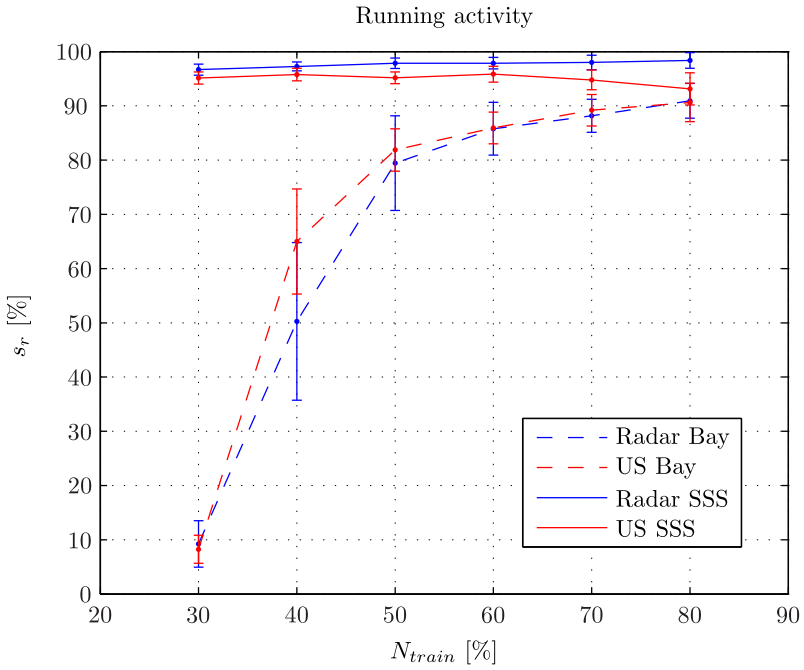

Figure 71: Running activity: classification results of μ-D signatures gathered by radar and ultrasound device, and employing both the Bayesian and the spectrum classifier.

7

CONCLUSIONS

Human detection and identification applications are assuming an increasing importance both within the commercial world and the scientific community. The applications cover a variety of different areas, such as security and surveillance, rescue/recovery of troubled people, medicine and gait analysis. Among the plenty of employed technologies, over the last few years, radar and ultrasound Doppler systems are gaining an increasing interest in human detection/identification scenario.

In this dissertation, the classification of radar and ultrasound human micro-Doppler signatures have been carried out, showing excellent performances in terms of positive classification rates. The first part of the work focuses on the development of a general measurement approach for human motion detection/identification. The designed approach is technology-independent and can be used in a wide variety of scenarios, from the estimation of some human basic movements to the identification of the human target identity. With the aim to prove the approach effectiveness, a 40 kHz ultrasound Doppler system has been designed and manufactured. It is composed of an ultrasound transmitter-receiver couple, employed to illuminate the target and collect the backscattering micro-Doppler signature. The UDS has been then characterised by a suitably build measurement setup. The tangential speed of a rotating sphere used as reference target has been estimated in various measurement setup conditions, yielding a mean error of 0.25 m/s (max tangential speed 11 m/s) and a standard deviation of the error equal to 0.15 m/s.

The UDS has been then tested to gather and analyse μ-D signatures relative to walking human targets. The acquired signatures have been displayed in the form of spectrograms, to be compared with the measures obtained through a motion capture system. The latter one is capable to accurately measure the position of a reflective markers set attached to the test human target, by employing a six-cameras system. The comparison has allowed to obtain a lot of information about the human-induced ultrasound μ-D signature. In particular, in the case of human gait analyses, the obtained signatures show a set of merged trajectories due the body parts motion. Some body parts can be highlighted within the signature:

(i) the arms and feet motions are very distinguishable at the extremities of the signature for their higher speed with respect to the other body parts; (ii) the thorax motion is particularly evident because it causes a strong ultrasound reflection due to the large surface; (iii) other body parts like knees, and elbows are instead merged, and difficult to access singularly.

In the second part of the dissertation, the UDS (40 kHz) has been employed to collect μ-D signatures of ten people walking on an electric treadmill, with the aim to classify the targets identity. The signatures have been processed in order to extract a novel set of features that synthetically describe the particular human. The features have been then forwarded to three different classifiers, obtaining successfully rates up to 66.4% and 83.9% with a Bayesian and a spectrum classifier respectively. Even better results have been achieved by combining the use of the two classifiers, up to successful rates of 88.9%.

The measurement approach has been then applied in the radio-frequency domain. The μ-D signatures of four different human targets have been collected by using a 10 GHz CW mono-static radar system. Measures have been performed for both walking and running gait and then separate analyses and classifications have been executed. Again, the classification of targets has been performance using two different classifiers, a Naïve Bayesian classifier, and the shape similarity spectrum classifier. The optimal time window duration and overlap ranges have been found by an iterative classification procedure. Classification success rate up to 99.6% can be achieved, when classifying the target relatively to the walking activity. The comparison between the classifiers shows that the shape similarity spectrum classifier can achieve better performances with respect to the Naïve Bayesian one, up to 12% higher. Moreover, the shape similarity spectrum classifier requires a lower amount of training measures.

Another experimental trial has been performed in order to compare the ultrasound and radar systems performance. Nine people have been asked to walk and run on the electric treadmill, while monitored through both the radar (10 GHz) and the ultrasound device (40 kHz). The signatures have been processed and classified through the previously developed algorithm. In the mean, the classification of the running activity results in better performance, of nearly 10%. The Spectrum classifier performs better in all the trials with respect to the Bayesian one. The signatures collected by the ultrasound system are classified with better positive rates, up to 16% difference. In fact, the ultrasound system is ca-

pable to collect signatures characterized by higher Doppler shifts (US wavelength is nearly 1/3 of the radar wavelength). Hence, the features extraction task is more accurate and consequently the classification performance is higher with respect to the radar signature classification. The radar system is preferable whenever longer distances must be covered. The attenuation of ultrasounds in air is indeed much greater than the radio-frequency wave attenuation.

The obtained results are promising and show the effectiveness of the adopted system and measurement approach for applications in the field of human motion recognition. Further research can be performed in order to enlarge the database of reference measures, study different target activities/behaviours, improve the use of classifiers, and apply the system for the analysis of some particular classes of people, e.g. diseased, armed people, kids, or old people.

APPENDIX A: DATASHEETS

A.1 MURATA MA40S4S/R

S15E.pdf
08.10.31

Ultrasonic Sensor

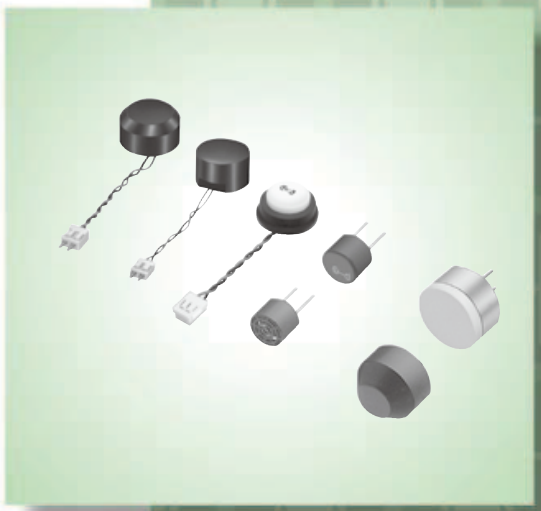

Application Manual

muRata Innovator in Electronics

Murata
Manufacturing Co., Ltd.

Cat.No.S15E-5

1

1 Characteristics of Ultrasonic Waves

Ultrasonic waves are sounds which cannot be heard by humans and are normally, frequencies of above 20kHz. The basic characterisitics of ultrasonic waves are explained below.

1. Wavelength and Radiation

Velocity of wave propagation is expressed by multiplication of frequency and wavelength. The velocity of an electromagnetic wave is 3×10^8m/s, but the velocity of sound wave propagation in air is as slow as about 344m/s (at 20°C). At these slower velocities, wavelengths are short, meaning that higher resolution of distance and direction can be obtained.
Because of the higher resolution, it is possible to get higher measurement made large accuracy. The surface dimension of the ultrasonic device can be easily to obtain accurate radi-ation.

2. Reflection

In order to detect the presence of an object, ultrasonic waves are reflected on objects.
Because metal, wood, concrete, glass, rubber and paper, etc. reflect approximately 100% of ultrasonic waves, these objects can be easily detected.
Cloth, cotton, wool, etc. are difficult to detect because they absorb ultrasonic waves. It may often be difficult, also, to detect objects having large surface undulation, because of irregular reflection.

3. Effects of Temperature

Velocity of sound wave propagation "c" is expressed by the following formula.
c=331.5+0.607t (m/s) where t=temperature (°C)
That is as sound velocity varies according to circumferential temperature, it is necessary to verify the temperature at all times to measure the distance to the object accurately.

4. Attenuation

The strength of ultrasonic waves propagated into the air attenuate proportionally with distance. This is caused by diffusion loss on a spherical surface due to diffraction phenomenon and absorption loss, that energy is absorbed by medium.
As shown in Fig.1, the higher the frequency of the ultrasonic wave, the bigger the attenuation rate and the shorter the distance the wave reaches.

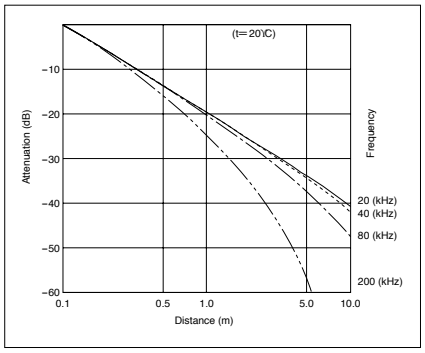

Fig. 1 Attenuation Characteristics of Sound Pressure by Distance

2 Construction and Operation Principles

When voltage is applied to piezoelectric ceramics, mechanical distortion is generated according to the voltage and frequency.
On the other hand, when vibration is applied to piezoelectric ceramics, an electric charge is produced.
By applying this principle, when an electric signal is added to a vibrator, constructed of 2 sheets of piezoelectric ceramics or a sheet of piezoelectric ceramics and a metal sheet, an electric signal is radiated by flexure vibration. As a reverse effect, when an ultrasonic vibration is added to the vibrator, an electric signal is produced.
Because of these effects, piezoelectric ceramics are utilized as ultrasonic sensors.

1. Open Structure Type Ultrasonic Sensors

As shown in the diagram of an ultrasonic sensor (Fig. 2), a multiple vibrator is fixed elastically to the base.
This multiple vibrator is a combination of a resonator and a vibrator which is composed of a metal sheet and a piezoelectric ceramics sheet. The resonator is conical in order to efficiently radiate the ultrasonic waves generated by the vibration and also in order to effectively concentrate the ultrasonic waves at the central part of the vibrator.
Fig. 3 shows a finite element method simulation of the vibration of the multiple vibrators.

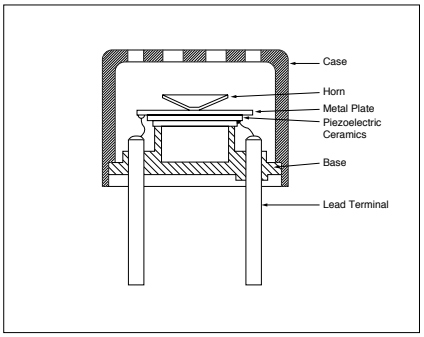

Fig.2 Construction of Open Structure Type Ultrasonic Sensor

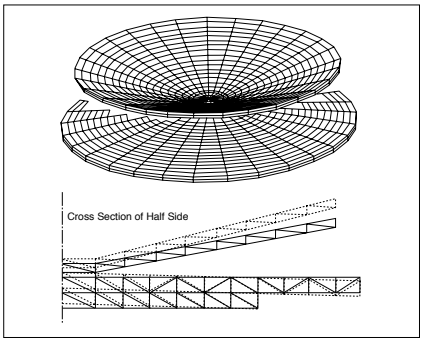

Fig.3 Simulation of Vibration

2 Construction and Operation Principles

2. Enclosed type Ultrasonic Sensor

Ultrasonic sensors for outdoors use are sealed to protect them from dew, rain and dust.
Piezoelectric ceramics are attached to the top inside of the metal case. The entrance of the case is covered with resin. (See Fig. 4.)

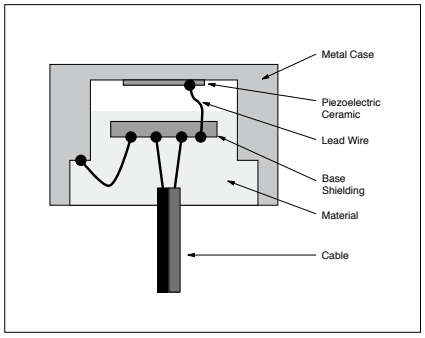

Fig. 4 Construction of Enclosed Type Ultrasonic Sensor

3. High Frequency Ultrasonic Sensors

For use in industrial robots, accuracy as precise as 1mm and acute radiation are required. By flexure vibration of the conventional vibrator, no practical characteristics can be obtained in frequencies higher than 70kHz and, therefore, vertical thickness vibration mode of piezoelectric ceramics is utilized for detection in high frequency.
In this case, the matching of acoustic impedances of the piezoelectric ceramics and air becomes important.
Acoustic impedance of piezoelectric ceramics is 2.6×10.7kg/m^{2}s, while that of air is 4.3×10.2kg/m^{2}s.
This difference of 5 powers causes large loss on the vibra-tion radiating surface of the piezoelectric ceramics.
Matching the acoustic impedances with air is performed by bonding a special material to the piezoelectric ceramics as an acoustic matching layer.
This construction enables the ultrasonic sensor to work in frequencies of up to several hundred kHz.

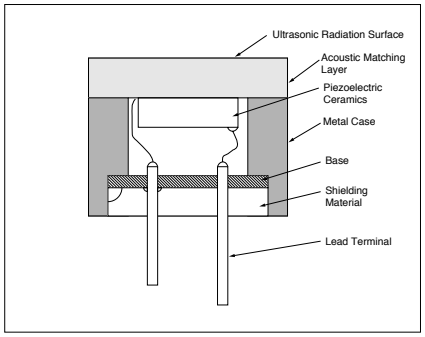

Fig. 5 Construction of High Frequency Ultrasonic Sensors

3 Electrical Characteristics

1. Sound Pressure Characteristics

Sound pressure level (S.P.L.) is unit indicating the volume of sound and is expressed by the following formula.

$$\text{S.P.L.}=20\log\frac{P}{Po}\ (\text{dB})$$

where "P" is Sensor sound pressure (Pa) and "Po" is reference sound pressure (20μPa).
Fig.6 shows a sound pressure measuring circuit.

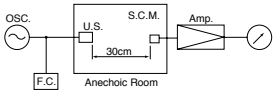

U.S.	: Ultrasonic Sensor	
S.C.M.	: Standard Capacitor Microphone	(Brüel & Kjær 4135)
Amp.	: Amplifier	(Brüel & Kjær 2610)
Input Voltage	: 10Vrms, Sine wave	
F.C.	: Frequency Counter	0dB=20μPa

Fig. 6 Sound Pressure Measuring Circuit

2. Sencitivity Characteristics

Sensitivity is the unit indicating the sound receiving level and is expressed by the following formula.

$$\text{Sensitivity}=20\log\frac{S}{So}\ (\text{dB})$$

where "S" is Sensor voltage (V) and "So" is reference sound pressure (V/Pa) .
Fig.7 shows a sensitivity measuring circuit. The 3.9kΩ resistor connected with the electrode terminal of the sensor is used to avoid the influence of outside noise.

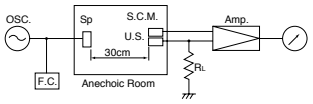

RL	: 3.9kΩ	
U.S.	: Ultrasonic Sensor	
S.C.M.	: Standard Capacitor Microphone	(Brüel & Kjær 4135)
Amp.	: Amplifier	(Brüel & Kjær 2610)
OSC.	: Oscillator	
Sp.	: Tweeter	
F.C.	: Frequency Counter	0dB=10V/Pa

Fig. 7 Sensitivity Measuring Circuit

3. Radiation

The ultrasonic sensor is installed on a table. Then, the relationship between angle and sound pressure (sensitivity) is measured.
In order to express radiation precisely, the angle in which the sound pressure (sensitivity) level attenuates by 6dB compared with the front is called the half attenuation angle with an expression of $\theta^{1/2}$.

3 Electrical Characteristics

4. Ratings

The ratings and dimensions of representative types of these ultrasonic sensors appear in Table 1. Also frequency characteristics of sensitivity and sound pressure are shown in Figs. 8 and 9 and their radiation characteristics Figs. 10 and 11.

Item \ Part Number	MA40S4R/S
Construction	Open structure type
Using Method	Receiver and Transmitter (Dual use) type
Nominal Frequency (kHz)	40
Overall Sensitivity (dB)	–
Sensitivity (dB)	–63±3
Sound Pressure (dB)	120±3
Directivity (deg)	80
Capacitance (pF)	2550±20%
Operating Temperature Range (°C)	–40 - +85
Detectable Range (m)	0.2 - 4
Dimension (mm)	ø9.9×7.1h
Weight (g)	0.7
Max. Input Voltage	20 Vp-p Square wave 40kHz

Item \ Part Number	MA40E7R/S	MA40E8-2	MA40MF14-5B
Construction	Water proof type		
Using Method	Receiver and Transmitter type	Combined use type	
Nominal Frequency (kHz)	40		
Overall Sensitivity (dB)	–		
Sensitivity (dB)	–74 min.	–85 min.	–87 min.
Sound Pressure (dB)	106 min.		103 min.
Directivity (deg)	100	75	100×50
Capacitance (pF)	2200±20%	2800	4400
Operating Temperature Range (°C)	–30 - +85		–40 - +85
Detectable Range (m)	0.2 - 3	0.2 - 1.5	
Dimension (mm)	ø18×12h	ø14×8h	ø14×9h
Weight (g)	4.5	2.4	
Max. Input Voltage	100 Vp-p Square waves 40kHz Pulse width 0.4 ms Interval 100 ms	160 Vp-p Square waves 40kHz Pulse width 0.8ms Interval 60 ms	

• Distance : 30cm, Sensitivity : 0dB=10V/Pa, Sound pressure Level : 0dB=20μPa.
• The sensor can be used in the operating temperature range.
Please refer to the individual specification for the temperature drift of Sensitivity/Sound pressure level or environmental characteristics in that temperature range.
• Directivity, and Detectable Range typical is value. It can be changed by application circuit and fixing method of the sensor.

Electrical Characteristics 3

Item \ Part Number	MA80A1	MA200A1	MA400A1
Construction	High frequency type		
Using Method	Combined use type		
Center Frequency (kHz)	75±5	200±10	400±20
Overall Sensitivity (dB)	-47 min. 0dB=18Vpp (at 50 cm)	-54 min. 0dB=18Vpp (at 20 cm)	-74 min. 0dB=18Vpp (at 10 cm)
Directivity (deg)	7		
Operating Temperature Range (°C)	-10 - +60	-30 - +60	
Detectable Range (m)	0.5 - 5	0.2 - 1	0.06 - 0.3
Dimension (mm)	ø47×24.5h	ø19×10.6h	ø11×10.5h
Weight (g)	93	6	2
Max. Input Voltage	120 Vp-p Square waves 75kHz Pulse width 600µs Interval 50 ms	120 Vp-p Square waves 200kHz Pulse width 250µs Interval 20 ms	120 Vp-p Square waves 400kHz Pulse width 125µs Interval 10 ms

• The sensor can be used in the operating temperature range. Please refer to the individual specification for the temperature drift of Sensitivity/ Sound pressure level or environmental characteristics in that temperature range.
• Directivity, and Detectable Range is typical value. It can be changed by application circuit and fixing method of the sensor.

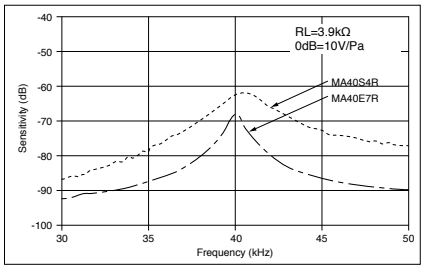

Fig. 8 Sensitivity

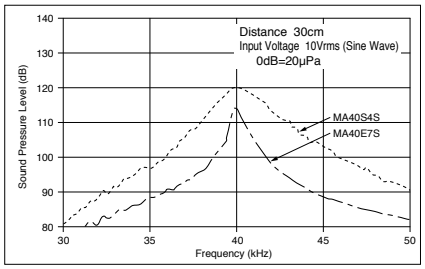

Fig. 9 Sound Pressure

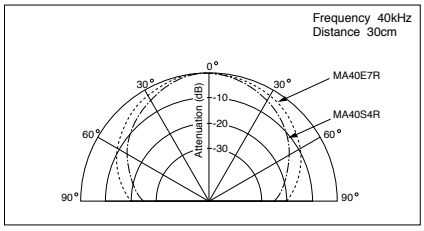

Fig. 10 Radiation Characteristics (Receiver)

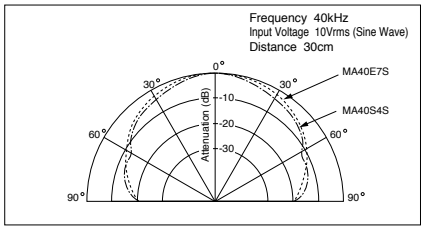

Fig. 11 Radiation Characteristics (Transmitter)

4 Applications

1. Examples of Applications

Ultrasonic sensors are utilized for many purposes such as measurement applications etc.
For examples of these applications, please refer to the examples in Table 2 and the explanations as follows.
Level detection of continuous wave signals (Example 1) is used for counting machines and approximate switches due to the simple circuit construction of these devices.
Example 2 is used in devices such as automatic doors where the environment is very changeable. The system is arranged so that the instrument may actuate only when a certain number of reflected pulses is detected. And example 2 is also used for measuring distance to an object, such as the back up sensors of cars.
Example 3 is an application utilizing the phenomenon by which the Doppler effect produces a modulated signal as an object moves closer or farther away. This is often used for intruder alarm systems.
Example 4 is an application utilizing the change of sound velocity according to the density and the flow speed of a gas.
Example 5 is a method used to count the number of Karman vortex generated against flow speed and utilize phenomena that ultrasonic signals level are reduced as Karman vortex passes into the sensor.

No.	Function Method	Performance Principle (S: transmitter, R: receiver)	Applications
1	Detection of Signal level of continuous wave	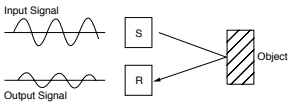	Counting instruments Access switches Parking meters
2	Measurement of pulse reflection time	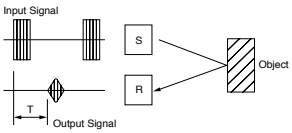	Automatic doors Level gauges Automatic change-overs of traffic signals Back sonars of automobiles
3	Utilization of Doppler effect	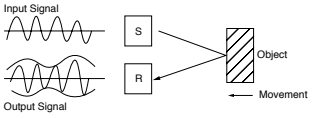	Intruder alarm systems
4	Measurement of direct propagation time	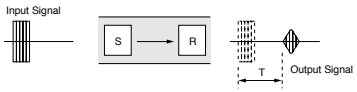	Densitometers Flowmeters
5	Measurement of Karman vortex	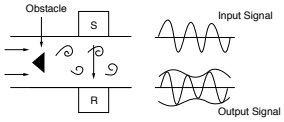	Flowmeters

Table 2 Application Examples

A.2 ON SEMICONDUCTOR MC33178

MC33078, MC33079

Dual/Quad Low Noise Operational Amplifiers

The MC33078/9 series is a family of high quality monolithic amplifiers employing Bipolar technology with innovative high performance concepts for quality audio and data signal processing applications. This family incorporates the use of high frequency PNP input transistors to produce amplifiers exhibiting low input voltage noise with high gain bandwidth product and slew rate. The all NPN output stage exhibits no deadband crossover distortion, large output voltage swing, excellent phase and gain margins, low open loop high frequency output impedance and symmetrical source and sink AC frequency performance.

The MC33078/9 family offers both dual and quad amplifier versions, tested over the automotive temperature range and available in the plastic DIP and SOIC packages (P and D suffixes).

- Dual Supply Operation: ±5.0 V to ±18 V
- Low Voltage Noise: 4.5 nV/$\sqrt{\text{Hz}}$
- Low Input Offset Voltage: 0.15 mV
- Low T.C. of Input Offset Voltage: 2.0 μV/°C
- Low Total Harmonic Distortion: 0.002%
- High Gain Bandwidth Product: 16 MHz
- High Slew Rate: 7.0 V/μs
- High Open Loop AC Gain: 800 @ 20 kHz
- Excellent Frequency Stability
- Large Output Voltage Swing: +14.1 V/ –14.6 V
- ESD Diodes Provided on the Inputs

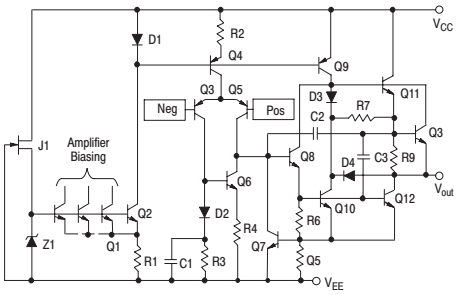

Figure 1. Representative Schematic Diagram
(Each Amplifier)

ON Semiconductor™

http://onsemi.com

MARKING DIAGRAMS

DUAL

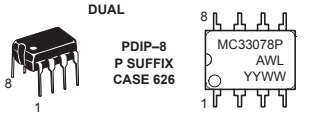

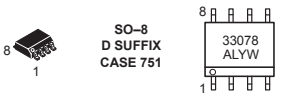

QUAD

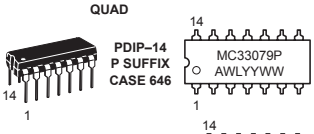

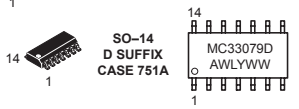

A = Assembly Location
WL, L = Wafer Lot
YY, Y = Year
WW, W = Work Week

ORDERING INFORMATION

Device	Package	Shipping
MC33078D	SO–8	98 Units/Rail
MC33078DR2	SO–8	2500 Tape & Reel
MC33078P	PDIP–8	50 Units/Rail
MC33079D	SO–14	55 Units/Rail
MC33079DR2	SO–14	2500 Tape & Reel
MC33079P	PDIP–14	25 Units/Rail

February, 2001 – Rev. 1

Publication Order Number:
MC33078/D

PIN CONNECTIONS

DUAL

CASE 626/751

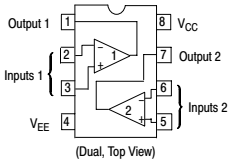

QUAD

CASE 646/751A

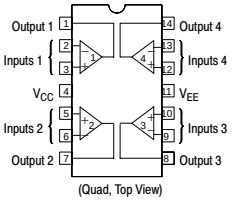

MAXIMUM RATINGS

Rating	Symbol	Value	Unit
Supply Voltage (V_{CC} to V_{EE})	V_S	+36	V
Input Differential Voltage Range	V_{IDR}	Note 1.	V
Input Voltage Range	V_{IR}	Note 1.	V
Output Short Circuit Duration (Note 2.)	t_{SC}	Indefinite	sec
Maximum Junction Temperature	T_J	+150	°C
Storage Temperature	T_{stg}	–60 to +150	°C
Maximum Power Dissipation	P_D	Note 2.	mW

1. Either or both input voltages must not exceed the magnitude of V_{CC} or V_{EE}.
2. Power dissipation must be considered to ensure maximum junction temperature (T_J) is not exceeded (see Figure 2).

DC ELECTRICAL CHARACTERISTICS (V_{CC} = +15 V, V_{EE} = –15 V, T_A = 25°C, unless otherwise noted.)

Characteristics	Symbol	Min	Typ	Max	Unit
Input Offset Voltage (R_S = 10 Ω, V_{CM} = 0 V, V_O = 0 V) (MC33078) T_A = +25°C T_A = –40° to +85°C (MC33079) T_A = +25°C T_A = –40° to +85°C	$\|V_{IO}\|$	 – – – –	 0.15 – 0.15 –	 2.0 3.0 2.5 3.5	mV
Average Temperature Coefficient of Input Offset Voltage R_S = 10 Ω, V_{CM} = 0 V, V_O = 0 V, T_A = T_{low} to T_{high}	$\Delta V_{IO}/\Delta T$	–	2.0	–	μV/°C
Input Bias Current (V_{CM} = 0 V, V_O = 0 V) T_A = +25°C T_A = –40° to +85°C	I_{IB}	 – –	 300 –	 750 800	nA
Input Offset Current (V_{CM} = 0 V, V_O = 0 V) T_A = +25°C T_A = –40° to +85°C	I_{IO}	 – –	 25 –	 150 175	nA
Common Mode Input Voltage Range (ΔV_{IO} = 5.0 mV, V_O = 0 V)	V_{ICR}	±13	±14	–	V
Large Signal Voltage Gain (V_O = ±10 V, R_L = 2.0 kΩ) T_A = +25°C T_A = –40° to +85°C	A_{VOL}	 90 85	 110 –	 – –	dB
Output Voltage Swing (V_{ID} = ±1.0V) R_L = 600 Ω R_L = 600 Ω R_L = 2.0 kΩ R_L = 2.0 kΩ R_L = 10 kΩ R_L = 10 kΩ	 V_O+ V_O– V_O+ V_O– V_O+ V_O–	 – – +13.2 – +13.5 –	 +10.7 –11.9 +13.8 –13.7 +14.1 –14.6	 – – – –13.2 – –14	V
Common Mode Rejection (V_{in} = ±13V)	CMR	80	100	–	dB
Power Supply Rejection (Note 3.) V_{CC}/V_{EE} = +15 V/ –15 V to +5.0 V/ –5.0 V	PSR	80	105	–	dB
Output Short Circuit Current (V_{ID} = 1.0 V, Output to Ground) Source Sink	I_{SC}	 +15 –20	 +29 –37	 – –	mA
Power Supply Current (V_O = 0 V, All Amplifiers) (MC33078) T_A = +25°C T_A = –40° to +85°C (MC33079) T_A = +25°C T_A = –40° to +85°C	I_D	 – – – –	 4.1 – 8.4 –	 5.0 5.5 10 11	mA

3. Measured with V_{CC} and V_{EE} differentially varied simultaneously.

AC ELECTRICAL CHARACTERISTICS (V_{CC} = +15 V, V_{EE} = –15 V, T_A = 25°C, unless otherwise noted.)

Characteristics	Symbol	Min	Typ	Max	Unit
Slew Rate (V_{in} = –10 V to +10 V, R_L = 2.0 kΩ, C_L = 100 pF A_V = +1.0)	SR	5.0	7.0	–	V/μs
Gain Bandwidth Product (f = 100 kHz)	GBW	10	16	–	MHz
Unity Gain Bandwidth (Open Loop)	BW	–	9.0	–	MHz
Gain Margin (R_L = 2.0 kΩ) C_L = 0 pF C_L = 100 pF	A_m	 – –	 –11 –6.0	 – –	dB
Phase Margin (R_L = 2.0 kΩ) C_L = 0 pF C_L = 100 pF	ϕ_m	 – –	 55 40	 – –	Deg
Channel Separation (f = 20 Hz to 20 kHz)	CS	–	–120	–	dB
Power Bandwidth (V_O = 27 V_{pp}, R_L = 2.0 kΩ, THD ≤ 1.0%)	BW_p	–	120	–	kHz
Total Harmonic Distortion (R_L = 2.0 kΩ, f = 20 Hz to 20 kHz, V_O = 3.0 V_{rms}, A_V = +1.0)	THD	–	0.002	–	%
Open Loop Output Impedance (V_O = 0 V, f = 9.0 MHz)	$\|Z_O\|$	–	37	–	Ω
Differential Input Resistance (V_{CM} = 0 V)	R_{in}	–	175	–	kΩ
Differential Input Capacitance (V_{CM} = 0 V)	C_{in}	–	12	–	pF
Equivalent Input Noise Voltage (R_S = 100 Ω, f = 1.0 kHz)	e_n	–	4.5	–	nV/$\sqrt{Hz}$
Equivalent Input Noise Current (f = 1.0 kHz)	i_n	–	0.5	–	pA/$\sqrt{Hz}$

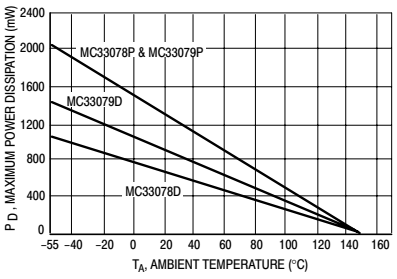

Figure 2. Maximum Power Dissipation versus Temperature

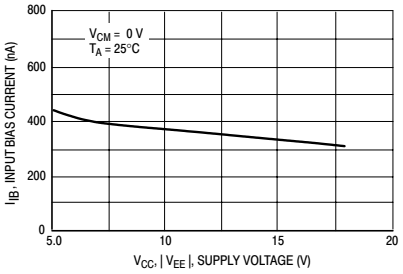

Figure 3. Input Bias Current versus Supply Voltage

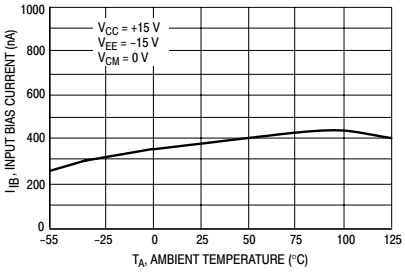

Figure 4. Input Bias Current versus Temperature

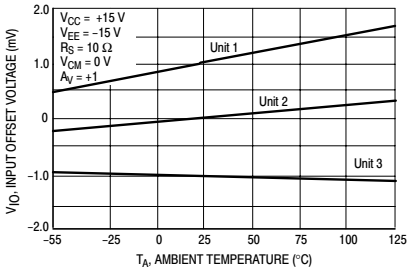

Figure 5. Input Offset Voltage versus Temperature

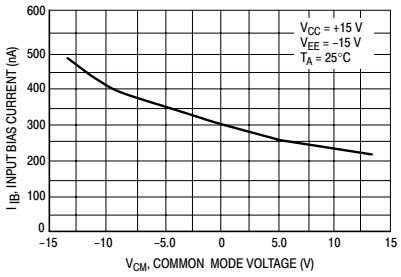

Figure 6. Input Bias Current versus Common Mode Voltage

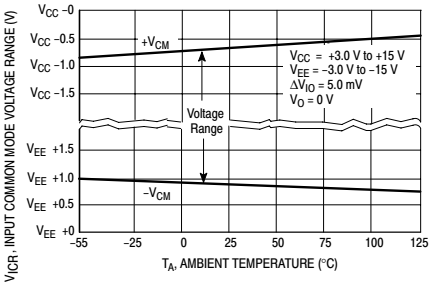

Figure 7. Input Common Mode Voltage Range versus Temperature

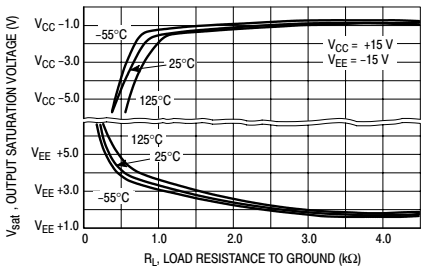

Figure 8. Output Saturation Voltage versus Load Resistance to Ground

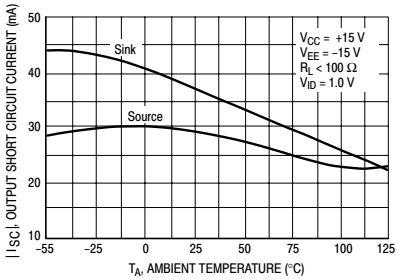

Figure 9. Output Short Circuit Current versus Temperature

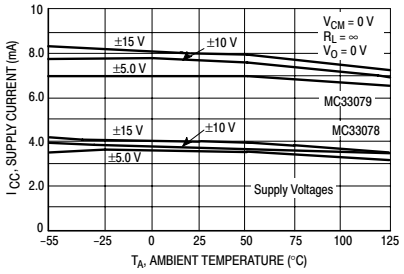

Figure 10. Supply Current versus Temperature

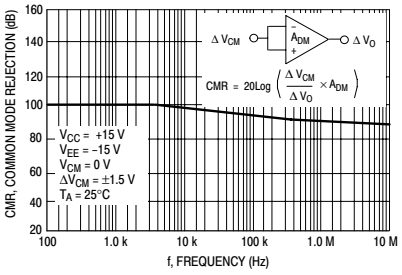

Figure 11. Common Mode Rejection versus Frequency

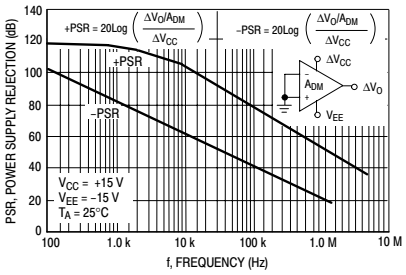

Figure 12. Power Supply Rejection versus Frequency

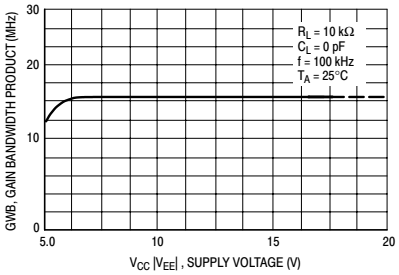

Figure 13. Gain Bandwidth Product versus Supply Voltage

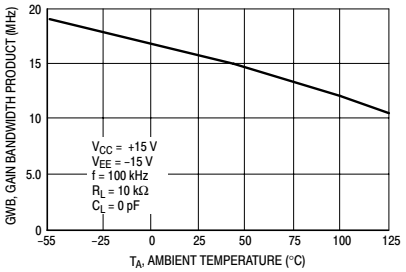

Figure 14. Gain Bandwidth Product versus Temperature

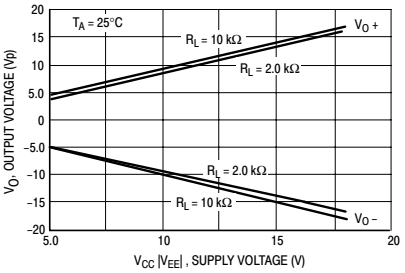

Figure 15. Maximum Output Voltage versus Supply Voltage

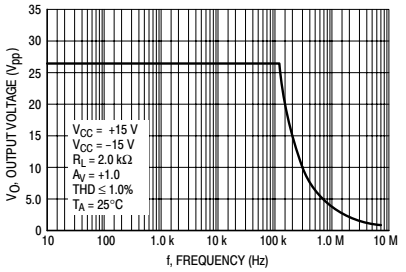

Figure 16. Output Voltage versus Frequency

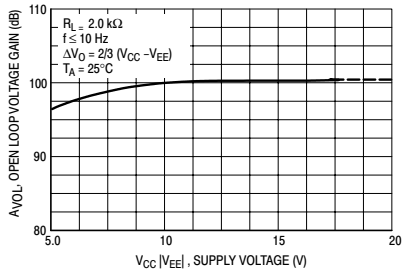

Figure 17. Open Loop Voltage Gain versus Supply Voltage

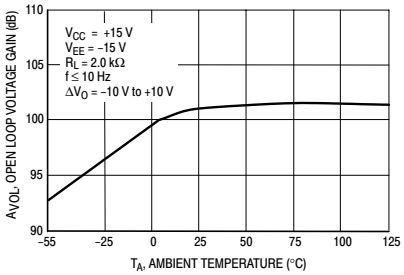

Figure 18. Open Loop Voltage Gain versus Temperature

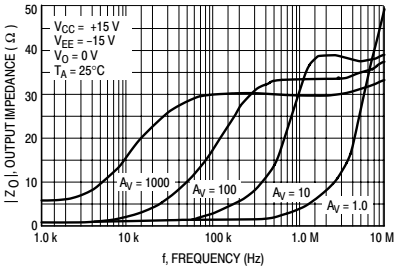

Figure 19. Output Impedance versus Frequency

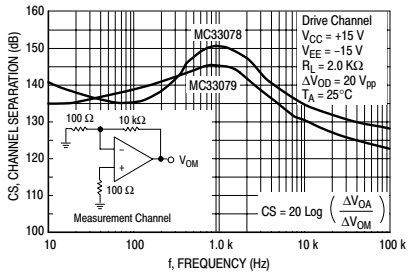

Figure 20. Channel Separation versus Frequency

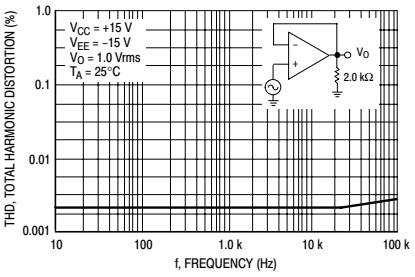

Figure 21. Total Harmonic Distortion versus Frequency

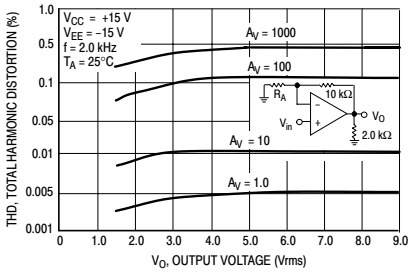

Figure 22. Total Harmonic Distortion versus Output Voltage

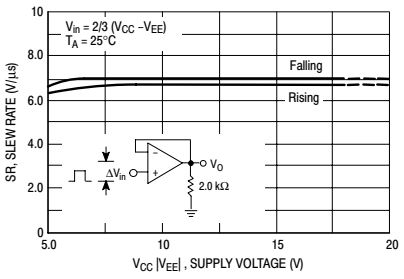

Figure 23. Slew Rate versus Supply Voltage

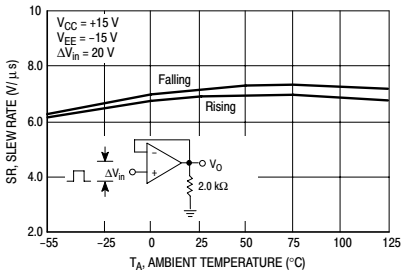

Figure 24. Slew Rate versus Temperature

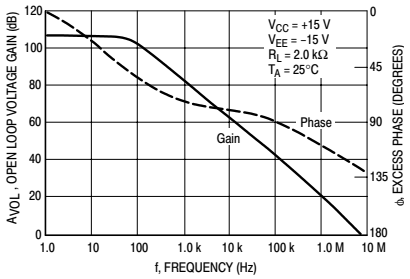

Figure 25. Voltage Gain and Phase versus Frequency

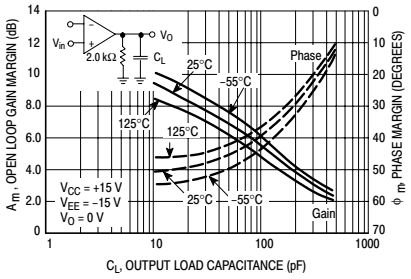

Figure 26. Open Loop Gain Margin and Phase Margin versus Load Capacitance

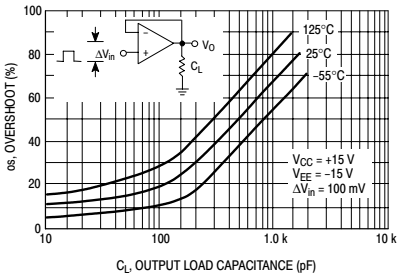

Figure 27. Overshoot versus Output Load Capacitance

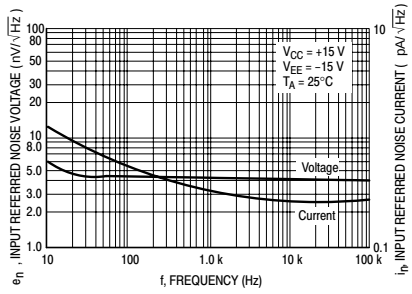

Figure 28. Input Referred Noise Voltage and Current versus Frequency

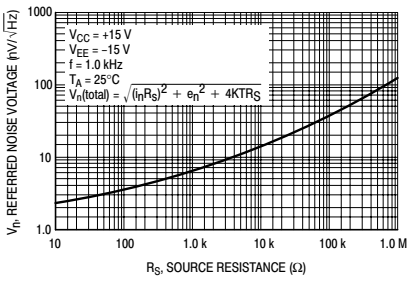

Figure 29. Total Input Referred Noise Voltage versus Source Resistance

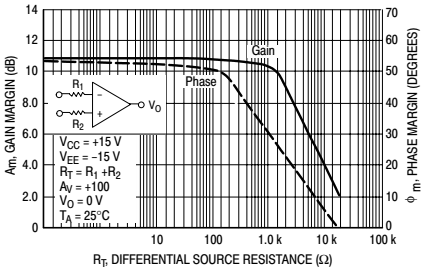

Figure 30. Phase Margin and Gain Margin versus Differential Source Resistance

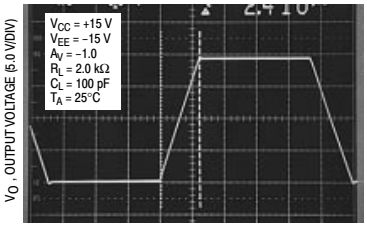

Figure 31. Inverting Amplifier Slew Rate

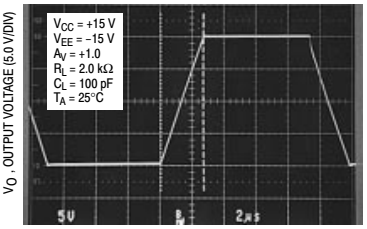

Figure 32. Non−inverting Amplifier Slew Rate

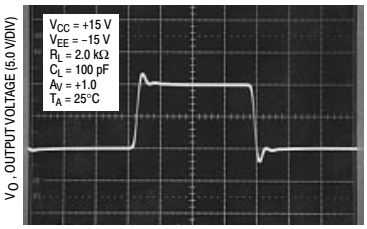

Figure 33. Non−inverting Amplifier Overshoot

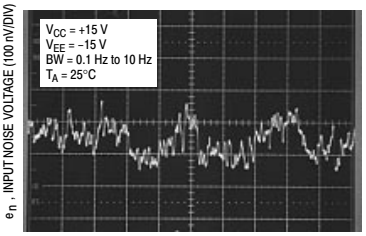

Figure 34. Low Frequency Noise Voltage versus Time

BIBLIOGRAPHY

[1] V. Chen, F. Li, S.-S. Ho, and H. Wechsler, "Micro-Doppler effect in radar: phenomenon, model, and simulation study," *IEEE Trans. Aerosp. Electron. Syst.*, vol. 42, no. 1, pp. 2–21, 2006.

[2] S. Z. Gürbüz, W. L. Melvin, and D. B. Williams, "Detection and identification of human targets in radar data," in *Proc. of SPIE*, vol. 6567, Apr. 2007, pp. 65 670I–65 670I–11.

[3] O. Masoud and N. Papanikolopoulos, "A novel method for tracking and counting pedestrians in real-time using a single camera," *IEEE Trans. Veh. Technol.*, vol. 50, no. 5, pp. 1267–1278, Sep 2001.

[4] D.-Y. Chen and P.-C. Huang, "Visual-based human crowds behavior analysis based on graph modeling and matching," *IEEE Sensors J.*, vol. 13, no. 6, pp. 2129–2138, June 2013.

[5] N. Farrugia, F. Mamalet, S. Roux, F. Yang, and M. Paindavoine, "Fast and robust face detection on a parallel optimized architecture implemented on fpga," *IEEE Trans. Circuits Syst. Video Technol.*, vol. 19, no. 4, pp. 597–602, April 2009.

[6] A. Broggi, A. Fascioli, M. Carletti, T. Graf, and M. Meinecke, "A multi-resolution approach for infrared vision-based pedestrian detection," in *IEEE Intelligent Vehicles Symposium*, June 2004, pp. 7–12.

[7] D. Linzmeier, M. Skutek, M. Mekhaiel, and K. Dietmayer, "A pedestrian detection system based on thermopile and radar sensor data fusion," in *International Conference on Information Fusion*, vol. 2, July 2005, pp. 8 pp.–.

[8] A. Ekimov and J. M. Sabatier, "A review of human signatures in urban environments using seismic and acoustic methods," in *Proc. of IEEE Conference on Technologies for Homeland Security*, 2008, pp. 215–220.

[9] ——, "Range limitation for seismic footstep detection," in *Proc. SPIE*, vol. 6963, 2008, pp. 69 630V–69 630V–12.

[10] ——, "Rhythm analysis of orthogonal signals from human walking," *J. Acoust. Soc. Am.*, vol. 129, no. 3, pp. 1306–1314, 2011.

[11] A. Yarovoy, L. Ligthart, J. Matuzas, and B. Levitas, "UWB radar for human being detection," *IEEE Aerosp. Electron. Syst. Mag.*, vol. 21, no. 11, pp. 22–26, 2006.

[12] T. Sakamoto, Y. Matsuki, and T. Sato, "A novel uwb radar 2-d imaging method with a small number of antennas for simple-shaped targets with arbitrary motion," in *Proc. of IEEE International Conference on Ultra-Wideband*, 2009, pp. 449–453.

[13] S. Chang, N. Mitsumoto, and J. Burdick, "An algorithm for UWB radar-based human detection," in *Proc. of IEEE Radar Conference*, 2009, pp. 1–6.

[14] S. Chang, M. Wolf, and J. Burdick, "Human detection and tracking via Ultra-Wideband (UWB) radar," in *Proc. of IEEE International Conference on Robotics and Automation*, 2010, pp. 452–457.

[15] V. Chen, *Micro-Doppler Effect in Radar*. Artech House, Norwood, 2011.

[16] V. C. Chen, D. Tahmoush, and W. J. Miceli, *Radar Micro-Doppler Signatures: Processing and Applications*, ser. Radar, Sonar, Navigation and Avionics. Institution of Engineering and Technology, 2014.

[17] C. Clemente, A. Balleri, K. Woodbridge, and J. Soraghan, "Developments in target micro-doppler signatures analysis: radar imaging, ultrasound and through-the-wall radar," *EURASIP J. Adv. Signal Process.*, vol. 2013, no. 1, p. 47, 2013.

[18] V. Chen, F. Li, S.-S. Ho, and H. Wechsler, "Analysis of micro-doppler signatures," *Radar, Sonar and Navigation, IEE Proceedings*, vol. 150, no. 4, pp. 271–6–, Aug 2003.

[19] P. Molchanov, K. Egiazarian, J. Astola, A. Totsky, S. Leshchenko, and M. Jarabo-Amores, "Classification of aircraft using micro-doppler bicoherence-based features," *IEEE Trans. Aerosp. Electron. Syst.*, vol. 50, no. 2, pp. 1455–1467, April 2014.

[20] T. Thayaparan, S. Abrol, E. Riseborough, L. Stankovic, D. Lamothe, and G. Duff, "Analysis of radar micro-Doppler signatures from ex-

perimental helicopter and human data," *IET Radar, Sonar and Navigation*, vol. 1, no. 4, pp. 289–299, 2007.

[21] P. Lei, J. Wang, and J. Sun, "Analysis of radar micro-doppler signatures from rigid targets in space based on inertial parameters," *IET Radar, Sonar and Navigation*, vol. 5, no. 2, pp. 93–102, Feb 2011.

[22] G. Smith, K. Woodbridge, and C. Baker, "Radar micro-Doppler signature classification using dynamic time warping," *IEEE Trans. Aerosp. Electron. Syst.*, vol. 46, no. 3, pp. 1078–1096, 2010.

[23] M. Ruegg, E. Meier, and D. Nuesch, "Vibration and rotation in millimeter-wave sar," *IEEE Trans. Geosci. Remote Sens.*, vol. 45, no. 2, pp. 293–304, Feb 2007.

[24] T. Sparr and B. Krane, "Micro-doppler analysis of vibrating targets in sar," *IEE Proceedings Radar, Sonar and Navigation*, vol. 150, no. 4, pp. 277–83–, Aug 2003.

[25] A. Ghaleb, L. Vignaud, and J. Nicolas, "Micro-doppler analysis of wheels and pedestrians in isar imaging," *IET Signal Processing*, vol. 2, no. 3, pp. 301–311, September 2008.

[26] V. Chen, W. Miceli, and B. Himed, "Micro-doppler analysis in isar - review and perspectives," in *Radar Conference - Surveillance for a Safer World*, Oct 2009, pp. 1–6.

[27] *ISAR based on micro-doppler analysis and Chirplet parameter separation*, Nov 2007.

[28] J. Geisheimer, W. Marshall, and E. Greneker, "A continuous-wave (cw) radar for gait analysis," in *Proc. of Signals, Systems and Computers Asilomar Conference*, vol. 1, 2001, pp. 834–838.

[29] J. L. Geisheimer, E. F. Greneker, and W. S. Marshall, "High-resolution doppler model of the human gait," in *Proc. SPIE*, vol. 4744, 2002, pp. 8–18.

[30] P. van Dorp and F. C. A. Groen, "Feature-based human motion parameter estimation with radar," *IET Radar, Sonar and Navigation*, vol. 2, no. 2, pp. 135–145, 2008.

[31] R. Boulic, N. M. Thalmann, and D. Thalmann, "A global human walking model with real-time kinematic personification," *The visual computer*, vol. 6, no. 6, pp. 344–358, 1990.

[32] M. Otero, "Application of a continuous wave radar for human gait recognition," in *Proc. SPIE*, vol. 5809, 2005, pp. 538–548.

[33] I. Bilik and J. Tabrikian, "Radar target classification using Doppler signatures of human locomotion models," *IEEE Trans. Aerosp. Electron. Syst.*, vol. 43, no. 4, pp. 1510–1522, 2007.

[34] Y. Kim and H. Ling, "Human activity classification based on micro-doppler signatures using a support vector machine," *IEEE Trans. Geosci. Remote Sens.*, vol. 47, no. 5, pp. 1328–1337, 2009.

[35] Z. Zhang, P. O. Pouliquen, A. Waxman, and A. G. Andreou, "Acoustic micro-doppler radar for human gait imaging," *J. Acoust. Soc. Am.*, vol. 121, no. 3, pp. EL110–EL113, 2007.

[36] A. Ekimov and J. M. Sabatier, "Human motion analyses using footstep ultrasound and doppler ultrasound," *J. Acoust. Soc. Am.*, vol. 123, no. 6, pp. EL149–EL154, 2008.

[37] A. Mehmood, M. J. Sabatier, M. Bradley, and A. Ekimov, "Extraction of the velocity of walking human's body segments using ultrasonic doppler," *J. Acoust. Soc. Am.*, vol. 128, no. 5, pp. EL316–EL322, 2010.

[38] A. Balleri, K. Chetty, and K. Woodbridge, "Classification of personnel targets by acoustic micro-doppler signatures," *IET Radar, Sonar and Navigation*, vol. 5, no. 9, pp. 943–951, Dec 2011.

[39] A. Balleri, K. Woodbridge, and K. Chetty, "Frequency-agile non-coherent ultrasound radar for collection of micro-doppler signatures," in *2011 IEEE Radar Conference (RADAR)*, May 2011, pp. 045–048.

[40] M. Skolnik, *Radar Handbook*, 3rd ed., ser. Electronics electrical engineering. McGraw-Hill Professional, 2008. [Online]. Available: http://books.google.it/books?id=76uF2Xebm-gC

[41] T. Gill, *The Doppler effect: an introduction to the theory of the effect*. Logos Press, 1965. [Online]. Available: http://books.google.co.uk/books?id=FfZBAAAAIAAJ

[42] F. Faure, G. Debunne, M. Cani-Gauscel, and F. Multon, "Dynamical analysis of human walking," in *Proc. of Eurographics Workshop*, vol. 2, 1997, pp. 53–65.

[43] L. Ren, D. Howard, and L. Kenney, "Biomechanical analysis of the musculoskeletal structure for medicine and sport," *Journal of Bionic Engineering*, june 2007.

[44] P. van Dorp and F. C. A. Groen, "Human walking estimation with radar," in *Proc. IEE Radar, Sonar and Navigation*, vol. 150, no. 5, 2003, pp. 356–365.

[45] D. Ballard, "Generalizing the Hough transform to detect arbitrary shapes," *Pattern Recognition*, vol. 13, no. 2, pp. 111 – 122, 1981.

[46] R. O. Duda and P. E. Hart, "Use of the Hough transformation to detect lines and curves in pictures," *Commun. ACM*, vol. 15, no. 1, pp. 11–15, Jan. 1972.

[47] Z. Changchun and S. Ge, "A Hough transform-based method for fast detection of fixed period sinusoidal curves in images," in *International Conference on Signal Processing*, vol. 1, 2002, pp. 909–912.

[48] "Human sizes," 1998. [Online]. Available: http://www.roymech.co.uk/Useful_Tables/Human/Human_sizes.html

[49] S. Theodoridis, *Pattern recognition*. Elsevier/Academic Press, 2009.